

PhD Thesis

---

# Bulk and Surface Spin-Flop Transitions

J. Karadamoglou

---



University of Crete  
Department of Physics

2001



PhD Thesis

# Bulk and Surface Spin-Flop Transitions

Thesis author: John D. Karadamoglou

Thesis supervisor: Prof. Nikos Papanicolaou

Thesis committee: N. Papanicolaou Thesis supervisor  
T. N. Tomaras Member  
G. P. Tsironis Member  
E. N. Economou Member  
I. E. Perakis Member  
P. Lambropoulos Member  
P. Tzanetakis Member

Physics Department - University of Crete  
Heraklion - Crete

May - 2001



## ACKNOWLEDGMENTS

I would like to thank my advisor, Professor Niko Papanicolaou, for a very fruitful as well as pleasant collaboration. His enthusiasm and deep knowledge of physics have been a source of inspiration for me from the very start of this work.

I would also like to thank Xenofon Zoto for his help and the exceptional hospitality that he and his family has provided me during my visit at Lausanne. Xiaoqun Wang has spent a lot of his time trying to introduce me to the TMRG method and I thank him very much for that.

Finally, I would like to thank the postgraduate students of the University of Crete, for helping me in many ways to complete this thesis.



# Contents

<b>1</b>	<b>Introduction</b>	<b>1</b>
<b>2</b>	<b>Classical Theory</b>	<b>5</b>
2.1	Introduction . . . . .	5
2.2	The infinite chain . . . . .	6
2.3	Antiferromagnetic domain walls . . . . .	8
2.4	Surface spin-flop transition . . . . .	10
2.5	Local stability analysis and critical fields . . . . .	17
2.6	The critical field $H_w$ . . . . .	26
2.7	Phase diagram on a finite chain . . . . .	27
2.8	Hysteresis of the spin-flop transition . . . . .	29
2.9	The odd chain . . . . .	31
2.10	Conclusion . . . . .	35
<b>3</b>	<b>Quantum Theory</b>	<b>37</b>
3.1	Introduction . . . . .	37
3.2	One-magnon spectrum . . . . .	39
3.3	Bulk spin-flop transition . . . . .	43
3.4	Surface spin-flop transition . . . . .	48
3.5	The phase diagram . . . . .	58
3.6	The odd chain . . . . .	59
3.7	The general XYZ model . . . . .	60
3.8	Conclusion . . . . .	63
<b>4</b>	<b>Magnetic resonance</b>	<b>65</b>
4.1	Introduction . . . . .	65
4.2	Bulk spin-flop transition . . . . .	67

4.3	Surface spin-flop transition . . . . .	72
4.4	Conclusion . . . . .	75
<b>5</b>	<b>Thermodynamics</b>	<b>77</b>
5.1	Introduction . . . . .	77
5.2	Magnetization . . . . .	78
5.3	Specific heat . . . . .	80
5.4	Johnson-Bonner anomalies . . . . .	84
5.5	Conclusion . . . . .	85
<b>6</b>	<b>Spin-1 planar ferromagnet CsNiF<sub>3</sub></b>	<b>87</b>
6.1	Introduction . . . . .	87
6.2	The magnon dispersion . . . . .	88
6.3	Thermodynamics . . . . .	94
6.3.1	Field perpendicular to $c$ . . . . .	95
6.3.2	Field parallel to $c$ . . . . .	102
6.4	Conclusion . . . . .	107
<b>7</b>	<b>Conclusion</b>	<b>109</b>
 <b>APPENDICES</b>		
<b>A</b>	<b>Detailed description of the SSF phase</b>	<b>111</b>

# CHAPTER 1

## INTRODUCTION

The nature of magnetic interactions was understood only after the establishment of quantum physics, since classical electromagnetic theory failed to account for the origin of magnetic phenomena in matter. Heisenberg in 1928 showed that in quantum mechanics Coulomb interactions along with Pauli's exclusion principle can lead to spin dependent interactions. One of the most important one-dimensional (1D) models proposed for the description of magnetic interactions is the spin- $\frac{1}{2}$  XYZ model described by the general Hamiltonian

$$W = \sum_{n=1}^{\Lambda-1} \left( J_1 S_n^x S_{n+1}^x + J_2 S_n^y S_{n+1}^y + J_3 S_n^z S_{n+1}^z \right) - H \sum_{n=1}^{\Lambda} S_n^z, \quad (1.1)$$

where  $\mathbf{S}_n$  is the spin- $\frac{1}{2}$  operator at site  $n$ ,  $\Lambda$  is the total number of sites in the chain,  $J_1$ ,  $J_2$ ,  $J_3$ , are exchange constants, and  $H$  is a magnetic field applied in the  $z$  direction.

Special cases of (1.1) have been the subject of numerous studies and have played an important role in statistical physics. Ising in 1925 [1] studied a model with  $J_1 = J_2 = 0$  which was later (1944) solved in 2D for the case of  $H = 0$  by Onsager [2]. For  $J_1 = J_2 = J_3$  Hamiltonian (1.1) describes the isotropic Heisenberg or XXX model (Heisenberg 1928 [3], Bloch 1930 [4]). The case  $J_1 = 0$  is known as the XY model. Explicit expressions for all the eigenvalues can be given (for any  $\Lambda$ ) and the partition function evaluated (Lieb 1961 [5], Katsura 1962 [6]). The case  $J_1 = J_2$  is called the Heisenberg-Ising or XXZ model for which Bethe [7] provided the correct

form of eigenfunctions and eigenvalues (Bethe Ansatz), while Yang and Yang (1966) [8–10] proved rigorously that Bethe’s Ansatz was correct, and derived the ground state and elementary excitations in the limit of large  $\Lambda$ . Later Gaudin [11, 12] derived an infinite set of coupled nonlinear integral equations, often referred to as Gaudin-Takahashi equations [13], from which it is possible to determine the free energy for any value of the magnetic field  $H$ . In 1972 Baxter calculated the free energy along with the low-lying eigenvalues and their corresponding eigenvectors for the general XYZ model in the absence of magnetic field [13–16]. Special cases of the XYZ model were found to be related to other integrable quantum 1D or classical 2D systems, such as the spinless fermion gas or the eight vertex model, and led to the development of new mathematics for their solution [17, 18].

Recently, there has been increased theoretical interest in surface effects on antiferromagnetic chains, which had been theoretically predicted some time ago [19–21]. This was partly due to the observation of a surface spin-flop transition in an Fe/Cr multilayer [22–25] a system that has attracted research interest due to its giant magnetoresistance. It has been shown that Fe/Cr multilayers can be modeled by a classical antiferromagnetic spin chain characterized by an isotropic exchange interaction  $J_1 = J_2 = J_3 = J > 0$  and a single-ion quadratic anisotropy of the form  $-D(S_n^z)^2$ , where  $D$  is a positive constant. The precise nature of the surface transition proved to be more intricate than originally envisaged and has only recently been clarified in a number of theoretical investigations [25–35]. Similar investigations for the quantum case [36–41] were limited to surface effects in the presence of artificial boundary fields which are difficult to implement experimentally. The Bethe Ansatz does not apply in the presence of a *uniform* field  $H$ , except in very special limits; e.g.  $J_1 = J_2$ .

In this work we investigate the possibility of such a transition in an antiferromagnetic quantum XYZ model in a uniform field. In chapter 2 we show that a spin-flop transition is present in a general class of classical XYZ Hamiltonians [42]. We present a detailed description of surface effects in order to prepare the ground for the quantum mechanical model studied in the following chapters and at the same time clarify some of the dark points of the surface transition in magnetic multilayers.

In chapter 3 we show [43] that a surface spin-flop transition can be induced

---

by a uniform bias field in a special case of the quantum Hamiltonian (1.1), leading to the creation of quantum domain walls. A bulk spin-flop transition takes place for larger fields through a nontrivial mechanism and is studied both analytically and numerically. The possibility of experimental realization is discussed together with a generalization to other quantum models in the general class (1.1).

The low temperature electron spin resonance spectrum of our special model is studied in chapter 4. We find that the resulting spectrum can probe both the surface and the bulk spin-flop transition as well as the excitation gap of our system for all values of the bias field. Our analytical results provide a complete picture for all values of the parameters of our model.

In chapter 5 the recently developed transfer matrix renormalization group (TMRG) method is used for the calculation of the magnetization and the specific heat directly in the thermodynamic limit [44]. We study their field and temperature dependence to find that signatures of the bulk spin-flop transition are apparent in both the magnetization and the specific heat. We also discuss low temperature spin-wave anomalies that are predicted to occur in the specific heat.

In chapter 6 we apply the TMRG method to provide an accurate calculation of the thermodynamics in a quantum spin-1 planar ferromagnetic chain [45]. We also calculate the field dependence of the magnon gap and confirm the accuracy of the magnon dispersion derived earlier through an  $1/n$  expansion. We are thus in a position to analyze a wide range of experiments on  $\text{CsNiF}_3$ . We finally present some indirect evidence to the effect that the popular interpretation of the excess specific heat in terms of sine-Gordon solitons may not be appropriate.

Our main conclusions are briefly summarized in chapter 7.



## CHAPTER 2

# CLASSICAL THEORY

### 2.1 Introduction

In this chapter we study [42] the ground state and phase diagram of a classical, easy-axis antiferromagnet described by Hamiltonian (1.1) restricted by the inequalities

$$|J_1| \leq J_2 \leq J_3. \quad (2.1)$$

The classical spin is parametrized by the usual spherical variables:

$$S_n^x + iS_n^y = s \sin \theta_n e^{i\phi_n}, \quad S_n^z = s \cos \theta_n, \quad (2.2)$$

where we further set  $s = 1/2$  in order to allow for a direct comparison with the quantum model studied in Chapter 3.

Because of (2.1) the ground state is characterized by  $\phi_n = \pi/2$  and is thus independent of the specific value of  $J_1$ . The spin configuration can therefore be written in the form

$$S_n^x = 0, \quad S_n^y = \frac{1}{2} \sin \theta_n, \quad S_n^z = \frac{1}{2} \cos \theta_n \quad (2.3)$$

and stable states are found as the local minima of the effective potential

$$W = \frac{1}{4} \sum_{n=1}^{\Lambda-1} \left( \sin \theta_n \sin \theta_{n+1} + \Delta \cos \theta_n \cos \theta_{n+1} \right) - \frac{H}{2} \sum_{n=1}^{\Lambda} \cos \theta_n, \quad (2.4)$$

where units are chosen such that  $J_2 = 1, J_3 = \Delta$ . Mathematically the problem reduces to solving the system of equations

$$\frac{\partial W}{\partial \theta_n} = 0, \quad n = 1, 2, \dots, \Lambda \quad (2.5)$$

in addition to performing a stability analysis for each solution of (2.5).

In sections 2.2 and 2.3 we study the ground state and topologically non-trivial excitations of the infinite system. In sections 2.4 to 2.7 we discuss surface induced effects, and derive the phase diagram of the finite chain, while in section 2.8 we discuss hysteresis phenomena. We then apply our results to describe the odd chain in section 2.9 and we conclude in section 2.10. Finally, Appendix A offers a more detailed description of surface effects.

## 2.2 The infinite chain

The infinite chain is easier to investigate analytically because of its translational symmetry. In order to find the ground state of the infinite system, we can take advantage of the fact that the antiferromagnetic ground state is periodic with period of, at most, two sites. The energy per site is then given by

$$V = \frac{1}{4} \left[ \sin \theta_1 \sin \theta_2 + \Delta \cos \theta_1 \cos \theta_2 - H(\cos \theta_1 + \cos \theta_2) \right] \quad (2.6)$$

and condition (2.5) reduces to

$$\frac{\partial V}{\partial \theta_1} = \frac{\partial V}{\partial \theta_2} = 0. \quad (2.7)$$

The simplest solution of (2.7) is the well known Néel state shown in fig. 2.1,



**Figure 2.1:** The Néel state.

which corresponds to  $(\theta_1 = 0, \theta_2 = \pi)$  and its energy per site is given by

$$V = -\frac{\Delta}{4}. \quad (2.8)$$

A second solution of equation (2.7) is the canted state depicted in figure 2.2



**Figure 2.2:** The canted state.

and analytically described by

$$\theta_1 = -\theta_2 = \theta, \quad \cos \theta = \frac{H}{\Delta + 1}, \quad (2.9)$$

while its energy per site is

$$V = -\frac{1}{4} \left( 1 + \frac{H^2}{\Delta + 1} \right). \quad (2.10)$$

The canted state contains as a special case the ferromagnetic state ( $\theta_1 = \theta_2 = 0$ ) shown in figure 2.3, whose energy per site is given by

$$V = \frac{1}{4}(\Delta - 2H). \quad (2.11)$$

A simple comparison of the energies given in equations (2.8), (2.10) and



**Figure 2.3:** The ferromagnetic state.

(2.11) establishes the existence of two critical fields:

$$H_b = \sqrt{\Delta^2 - 1}, \quad H_f = \Delta + 1. \quad (2.12)$$

For  $H < H_b$  the Néel state is the ground state. Once  $H_b$  is reached a Bulk Spin Flop (BSF) transition takes place and the canted state becomes the lowest energy state for  $H_b < H < H_f$ . Finally, when  $H$  exceeds  $H_f$  total ferromagnetic order is established. The emerging picture is summarized in the phase diagram of figure 2.4. Here we call AF, BSF, and F the phases where the Néel, the canted, and the ferromagnetic state, are the ground states of our system. The dashed line shows the region of stability of the Ising type domain wall discussed in section 2.3.

We can see that the spin configuration of the ground state changes discontinuously at the transition from the AF to the BSF phase (figs. 2.1, 2.2), and therefore the BSF transition is a first order transition. On the other hand, the F transition is a smooth, second-order transition (figs. 2.2, 2.3). A complete stability analysis of the uniform states described in this section will be given in section 2.5.





locked DW for  $H = 0$  leads to the corresponding “up” configuration transformed by  $\mathbf{S}_n \rightarrow -\mathbf{S}_n$ . The two kinds of DW are degenerate for zero field. Once we apply a positive external field the “up” DW, with its central spins in the direction of  $H$ , becomes energetically preferable.

Analytical description of the DW is available only near the isotropic limit through the continuum approximation. It is useful to define  $\delta = \Delta - 1$  and the rationalized magnetic field  $h = H/\sqrt{2\delta}$ . In order to turn from the alternating variables  $\mathbf{S}_n$  to a set of *slow* ones we introduce

$$\mathbf{m}_\alpha = \mathbf{S}_{2\alpha-1} + \mathbf{S}_{2\alpha}, \quad \mathbf{n}_\alpha = \mathbf{S}_{2\alpha-1} - \mathbf{S}_{2\alpha} \quad \alpha = 1, 2, \dots \quad (2.15)$$

where  $\alpha$  is a sublattice index from which we define the position variable  $y = \sqrt{2\delta(1-h^2)} \alpha$ . In the limit of

$$\sqrt{2\delta(1-h^2)} \ll 1 \quad (2.16)$$

one can show [46] that

$$\begin{aligned} n_1(y) &= 0, & n_2(y) &= \frac{1}{\cosh y}, & n_3(y) &= -\tanh y, \\ m_1(y) &= 0, & m_2(y) &= \frac{\sqrt{2\delta}}{2} [h + \sqrt{1-h^2}] \frac{\tanh y}{\cosh y}, \\ m_3(y) &= \frac{\sqrt{2\delta}}{2} [h + \sqrt{1-h^2}] \frac{1}{\cosh^2 y}, \end{aligned} \quad (2.17)$$

The continuum approximation will prove useful in Appendix A for the understanding of the surface-DW interaction.

## 2.4 Surface spin-flop transition

We will now use the relaxation algorithm (2.14) to perform numerical experiments on a finite chain of length  $\Lambda = 22$ , which is a typical size of realistic Fe/Cr multilayers [22–25], for specific values of  $\Delta$ . Specifically, we start our simulations with  $H = 0$ , and our system in a slightly perturbed Néel state, and we increase the magnetic field in small steps until the chain reaches ferromagnetic saturation. For each value of  $H$  we allow the system to relax to a stable configuration and we then calculate the energy, as well

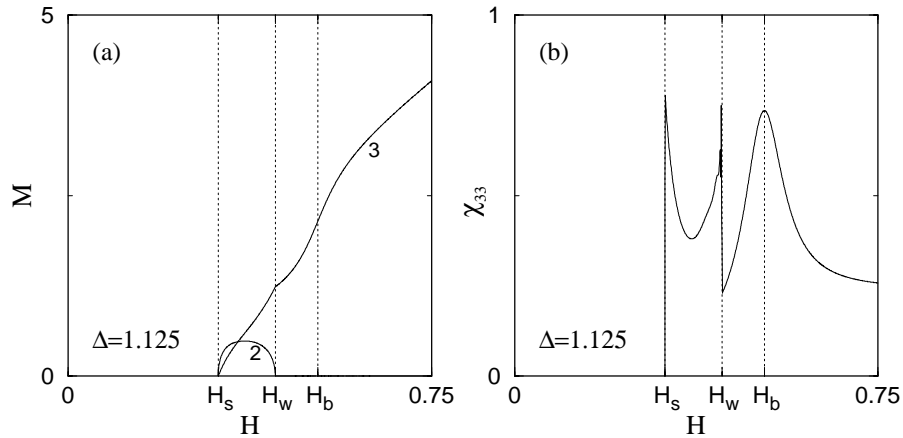


**Figure 2.7:** Field dependence of the total magnetization and susceptibility for an open chain with  $\Lambda = 22$  sites and  $\Delta = 1.125$ . (a) The two nonvanishing components of the magnetization  $M_2$  and  $M_3$ . (b) The diagonal susceptibility  $\chi_{33}$  defined as in equation (2.18).

as the magnetization and susceptibility per site defined from

$$\mathbf{M} = \sum_{n=1}^{\Lambda} \mathbf{S}_n \equiv (M_1 = 0, M_2, M_3), \quad \chi_{23} = \frac{1}{\Lambda} \frac{\partial M_2}{\partial H}, \quad \chi_{33} = \frac{1}{\Lambda} \frac{\partial M_3}{\partial H}. \quad (2.18)$$

For the next value of magnetic field  $H + dH$  we use as initial condition the configuration found in the previous step<sup>1</sup>, slightly perturbed in order to escape unstable solutions. This procedure, although it may skip the absolute energy minimum, simulates better an actual experiment than a direct minimization of the effective potential.

We first perform a simulation for  $\Delta = 1.125$  that gives us the total magnetization and susceptibility per site of figure 2.7. One can see that there are two new critical fields  $H_s, H_w < H_b$  that were absent in the infinite system. Once  $H_s$  is reached the magnetization gradually acquires non zero values while the susceptibility suffers a sudden jump. At  $H_w$  the magnetization develops a knee that causes a sharp peak in the susceptibility, and once  $H_b$  is reached the BSF transition takes place creating a new smoother peak in the susceptibility. Finally, the magnetization takes its saturation value  $M_3 = \Lambda/2$  for fields greater than  $H_f$  (not displayed in figure 2.7).

<sup>1</sup>One can also use a slightly perturbed Néel state as initial condition for all values of  $H$ . It turns out to give the same results.

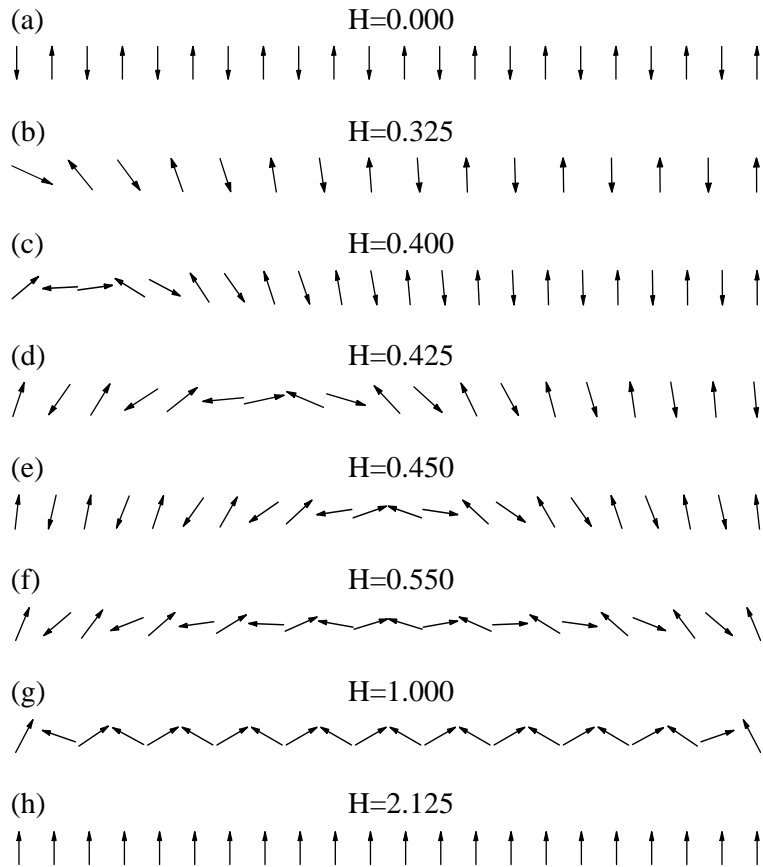


**Figure 2.8:** The spin configurations for  $\Delta = 1.125$ ,  $\Lambda = 22$  for a characteristic set of field values. The critical fields for this  $\Delta$  are  $H_s = 0.310$ ,  $H_w = 0.428$ ,  $H_b = 0.515$ ,  $H_f = 2.125$ .

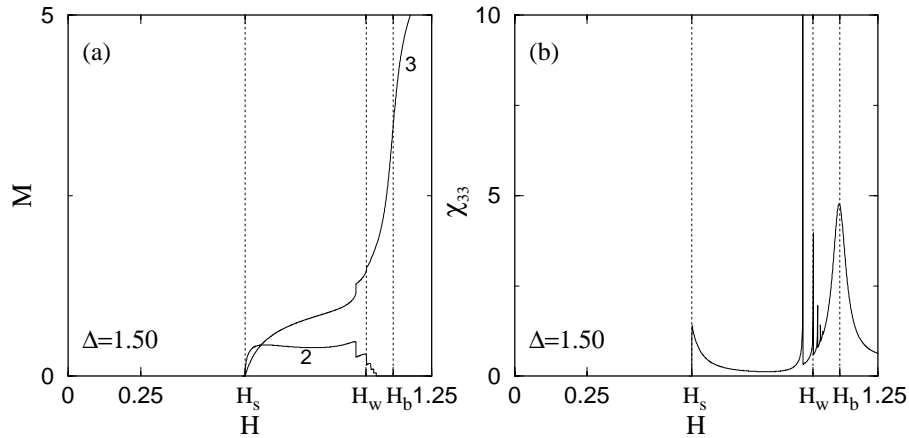


**Figure 2.9:** As in figure 2.7 but for  $\Delta = 1.50$ .

In figure 2.8 we see the spin configurations for a convenient set of field values. For magnetic fields in the region of  $(0, H_s)$  the ground state is the Néel state (fig. 2.8a). Once we reach  $H_s$  the spin opposed to the field gradually deviates from its  $-z$  direction and the system relaxes in a surface state (fig. 2.8b). We will thus call the transition that takes place at  $H_s$  the surface spin-flop (SSF) transition. Further increase of  $H$  causes the ending spin to further align with the field and the surface state to become a DW located near the surface as  $H$  approaches  $H_w$  (fig. 2.8c). The created DW moves further towards the center with increasing bias field and does so rapidly when  $H$  crosses  $H_w$  (fig. 2.8d). The wall eventually migrates and becomes symmetric about the center to great numerical precision near the critical field  $H_b$  (fig. 2.8e). In the region  $H \gtrsim H_b$  the domain wall expands symmetrically about the center to become a nearly uniform canted state within the bulk with notable nonuniformities near the edges (fig. 2.8f,g). Finally complete ferromagnetic order is achieved when  $H$  crosses the last critical field  $H_f$  (fig. 2.8h).

To investigate the  $\Delta$  dependence of the SSF transition we repeat our numerical experiment for  $\Delta = 1.50$ . The corresponding total magnetization and susceptibility per site are shown in figure 2.9. We see that the evolution of the SSF transition with  $H$  produces more structure in the susceptibility and magnetization around the critical field  $H_w$  compared with the  $\Delta = 1.125$  case.

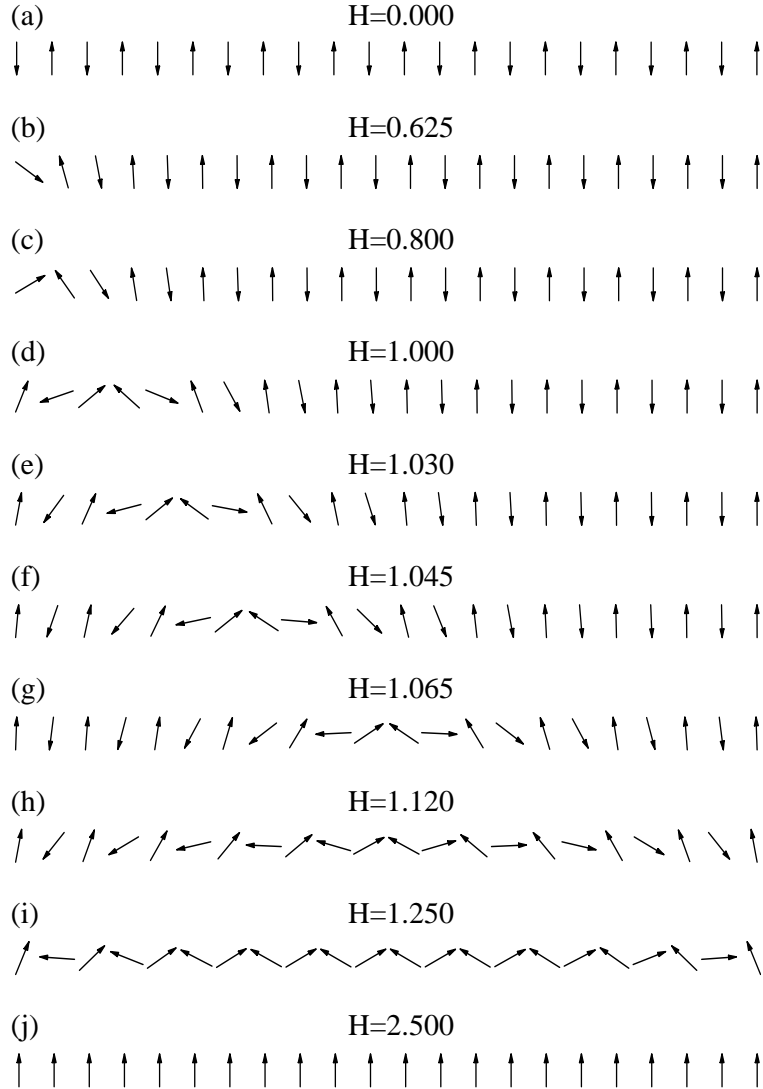


**Figure 2.10:** The spin configurations for  $\Delta = 1.5$ ,  $\Lambda = 22$  for a characteristic set of field values. The critical fields for this  $\Delta$  are  $H_s = 0.610$ ,  $H_w = 1.025$ ,  $H_b = 1.120$ ,  $H_f = 2.500$ .

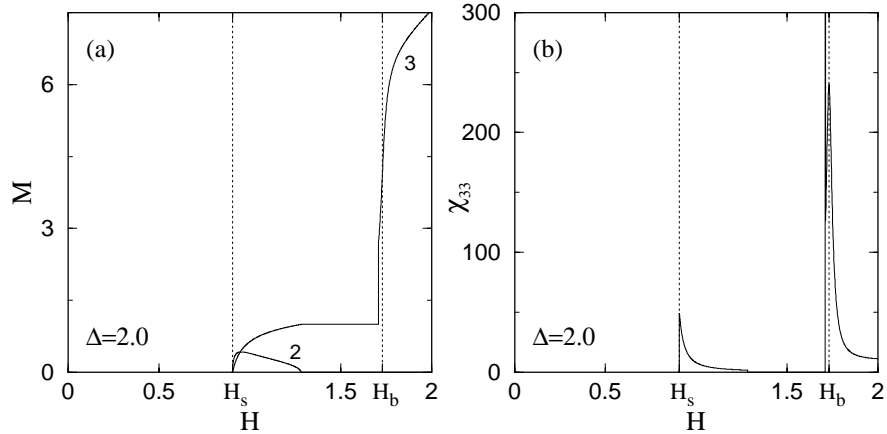


**Figure 2.11:** As in figures 2.7 and 2.9 for  $\Delta = 2$ .

Figure 2.10 shows a set of the corresponding spin configurations. Once we reach the critical field  $H_s$ , the SSF transition takes place (fig. 2.10b) and the system gradually develops a DW (fig. 2.10c) that moves towards the center with increasing field (fig. 2.10c-g). Yet, in order for it to move from the position of figure 2.10c, zero sites away from the surface, to that of figure 2.10d, two sites away from the surface, it has to go through an unfavorable “down” DW located one site away from the surface. Specifically, as we increase the field the DW is moving towards the center through a series of first order transitions from a preferable “up” wall located an even number of sites away from the surface to an energy costing “down” one at an odd number of sites away from the surface, and that causes the sharp peaks in the susceptibility. Because of the barriers that the wall encounters in its movement it is delayed from settling in the center which now happens closer to  $H_b$ . Once the DW does so, the system evolves with the field similarly to the  $\Delta = 1.125$  case, first to the canted and then to the ferromagnetic state. One should mention here that the barriers that the DW suffers during its movement are similar to Peierls barriers observed in Frenkel-Kontorova type models [47].

The reason that this structure around  $H_w$  was absent in the susceptibility of the  $\Delta = 1.125$  case is that the energy difference between the “up” and the “down” wall diminishes for smaller anisotropies. The picture above is verified by performing numerical experiments for intermediate anisotropies,

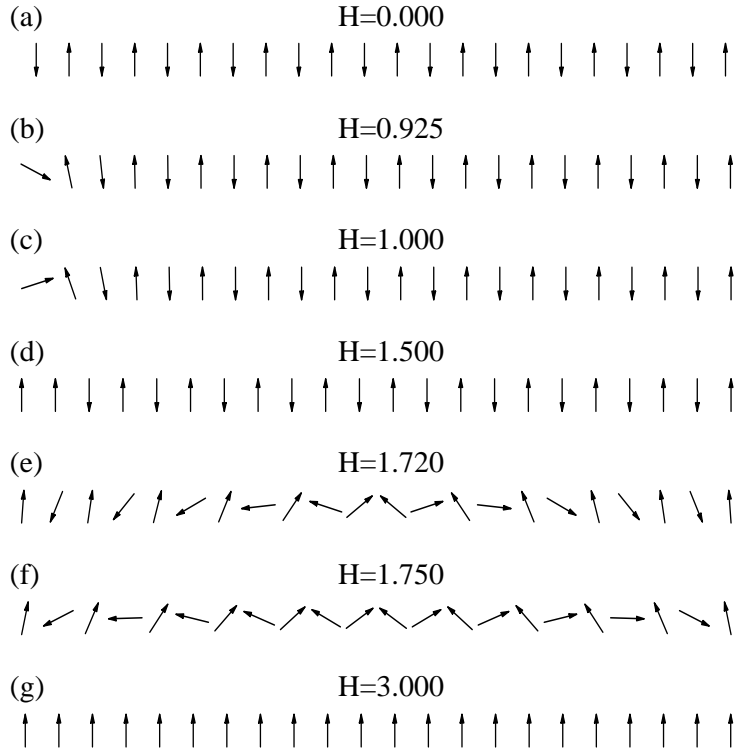


**Figure 2.12:** The spin configurations for  $\Delta = 2$ ,  $\Lambda = 22$  for a characteristic set of field values. The critical fields for this  $\Delta$  are  $H_s = 0.905$ ,  $H_b = 1.730$ ,  $H_f = 3.00$ .

where the occurring effects lie between the two cases we have presented.

One can ask what will happen for even greater anisotropies and specifically above the line  $H_{[\infty]}$  (eq. (2.13)) where we can have stable Ising type DW's. In order to investigate the possibility of such a DW created through the SSF transition we perform an experiment for  $\Delta = 2$ . The susceptibility and magnetization diagrams (fig. 2.11) show that the critical field  $H_w$  is now absent while there is a region before  $H_b$  where the magnetization remains stable at  $M = 2$ .

We can see that after the SSF transition has taken place (fig. 2.12b), the created DW, located right at the surface, becomes locked at a new critical field  $H_{[0]}$  different than  $H_{[\infty]}$  (fig. 2.12d). The wall unlocks just before  $H_b$  and then moves rapidly towards the center of the chain to spread and give its place to the canted state once the BSF field is crossed. Once again total ferromagnetic order is achieved for  $H > H_f$ .

To conclude, our numerical experiments show that the SSF transition is always present but its evolution strongly depends on the specific choice of  $\Delta$ . The main phenomena that complicate the straightforward picture of our first ( $\Delta = 1.125$ ) experiment are the barriers encountered in the movement between two successive “up” DW's for large anisotropies, and the locking of the wall for even larger  $\Delta$ 's. Yet, we have not provided detailed description of the critical fields that we have found nor any analytical formulas for their accurate determination. This will be our task in sections 2.5 and 2.6 below while in Appendix A we provide a detailed analysis of the surface state in the limit of small anisotropies.

## 2.5 Local stability analysis and critical fields

We now present a systematic stability analysis for some of the stationary states of both the infinite and the finite chain. A stationary state becomes unstable when the corresponding Hessian  $\tilde{H}$  ceases to be positive definite. Therefore in the rest of this section our task will be to solve the eigenvalue problem

$$\tilde{H}\mathbf{C} = \frac{\omega}{2}\mathbf{C}, \quad (2.19)$$

where  $\omega/2$  are the eigenfrequencies, and  $\mathbf{C}$  the corresponding eigenvectors, in order to determine the combination of parameters  $\Delta$  and  $H$  for which the lowest lying eigenvalue crosses zero to become negative. It is straightforward to check that the only non-zero elements of the Hessian calculated from our effective potential (2.4) for a spin state  $\{\theta_i\}$  are

$$\begin{aligned} \left. \frac{\partial^2 V}{\partial \theta_n^2} \right|_{\{\theta_i\}} &= \frac{1}{4}(-\sin \theta_n \sin \theta_{n-1} - \Delta \cos \theta_n \cos \theta_{n-1}) \\ &+ \frac{1}{4}(-\sin \theta_n \sin \theta_{n+1} - \Delta \cos \theta_n \cos \theta_{n+1}) \\ &+ \frac{H}{2} \cos \theta_n \end{aligned} \quad (2.20)$$

$$\left. \frac{\partial^2 V}{\partial \theta_n \partial \theta_{n+1}} \right|_{\{\theta_i\}} = \frac{1}{4}(\cos \theta_n \cos \theta_{n+1} + \Delta \sin \theta_n \sin \theta_{n+1})$$

$$\left. \frac{\partial^2 V}{\partial \theta_n \partial \theta_{n-1}} \right|_{\{\theta_i\}} = \frac{1}{4}(\cos \theta_n \cos \theta_{n-1} + \Delta \sin \theta_n \sin \theta_{n-1}).$$

We start with the stability analysis of the lowest energy states of the infinite system discussed in section 2.2. The Hessian of the Néel (AF) state is easily found from equation (2.20) to be

$$\tilde{H} = \frac{1}{2} \begin{pmatrix} \cdot & \cdot & \cdot & \cdot & \cdot & \cdot \\ \cdot & \Delta + H & -1/2 & 0 & 0 & \cdot \\ \cdot & -1/2 & \Delta - H & -1/2 & 0 & \cdot \\ \cdot & 0 & -1/2 & \Delta + H & -1/2 & \cdot \\ \cdot & 0 & 0 & -1/2 & \Delta - H & \cdot \\ \cdot & \cdot & \cdot & \cdot & \cdot & \cdot \end{pmatrix} \quad (2.21)$$

and the eigenproblem of equation (2.19) can be rewritten as

$$[\Delta + (-1)^n H - \omega] C_n = \frac{1}{2}(C_{n+1} + C_{n-1}) \quad (2.22)$$

where  $C_n$  are the components of the eigenvector  $\mathbf{C}$ .

Here we introduce the sublattice variables

$$A_n = C_{2n-1}, \quad B_n = C_{2n}, \quad (2.23)$$

in terms of which the linear system (2.22) takes the form

$$\begin{aligned} (\Delta - H - \omega) A_n &= \frac{1}{2}(B_{n-1} + B_n), \\ (\Delta + H - \omega) B_n &= \frac{1}{2}(A_n + A_{n+1}). \end{aligned} \quad (2.24)$$

It is now a straightforward matter to eliminate  $B_n$  to obtain the equivalent system

$$B_n = \frac{1}{2} \frac{A_n + A_{n+1}}{\Delta + H - \omega}, \quad (2.25a)$$

$$[(\Delta - \omega)^2 - H^2] A_n = \frac{1}{4}(2A_n + A_{n+1} + A_{n-1}), \quad (2.25b)$$

whose solution is  $A_n = e^{ikn}$ , where  $k \in [0, 2\pi)$  is a sublattice crystal momentum, provided that

$$\omega = \Delta \pm \sqrt{H^2 + \cos^2(k/2)}. \quad (2.26)$$

For the case of the canted (BSF) state the calculation of the Hessian gives

$$\tilde{H} = \frac{1}{2} \begin{pmatrix} \cdot & \cdot & \cdot & \cdot & \cdot & \cdot \\ \cdot & 1 & A & 0 & 0 & \cdot \\ \cdot & A & 1 & A & 0 & \cdot \\ \cdot & 0 & A & 1 & A & \cdot \\ \cdot & 0 & 0 & A & 1 & \cdot \\ \cdot & \cdot & \cdot & \cdot & \cdot & \cdot \end{pmatrix}, \quad A \equiv \frac{1}{2} \left( \frac{H^2}{\Delta + 1} - \Delta \right), \quad (2.27)$$

and its diagonalization leads to the system of equations

$$(\omega - 1)C_n = A(C_{n-1} + C_{n+1}) \quad (2.28)$$

with solution

$$\begin{aligned} C_n &= e^{ikn}, & k &\in [0, 2\pi), \\ \omega &= 1 + 2A \cos k. \end{aligned} \quad (2.29)$$

Finally, for the ferromagnetic (F) state we find

$$\tilde{H} = \frac{1}{2} \begin{pmatrix} \cdot & \cdot & \cdot & \cdot & \cdot & \cdot \\ \cdot & H - \Delta & 1/2 & 0 & 0 & \cdot \\ \cdot & 1/2 & H - \Delta & 1/2 & 0 & \cdot \\ \cdot & 0 & 1/2 & H - \Delta & 1/2 & \cdot \\ \cdot & 0 & 0 & 1/2 & H - \Delta & \cdot \\ \cdot & \cdot & \cdot & \cdot & \cdot & \cdot \end{pmatrix}, \quad (2.30)$$

whose eigenvalue problem gives

$$\begin{aligned} (\omega - H + \Delta)C_n &= \frac{1}{2}(C_{n-1} + C_{n+1}) \\ C_n &= e^{ikn}, & k &\in [0, 2\pi), \\ \omega &= \cos k + H - \Delta. \end{aligned} \quad (2.31)$$

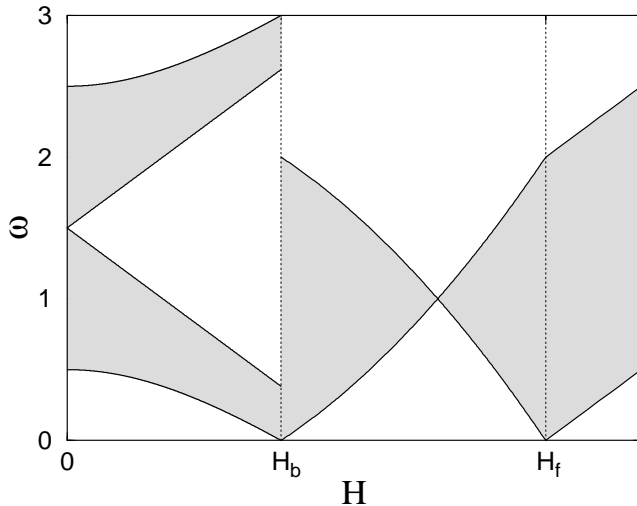


**Figure 2.13:** The spectrum of the quadratic fluctuations of the infinite system as a function of  $H$ .

In figure 2.13 we show the full spectrum of eigenfrequencies for the AF ( $0 < H < H_b$ ) the BSF ( $H_b < H < H_f$ ) and the F ( $H_f < H$ ) phase as a function of the magnetic field. We see that the lowest lying eigenfrequency of the AF spectrum becomes zero at the critical field  $H_b$  above which the Néel state becomes unstable. Similarly, we find the eigenvalues (2.29) to be strictly positive in the region  $(H_b, H_f)$  where the canted state is locally stable. Finally, the ferromagnetic state becomes stable above  $H_f$ , as expected.

We will now perform the stability analysis for the Ising type DW discussed in section 2.3. We consider such a DW with its two aligned spins located at sites 0 and 1 whose Hessian is

$$\tilde{H} = \frac{1}{2} \begin{pmatrix} \cdot & \cdot \\ \cdot & \Delta+H & -1/2 & 0 & 0 & 0 & 0 & \cdot \\ \cdot & -1/2 & \Delta-H & -1/2 & 0 & 0 & 0 & \cdot \\ \cdot & 0 & -1/2 & H & 1/2 & 0 & 0 & \cdot \\ \cdot & 0 & 0 & 1/2 & H & -1/2 & 0 & \cdot \\ \cdot & 0 & 0 & 0 & -1/2 & \Delta-H & -1/2 & \cdot \\ \cdot & 0 & 0 & 0 & 0 & -1/2 & \Delta+H & \cdot \\ \cdot & \cdot \end{pmatrix} \quad (2.32)$$

and its eigenvalue problem (2.19) can be explicitly written as

$$(\Delta + (-1)^n H - \omega)C_n = \frac{1}{2}(C_{n-1} + C_{n+1}), \quad n = -1, -2, \dots \quad (2.33a)$$

$$(H - \omega)C_0 = \frac{1}{2}(C_{-1} - C_1), \quad (2.33b)$$

$$(H - \omega)C_1 = \frac{1}{2}(-C_0 + C_2), \quad (2.33c)$$

$$(\Delta + (-1)^{n+1}H - \omega)C_n = \frac{1}{2}(C_{n-1} + C_{n+1}) \quad n = 2, 3, \dots \quad (2.33d)$$

Since we seek after a combination of  $H$  and  $\Delta$  for which the lowest lying eigenvalue becomes zero we explicitly set  $\omega = 0$  to simplify the calculation. One can see that (2.33a) is identical to (2.22) for  $n = -1, -2, \dots$ , and we can therefore apply the transformation (2.23) to obtain equations (2.24), (2.25) which are satisfied by a solution of the special form

$$\begin{aligned} A_n &= \psi^{-n}, & n &= 0, -1, \dots \\ B_n &= \frac{1}{2} \frac{1 + \psi^{-1}}{\Delta + H} \psi^{-n} \equiv r\psi^{-n}, & n &= -1, -2, \dots \end{aligned} \quad (2.34)$$

provided that

$$\Delta^2 - H^2 = \frac{1}{4}(2 + \psi + 1/\psi) \quad (2.35)$$

and supplemented by the requirement  $|\psi| < 1$  which guarantees that the state decays exponentially away from the wall. Demanding that the eigenstate will be symmetric about the center of the wall we find similarly the solution of (2.33d) to be

$$\begin{aligned} B_n &= \psi^{n-1}, & n &= 1, 2, \dots \\ A_n &= \frac{1}{2} \frac{1 + \psi^{-1}}{\Delta + H} \psi^{n-1} = r\psi^{n-1}, & n &= 2, 3, \dots \end{aligned} \quad (2.36)$$

and replacing equations (2.34), (2.36) in the remaining equations of (2.33) we find that

$$\begin{aligned} \Delta - H &= \frac{1}{2}(r\psi + B_0), \\ HB_0 &= \frac{1}{2}(1 - A_1), \\ HA_1 &= \frac{1}{2}(1 - B_0), \\ \Delta - H &= \frac{1}{2}(r\psi + A_1). \end{aligned} \quad (2.37)$$

This system is further simplified by applying our symmetry argument again to set  $A_1 = B_0$ , leading to a unique equation for  $\psi$

$$\Delta - H = \frac{1}{2} \left( r\psi + \frac{1}{2H+1} \right) \quad (2.38)$$

which we can now combine with (2.35) to obtain our final result of equation (2.13) already discussed in section 2.3.

We will now search for instabilities that may arise from the surfaces in order to probe the finite system, similarly to the single ion model case of references 20, 35. Analytical diagonalization of the Hessian of the finite system is not possible and one has to perform the preceding analysis for the semi-infinite system where the essential new ingredients can be explicitly obtained.

The Hessian of a semi-infinite system with its ending spin located at site 1 and pointing in the  $-z$  direction is found to be

$$\tilde{H} = \frac{1}{2} \begin{pmatrix} \Delta/2 - H & -1/2 & 0 & 0 & \cdot \\ -1/2 & \Delta + H & -1/2 & 0 & \cdot \\ 0 & -1/2 & \Delta - H & -1/2 & \cdot \\ 0 & 0 & -1/2 & \Delta + H & \cdot \\ \cdot & \cdot & \cdot & \cdot & \cdot \end{pmatrix} \quad (2.39)$$

and its diagonalization leads to the linear system

$$(\Delta/2 - H - \omega)C_1 = \frac{1}{2}C_2, \quad (2.40a)$$

$$[\Delta + (-1)^n H - \omega]C_n = \frac{1}{2}(C_{n+1} + C_{n-1}). \quad n = 2, 3, \dots \quad (2.40b)$$

or, by applying transformation (2.23),

$$(\Delta/2 - H - \omega)(\Delta/2 + H - \omega)A_1 = \frac{1}{4}(A_1 + A_2), \quad (2.41)$$

$$[(\Delta - \omega)^2 - H^2]A_n = \frac{1}{4}(2A_n + A_{n+1} + A_{n-1}) \quad n = 2, 3, \dots$$

supplemented by (2.25a).

The lowest lying mode turns out to be a surface mode of the special form

$$\begin{aligned} A_n &= \xi^n, \\ B_n &= \frac{1}{2} \frac{1 + \xi}{\Delta + H - \omega} \xi^n, \end{aligned} \quad n = 1, 2, \dots \quad (2.42)$$

provided that  $|\xi| < 1$  which guarantees that the state decays exponentially away from the boundary. Equations (2.41) reduce to

$$\begin{aligned}(\Delta/2 - H - \omega)(\Delta + H - \omega) &= \frac{1}{4}(1 + \xi), \\ (\Delta - \omega)^2 - H^2 &= \frac{1}{4}(2 + \xi + 1/\xi),\end{aligned}\tag{2.43}$$

which yield two distinct converging ( $|\xi| < 1$ ) surface modes.

The most interesting surface mode is given by the root  $\xi = \xi_1$  and  $\omega = \omega_1$  with

$$\begin{aligned}\xi_1 &= \frac{1}{2\Delta^2} \left[ \sqrt{(\Delta^2 + 4\Delta H - 1)^2 + 4\Delta^2} - (\Delta^2 + 4\Delta H - 1) \right], \\ \omega_1 &= \Delta - \sqrt{H^2 + \frac{1}{4}(2 + \xi_1 + 1/\xi_1)},\end{aligned}\tag{2.44}$$

which satisfies the convergence condition for  $H > -H_0$  with

$$H_0 = \frac{\Delta^2 - 1}{2\Delta}.\tag{2.45}$$

A second converging root is given by  $\xi = \xi_2$  and  $\omega = \omega_2$  with

$$\begin{aligned}\xi_2 &= -\frac{1}{2\Delta^2} \left[ \sqrt{(\Delta^2 + 4\Delta H - 1)^2 + 4\Delta^2} + (\Delta^2 + 4\Delta H - 1) \right], \\ \omega_2 &= \begin{cases} \Delta - \sqrt{H^2 + \frac{1}{4}(2 + \xi_2 + 1/\xi_2)} & -H_0 < H < 0, \\ \Delta + \sqrt{H^2 + \frac{1}{4}(2 + \xi_2 + 1/\xi_2)} & H < -H_0. \end{cases}\end{aligned}\tag{2.46}$$

The two branches of  $\omega_2$  join smoothly at  $-H_0$  while  $\xi_2$  lies in the interval  $-1 < \xi_2 < 0$  and thus the corresponding surface state decays away from the boundary in an oscillatory manner.

The calculated surface modes  $\omega_1$  and  $\omega_2$  are depicted in figure 2.14 by lines 1 and 2 respectively where we have also included the spectrum of the bulk AF state of equation (2.26). The lines 1' and 2' correspond to a surface with its ending spin in the  $+z$  direction so the spectrum of fig. 2.14 would actually be obtained by a chain consisted by an even number of spins.

Our results are verified by a numerical diagonalization of the Hessian which shows that the size dependence of the spectrum is rather weak. For

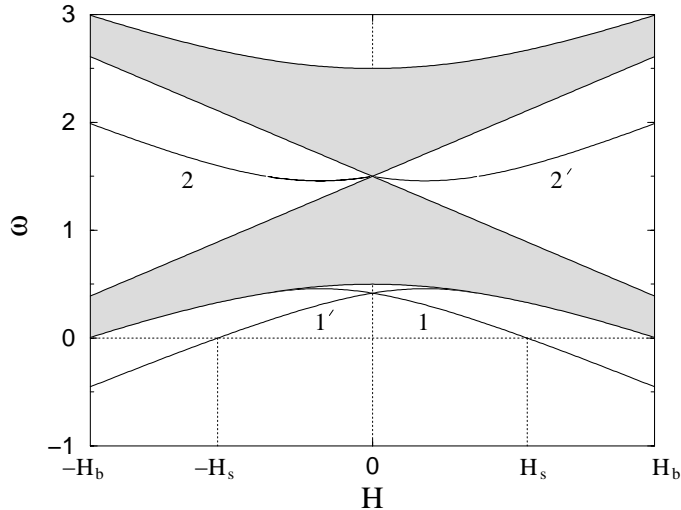


**Figure 2.14:** The spectrum of a finite system ( $\Lambda = 2N$ ) in the Néel state. We distinguish the surface modes 1, 1' and 2, 2' while the shaded region corresponds to the bulk continuum.

any given  $\Lambda = 2N$  the majority of eigenvalues fall within the shaded region of figure 2.14 but a finite number of eigenvalues occur outside the continuum, and are very accurately described by the analytically calculated frequencies  $\omega_1$  and  $\omega_2$ . The frequencies of the gap modes calculated analytically on a chain with  $\Delta = 1.125$  agree with the numerical results to several significant figures for  $\Lambda = 22$  while the agreement improves rapidly with increasing  $\Lambda$  or  $\Delta$ .

The most important conclusion derived from the preceding calculation is that  $\omega_1$  crosses zero for a field value  $H_s < H_b$  which is found from (2.44) to be

$$H_s = \frac{1}{4\Delta} \left[ \sqrt{(\Delta^2 - 1)(9\Delta^2 - 1)} - (\Delta^2 - 1) \right], \quad (2.47)$$

where the SSF transition takes place and the Néel state ceases to be the ground state. Our numerical experiments of section 2.4 give values for  $H_s$  which are in excellent agreement with those calculated from (2.47) thus verifying the picture derived from the stability analysis. We should mention here that there is also a second root  $H_e$  of  $\omega_1 = 0$ , namely

$$H_e = -\frac{1}{4\Delta} \left[ \sqrt{(\Delta^2 - 1)(9\Delta^2 - 1)} + (\Delta^2 - 1) \right], \quad (2.48)$$

where  $H_e < -H_0$  and therefore the corresponding eigenvector of equation

(2.44) is exponentially diverging away from the surface and we have to reject it. Finally, we can see from fig. 2.14 that the modes 1' and 2', related to a surface with its ending spin in the  $+z$  direction, can be found from the 1 and 2 modes by the transformation  $H \rightarrow -H$  and therefore the corresponding critical fields will be

$$H'_s = -H_s, \quad H'_e = -H_e. \quad (2.49)$$

We will now derive a condition for the determination of the critical field  $H_{[0]}$ . Here we adopt the convenient symbol  $|2n\rangle$  to denote an Ising domain wall located  $n$  steps away from the chain boundary, e.g.  $|0\rangle \equiv (\theta_n) = (0, 0, \pi, 0, \pi, 0, \dots)$ ,  $|2\rangle \equiv (\theta_n) = (0, \pi, 0, 0, \pi, 0, \dots)$  and so on. So  $H_{[0]}$  is the field for which the  $|0\rangle$  state becomes unstable and similarly  $H_{[2]}$  is the field corresponding to  $|2\rangle$  while the extreme member of this family will be  $H_{[\infty]}$  of equation (2.13).

The Hessian of the  $|0\rangle$  state is found to be

$$\tilde{H} = \frac{1}{2} \begin{pmatrix} -\Delta/2+H & 1/2 & 0 & 0 & 0 & \cdot \\ 1/2 & H & -1/2 & 0 & 0 & \cdot \\ 0 & -1/2 & \Delta-H & -1/2 & 0 & \cdot \\ 0 & 0 & -1/2 & \Delta+H & -1/2 & \cdot \\ 0 & 0 & 0 & -1/2 & \Delta-H & \cdot \\ \cdot & \cdot & \cdot & \cdot & \cdot & \cdot \end{pmatrix} \quad (2.50)$$

and its diagonalization leads to the following system

$$\begin{aligned} (-\Delta/2 + H - \omega)C_1 &= -\frac{1}{2}C_2, \\ (H - \omega)C_2 &= \frac{1}{2}(-C_1 + C_3), \\ [\Delta + (-1)^n H - \omega]C_n &= \frac{1}{2}(C_{n+1} + C_{n-1}), \quad n = 3, 4, \dots \end{aligned} \quad (2.51)$$

Similarly to the case of the DW in the bulk we apply transformation (2.23) and additionally set  $\omega = 0$  to find that the last of equations (2.51) has a solution of the form

$$\begin{aligned} A_n &= \zeta^{n-1}, \\ B_n &= \frac{1}{2} \frac{1 + \zeta}{\Delta + H} \zeta^{n-1} \equiv q \zeta^{n-1}, \end{aligned} \quad n = 2, 3, \dots \quad (2.52)$$

where  $\zeta$  must satisfy

$$\Delta^2 - H^2 = \frac{1}{4}(2 + \zeta + 1/\zeta), \quad (2.53)$$

while the remaining of equations (2.51) are written in the form

$$\begin{aligned} (-\Delta/2 + H)A_1 &= -\frac{1}{2}B_1 \\ HB_1 &= \frac{1}{2}(\zeta - A_1) \\ (\Delta - H)\zeta &= \frac{1}{2}(q\zeta + B_1). \end{aligned} \quad (2.54)$$

This last system leads to a unique equation for  $\zeta$

$$[2(\Delta - H)(\Delta + H) - \frac{1}{2}(1 + \zeta)][-\frac{1}{2} + H(2H - \Delta)] = (H - \frac{\Delta}{2})(\Delta + H) \quad (2.55)$$

which, combined with (2.53), yields an algebraic condition that determines the points  $(H, \Delta)$  at which  $\omega = 0$ , namely

$$16\Delta H^4 - 8(4\Delta^2 - 1)H^3 + 10\Delta(2\Delta^2 - 1)H^2 - (4\Delta^4 - 5\Delta^2 + 1)H - \Delta(\Delta^2 - 1) = 0. \quad (2.56)$$

This equation can be solved numerically and its roots in the upper-right quadrant of the  $(H, \Delta)$  plane bound from below the region of stability of the  $|0\rangle$  domain wall. Specifically, we find that there is a minimum value of  $\Delta \simeq 1.76$  below which equation (2.56) has no solutions and therefore  $|0\rangle$  never occurs, while for bigger anisotropies we find two positive solutions of (2.56)  $H_{[0]}^-, H_{[0]}^+$  which define the region of stability  $(H_{[0]}^-, H_{[0]}^+)$  of the state  $|0\rangle$ . Once again agreement of the  $H_{[0]}$  calculated from the equation above and the values obtained from the numerical experiments of section 2.4 is excellent.

Although we do not calculate the limits of stability of  $|2\rangle, |4\rangle, \dots, |2n\rangle$  here, the results show that the series of  $H_{[2n]}$  converges very fast to  $H_{[\infty]}$ . Specifically, only  $H_{[0]}$  differs from  $H_{[\infty]}$  while the other members of the family are practically indistinguishable from  $H_{[\infty]}$ .

## 2.6 The critical field $H_w$

We will now derive an analytical formula for the critical field  $H_w$  using an argument similar to that applied before for the single-ion model [32, 48].

The procedure of section 2.5 seems inapplicable because the ground state in the field region of  $H_w$  is non trivial making the explicit calculation and diagonalization of the Hessian impossible.

It is useful to note that the values of  $H_w$  obtained from our numerical experiments of section 2.4 coincide with the critical field  $H'_e$  of equation (2.49). For example the critical fields  $H_w$  depicted in figures 2.7 and 2.9 by the dotted line were calculated by formula (2.49) and we can see that the agreement is very good for the  $D = 1.125$  case.

The physical meaning of  $H_w$  can be understood by performing the following numerical experiment. We apply our relaxation algorithm on long systems with initial configurations slightly perturbed  $|2n\rangle$  states. Comparing the calculated energies of the resulting configurations we find that above  $H_w$  the energetically preferable location for a DW is as far from the surface as possible.

An analytical comparison of those energies, for the field region of interest, can be performed by using the following argument. For a semi-infinite system at  $H - H'_e \simeq 0$  the domain wall causes the surface spins to relax in a configuration given by the eigenvector of equation (2.44). Specifically, at  $H'_e$  this surface mode becomes static ( $\omega = 0$ ) and once we exceed  $H_w$  it becomes energetically preferable to the Néel state ( $\omega < 0$ ). This causes the DW to move towards the bulk in order to include as many tail spins as possible at the expense of the energy costing Néel spins infinitely into the bulk. Therefore, at  $H'_e$  the wall moves in the bulk in order to lower its energy thus verifying that  $H_w = H'_e$  or explicitly

$$H_w = \frac{1}{4\Delta} \left[ \sqrt{(\Delta^2 - 1)(9\Delta^2 - 1)} + (\Delta^2 - 1) \right]. \quad (2.57)$$

This critical field is present for those values of  $\Delta$  for which the DW is not of the Ising type and therefore interacts with the surface.

## 2.7 Phase diagram on a finite chain

We are now in a position to derive the phase diagram of the finite system with  $\Lambda = 2N$ , shown in figure 2.15. In comparison with the phase diagram of the infinite system (sec. 2.2) we find that the BSF and F phases remain as they were while the AF region has been divided in four subregions AF, SSF,

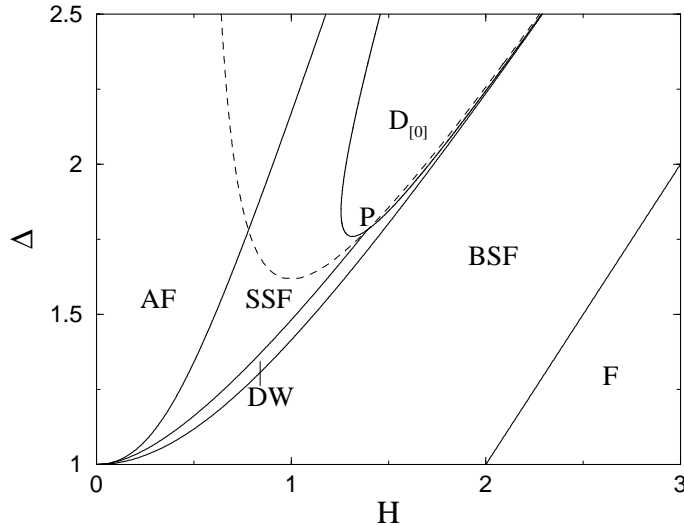


**Figure 2.15:** The phase diagram of the finite system.

DW,  $D_{[0]}$ , separated by the critical fields  $H_s$ ,  $H_w$ ,  $H_{[0]}$  respectively. Here we also display the critical field  $H_{[\infty]}$  depicted by the dashed line. One can see that the critical field  $H_w$  terminates at a point  $P$  where the lines  $H_{[0]}$  and  $H_w$  intersect. We find that at the point  $P$  all critical fields  $H_{[2n]}$  intersect, and we therefore call it the multicritical point which is numerically calculated to be  $P = (\Delta_P, H_P) = (1.7807764, 2.7807764)$ . The existence of such a multicritical point has also been observed in the single-ion model describing Fe/Cr superlattices [32,33] whose phase diagram shares many common features with that of our model.

In the AF phase the ground state is the well known Néel state of fig. 2.1. Once we cross  $H_s$  the SSF transition takes place and the system enters the SSF phase where the lowest energy state is the surface state of section 2.4, also described in Appendix A. Above  $H_w$  and for  $\Delta$  under  $\Delta_P$  we enter the DW phase, in which the energy is minimized through an “up” DW as far from the surfaces as possible, which at  $H_b$  gives its place to the BSF phase and finally to the F phase for fields above  $H_f$ . For anisotropies above  $\Delta_P$  once we reach the critical field  $H_{[0]}$  the surface state of lowest energy becomes the  $|0\rangle$  state until we cross  $H_{[\infty]}$  where the ground state becomes an extended domain wall at the center of the chain. Again at  $H_b$  and  $H_f$  we enter the BSF and F phases respectively.

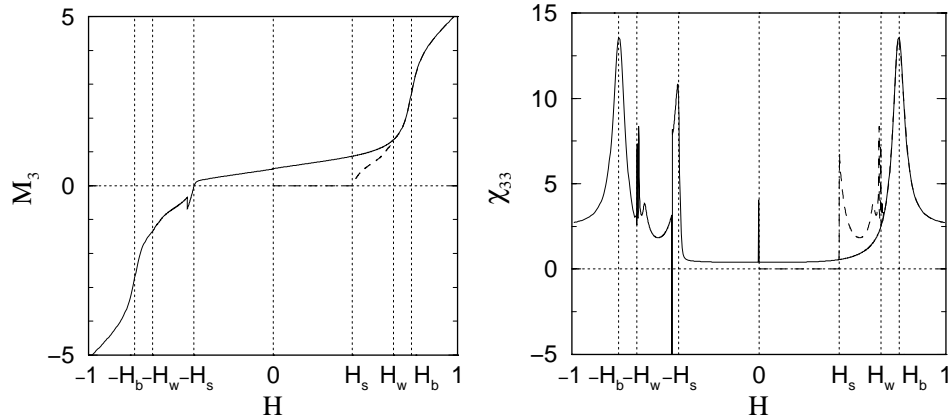


**Figure 2.16:** Field dependence of the total magnetization and susceptibility for an open chain with  $\Lambda = 22$  sites and  $\Delta = 1.25$  for a hysteresis numerical experiment. The dashed line depicts the values corresponding to the increase of the field from  $H = 0$  to  $H_f$  (as described in section 2.4) while the continuous line depicts the values obtained while decreasing  $H$  from  $H_f$  to  $-H_f$ .

As we have seen in numerical experiments the system will not always relax in the ground state, because of local minima in the energy. Their role becomes even more important in the following discussion of the hysteresis.

## 2.8 Hysteresis of the spin-flop transition

In order to investigate hysteresis phenomena we perform the following numerical experiment. Beginning from the Néel state at  $H = 0$  we increase the magnetic field until ferromagnetic saturation is reached, and we then decrease  $H$  in small steps down to  $H = -H_f$ . For every value of the field we use as initial configuration for our relaxation algorithm the stable configuration of the previous field value  $H - dH$  slightly perturbed in a random way.

In figure 2.16 we show the magnetization and susceptibility of a system of  $\Lambda = 22$  and  $\Delta = 1.25$ . The dashed lines depict the results obtained while we increase the field where we can see the peaks in the susceptibility around  $H_s$ ,  $H_w$  and  $H_b$  caused by the SSF and BSF transitions taking place, as described in section 2.4. The continuous line depict the results corresponding to fields decreasing from  $H_f$  to  $-H_f$ . We note that the two lines coincide down to  $H_w$  but separate for smaller fields. Furthermore, the magnetization takes

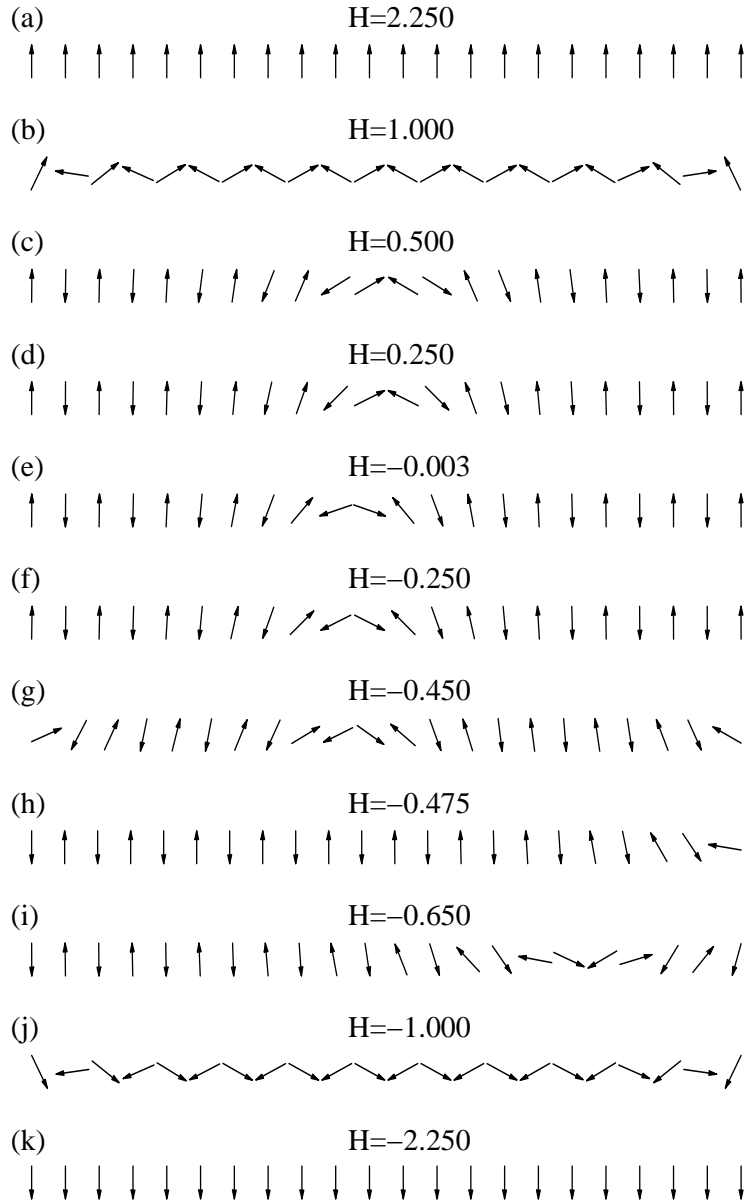


**Figure 2.17:** The spin configurations for  $\Delta = 1.25$ ,  $\Lambda = 22$  for fields decreasing from  $H_f$  to  $-H_f$ .

non zero values for all positive field values suggesting that the system does not return to the Néel state. One can check that in the region  $0 < H < H_b$  the magnetization actually coincides with the magnetization curve of a bulk DW which is known [46, 34] to take non-zero values even for vanishing field.

The spin configurations of fig. 2.17a-d reveal that as we decrease the magnetic field the canted state of  $H \geq H_b$  evolves into an “up” DW in the center of the chain which sustains all the way down to  $H = 0$ . Once we apply negative magnetic field the DW becomes energetically unfavorable and moves by one site to lower its energy (fig. 2.17e) causing a sharp peak in the susceptibility. At  $H \lesssim -H_s$  a surface state is generated at both ends of the chain (fig. 2.17g) and by further decreasing the field the wall annihilates with one<sup>2</sup> of the surface states (fig. 2.17h) leaving the system in a surface state at its other end. The surface state now evolves with the field as we have described before in section 2.4 first to a DW at  $H \simeq H_w$  (fig. 2.17i) and then to the canted state once we reach  $H_b$  (fig. 2.17j).

The picture presented above strongly depends on the anisotropy and lattice size. For anisotropies for which the width of the formed DW at  $H = H_w$  is comparable to the size of the chain once the field becomes lower than  $H_w$  the wall moves towards the surface following an inverse SSF transition leading to the Néel state at  $H = H_s$  thus producing no hysteresis loop. When the dimension of the system is large compared with the width of the DW (that is for large anisotropies) the interaction of the wall with the surface is not enough to overcome the barriers encountered in its movement and the DW remains in the center evolving as in the  $\Delta = 1.25$  case presented above.

## 2.9 The odd chain

The case of the odd chain does not add anything fundamentally new as all the occurring phenomena can be derived from our analysis of the even chain. We can distinguish two cases for the study of the odd chain depending on the direction of the ending spins relatively to the bias field.

The simplest case is for applied field in the direction of the ending spins. In figure 2.18 we see the magnetization and the susceptibility per site ob-

---

<sup>2</sup>The one that is closer to the DW.

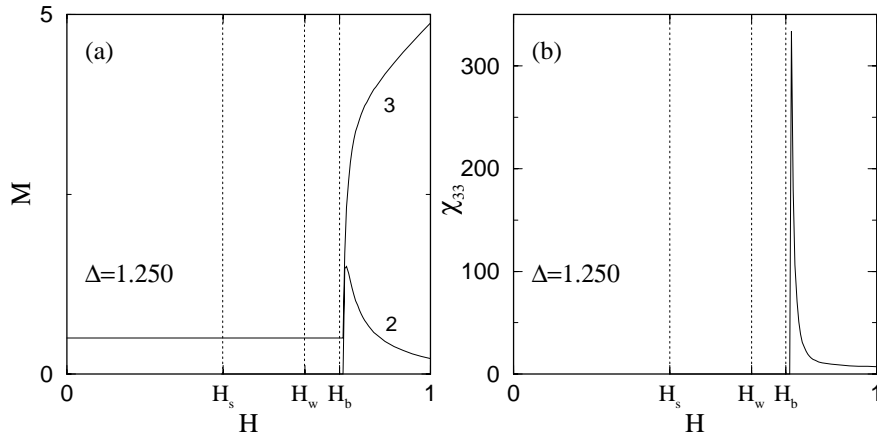


**Figure 2.18:** The magnetization and susceptibility per site of a system with  $\Lambda = 21$  and  $\Delta = 1.250$  and the two ending spins parallel to the magnetic field.

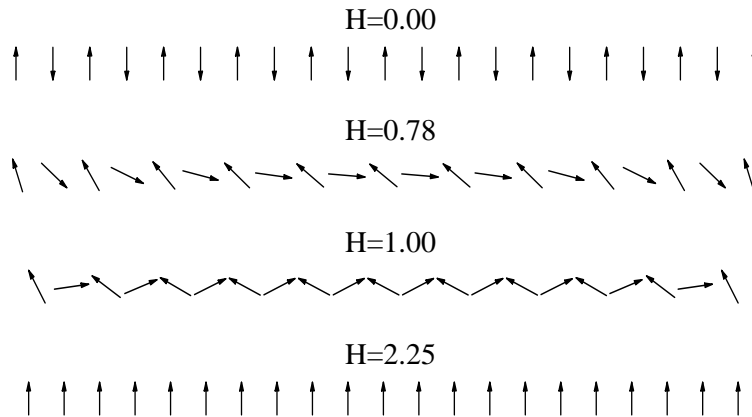


**Figure 2.19:** The spin configurations for  $\Delta = 1.25$ ,  $\Lambda = 21$  for a characteristic set of field values. The critical fields for this  $\Delta$  are  $H_s = 0.43$ ,  $H_w = 0.65$ ,  $H_b = 0.75$ ,  $H_f = 2.25$ .

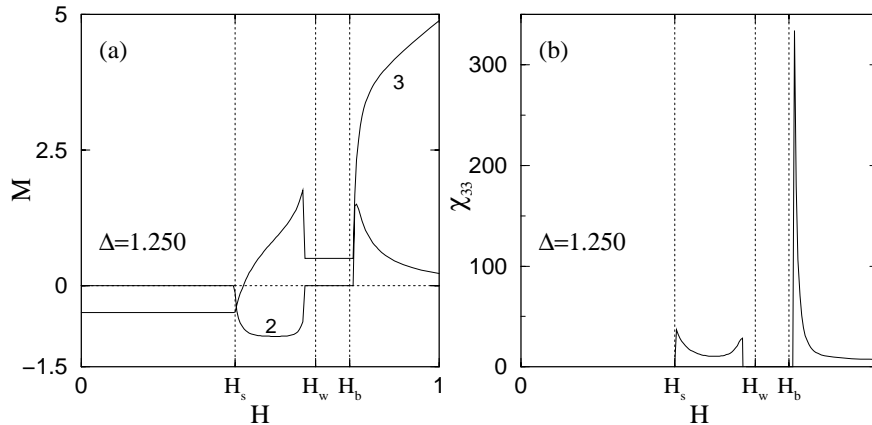


**Figure 2.20:** Field dependence of the total magnetization and susceptibility for an open chain with  $\Lambda = 21$  sites,  $\Delta = 1.250$  and both ending spins, initially, antiparallel to the bias field. (a) The two nonvanishing components of the magnetization  $M_2$  and  $M_3$ . (b) The diagonal susceptibility  $\chi_{33}$  defined as in equation (2.18).

tained by a simulation of a system of  $\Lambda = 21$  and  $\Delta = 1.250$ . We notice that there is no structure present around  $H_s$  and  $H_w$  implying that the SSF transition do not occur.

The corresponding spin configurations of figure 2.19 verify that the system remains in its Néel positions until  $H_b$  where the BSF transition takes place and the canted state becomes the lowest energy state. Finally, when the critical field exceeds  $H_f$  the system reaches ferromagnetic saturation. Therefore for fields in the direction of the ending spins the phase diagram coincides with that of the infinite chain.

On the other hand, if we apply a bias field antiparallel to the ending spins once we reach  $H_s$  a surface spin flop transition takes place at both ends of the chain developing into two DW's moving towards the center of the chain with increasing field. These two DW's evolve independently as described in the even spin chain, as long as they are not close enough for their interaction to become important. Once they approach they annihilate each other to leave the system in a Néel state with both ending spins parallel to the bias field. The evolution of the chain now proceeds as in the previous case (where the ending spins were initially in the direction of the bias field) with the Néel state giving its place to the canted state at  $H_b$  and then to the ferromagnetic

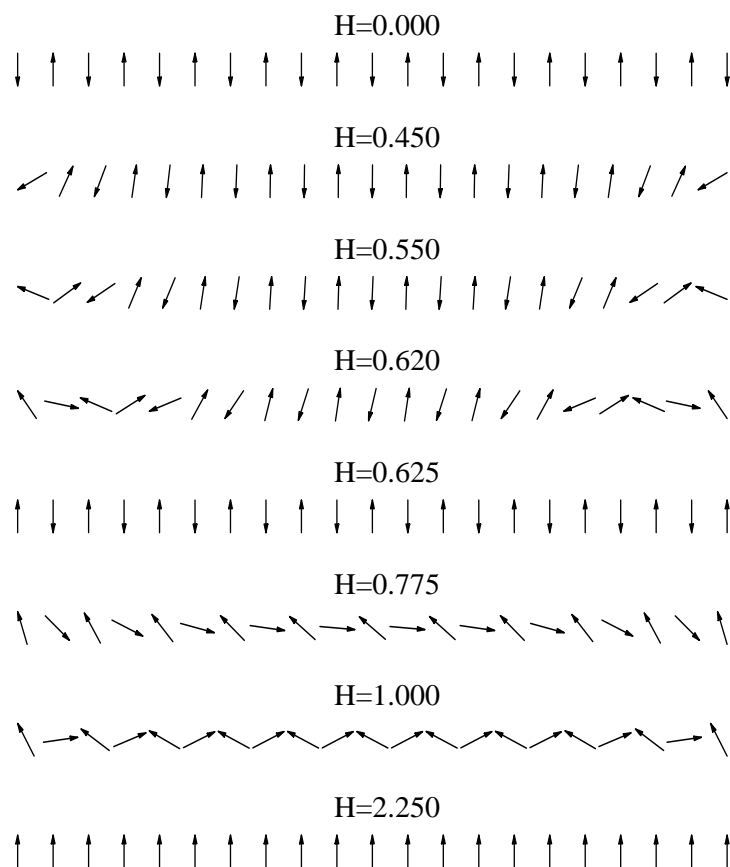


**Figure 2.21:** The spin configurations for  $\Delta = 1.250$ ,  $\Lambda = 21$  and a characteristic set of field values. The critical fields for this case are  $H_s = 0.43$ ,  $H_w = 0.65$ ,  $H_b = 0.75$ ,  $H_f = 2.25$ .

state for  $H \geq H_f$ .

The field at which the annihilation of the two DW's takes place depends on the width and the relative positions of the DW's which are relevant to the values of  $\Delta$  and  $\Lambda$ . One expects that this field would generally be in the region of  $H_w < H < H_b$ . The picture described above is shown in figures 2.20 and 2.21.

## 2.10 Conclusion

We have seen that our system described by the effective potential (2.4) is characterized by a surface and a bulk spin flop transition for all values of the anisotropy  $\Delta$ . We have provided the phase diagram with a detailed description of the different phases and we have pointed out the importance of local energy minima in the evolution of the system with the magnetic field. Furthermore, our numerical relaxation algorithm, in contrast to a straight energy minimization procedure, allows us to probe the odd chain and the hysteresis of the SSF transition.

One should note here that the emerging picture shares several common features with the one derived within the single-ion model of the magnetic superlattices [29–35] which make our model helpful for the understanding of some of the dark points of the SSF transition. On the other hand, there are some important differences. For example, the critical fields  $H_s$  and  $H_w$  coincide in the single ion model leading to a more involved picture partly responsible for some confusion on that subject. Moreover the BSF transition in our model, although a first order one, is characterized by a single critical field while in the single ion case by three such fields. Yet, the differences of the two models smooth out for small anisotropies as they share the same continuous limit.



## CHAPTER 3

# QUANTUM THEORY

### 3.1 Introduction

In this chapter we study [43] the spin-flop transition in a quantum spin- $\frac{1}{2}$  system described by Hamiltonian (1.1) for the special choice of exchange constants

$$-J_1 = J_2 \equiv 1, \quad J_3 \equiv \Delta > 1, \quad (3.1)$$

which is consistent with inequalities (2.1). We find that this choice gives the most classical antiferromagnet e.g. if  $u$  and  $d$  denote spin-up and spin-down states, the two fully polarized Néel states

$$|N_A\rangle = |d, u, d, u, \dots\rangle, \quad |N_B\rangle = |u, d, u, d, \dots\rangle, \quad (3.2)$$

are the two (degenerate) exact ground states when the applied field is sufficiently weak.

The study of the quantum mechanical problem at zero temperature requires the determination of the ground state from which we calculate the mean values of the desired observables. The numerical diagonalization of the Hamiltonian is only possible for small systems since the dimension of the Hilbert space grows as  $2^A$ . Yet, significant analytical progress can be made for the specific choice (3.1) which may serve as a prototype for further consideration of the full range of models defined by inequalities (2.1).

Some special features of model (3.1) become apparent by performing the

familiar canonical transformation

$$S_n^x = T_n^x, \quad S_n^y = (-1)^n T_n^y, \quad S_n^z = (-1)^n T_n^z, \quad (3.3)$$

where the ‘pseudospin’ variables  $\mathbf{T}_n$  again satisfy the standard spin commutation relations and map the Hamiltonian to

$$W = - \sum_{n=1}^{\Lambda-1} \left[ T_n^x T_{n+1}^x + T_n^y T_{n+1}^y + \Delta \left( T_n^z T_{n+1}^z - \frac{1}{4} \right) \right] - H \sum_{n=1}^{\Lambda} (-1)^n T_n^z, \quad (3.4)$$

which describes an easy-axis ‘ferromagnet’ in a staggered magnetic field. In equation (3.4) we have included a trivial additive constant to provide a convenient normalization for the energy eigenvalues.

It is clear from equation (3.4) that the model (3.1) is also endowed with a  $U(1)$  symmetry because the total azimuthal pseudospin

$$\tau = \sum_{n=1}^{\Lambda} T_n^z = \sum_{n=1}^{\Lambda} (-1)^n S_n^z, \quad (3.5)$$

obviously commutes with the Hamiltonian and thus the Hilbert space breaks up into  $\Lambda + 1$  sectors characterized by the good quantum number  $\tau = \Lambda/2 - \lambda$  with  $\lambda = 0, 1, \dots, \Lambda$ . Although this observation will greatly simplify calculations, the quantum number  $\tau$  is not related to a simple physical observable. Instead we shall be interested in the total azimuthal magnetization

$$M = \sum_{n=1}^{\Lambda} S_n^z = \sum_{n=1}^{\Lambda} (-1)^n T_n^z, \quad (3.6)$$

which does not commute with the Hamiltonian and its expected values cannot be predicted by simple quantization. One of our objectives in the following is to determine the ground-state expectation value  $M = M(\Delta, H)$  as a function of anisotropy  $\Delta$  and applied field  $H$ .

In section 3.2 we provide a complete calculation of one-magnon excitations with or without open boundaries. These results already suggest the occurrence of a bulk spin-flop (BSF) transition at a critical field  $H_b$ , which is preceded by a surface spin-flop (SSF) transition at a new critical field  $H_s < H_b$  in the presence of open boundaries. The two types of transition are analyzed in sections 3.3 and 3.4. Antiferromagnetic domain walls arise

naturally in the description of the SSF transition and are thus also discussed in section 3.4. In section 3.5 we summarize some of our main conclusions, and present the phase diagram, while in section 3.6 we discuss the necessary modifications for the case of an odd chain ( $\Lambda = 2N + 1$ ). Some preliminary results for other quantum spin models in the range of inequalities (2.1) are presented in section 3.7, and our conclusions are summarized in section 3.8.

### 3.2 One-magnon spectrum

The eigenstates of the Hamiltonian (3.4) are linear superpositions of states of the form  $|\tau_1, \tau_2, \dots, \tau_\Lambda\rangle$  where the  $\tau_n$ 's take the values  $1/2$  or  $-1/2$  in any combination that preserves their sum  $\tau$ . The Néel states (3.2) are mapped to two completely polarized ‘ferromagnetic’ states  $|F_A\rangle, |F_B\rangle$ , with  $\tau = \pm\Lambda/2$ , which are exact eigenstates, with energy  $E = 0$ , for any value of the applied field. It is also clear that these are the two degenerate ground states at vanishing field. The first question is then to determine the field region over which the polarized states persist as the ground states of the system.

One is thus lead to study excitations, the simplest possibilities being one-magnon modes with  $\tau = \Lambda/2 - 1$  or  $-\Lambda/2 + 1$ . It is sufficient to consider only the former case, information about the latter being inferred by extending the field region to both positive and negative values of  $H$ . The one-magnon eigenvalue problem reads

$$W|\psi\rangle = E|\psi\rangle, \quad |\psi\rangle = \sum_{n=1}^{\Lambda} C_n |n\rangle, \quad (3.7)$$

where we have simplified the notation by asserting that  $|n\rangle$  is the state where  $\tau_n = -1/2$  but all other  $\tau$ 's are equal to  $1/2$ . An explicit form of the eigenvalue equations is then given by

$$\begin{aligned} (\Delta/2 - H - E)C_1 &= \frac{1}{2}C_2, \\ [\Delta + (-1)^n H - E]C_n &= \frac{1}{2}(C_{n+1} + C_{n-1}), \quad n = 2, 3, \dots, \Lambda - 1, \\ (\Delta/2 + H - E)C_\Lambda &= \frac{1}{2}C_{\Lambda-1}, \end{aligned} \quad (3.8)$$

and are valid on an open chain with  $\Lambda$  sites. Comparing (3.8) with (2.22) we can see that the one-magnon spectrum actually coincides with that of the

quadratic fluctuations of the Néel state already performed in section 2.5. Yet, we will repeat the calculation here for reasons of completeness. Throughout this chapter we assume that the chain is even ( $\Lambda = 2N$ ) with the exception of section 3.6 where we deal with the problem of the odd chain. We now introduce the sublattice variables

$$A_n = C_{2n-1}, \quad B_n = C_{2n}, \quad n = 1, 2, \dots, N, \quad (3.9)$$

in terms of which the linear system (3.8) reads

$$\begin{aligned} (\Delta/2 - H - E)A_1 &= \frac{1}{2}B_1, \\ (\Delta - H - E)A_n &= \frac{1}{2}(B_{n-1} + B_n), \quad n = 2, 3, \dots, N, \\ (\Delta + H - E)B_n &= \frac{1}{2}(A_n + A_{n+1}), \quad n = 1, 2, \dots, N - 1, \\ (\Delta/2 + H - E)B_N &= \frac{1}{2}A_N. \end{aligned} \quad (3.10)$$

It is instructive to consider in parallel a cyclic or periodic chain with the same number of sites, in order to establish a simple reference case which will enable us to better appreciate surface effects that may arise on an open chain. The first and fourth equations in (3.10) are absent on a cyclic chain, and the remaining two equations are valid for all  $n = 1, 2, \dots, N$ . It is then a straightforward matter to eliminate  $B_n$  to obtain the equivalent system

$$\begin{aligned} B_n &= \frac{1}{2} \frac{A_n + A_{n+1}}{\Delta + H - E}, \\ [(\Delta - E)^2 - H^2] A_n &= \frac{1}{4}(2A_n + A_{n+1} + A_{n-1}), \end{aligned} \quad (3.11)$$

whose solution is  $A_n = e^{ikn}$ , where  $k = 2\pi\nu/N$  with  $\nu = 0, 1, \dots, N - 1$  is a sublattice crystal momentum, provided that the energy is given by

$$E = \Delta \pm \sqrt{H^2 + \cos^2(k/2)}. \quad (3.12)$$

Viewed as functions of the applied field the energy eigenvalues are contained within the two shaded regions of figure 2.14 and their distribution becomes increasingly dense in the bulk limit  $N \rightarrow \infty$ . The shaded regions are bounded from above and below by the two curves  $E = \Delta \pm \sqrt{H^2 + 1}$  and display a

middle gap extended between the straight lines  $E = \Delta \pm H$ . The lowest gap closes ( $E = 0$ ) at  $H = \pm H_b$  where

$$H_b = \sqrt{\Delta^2 - 1}, \quad (3.13)$$

is a critical field of special importance in the following. The preceding derivation already indicates that the simple Néel states (3.2) can no longer be the ground states for field values outside the interval  $[-H_b, H_b]$ . Further analysis of the cyclic chain given in section 3.3 will establish that  $H_b$  provides the critical boundary of the BSF transition.

We now return to the main theme and examine the possibility of one-magnon surface modes on an open chain. Solution of the linear system (3.10) is complicated by the appearance of the two distinct equations at the outer layers. However the essential new ingredients can be obtained analytically on a semi-infinite chain. The fourth equation in (3.10) may then be ignored and the third may again be used to eliminate  $B_n$  as in equation (3.11). The first two equations are written as

$$\begin{aligned} (\Delta/2 - H - E)(\Delta + H - E)A_1 &= \frac{1}{4}(A_1 + A_2), \\ [(\Delta - E)^2 - H^2] A_n &= \frac{1}{4}(2A_n + A_{n+1} + A_{n-1}), \end{aligned} \quad (3.14)$$

where  $n = 2, 3, \dots, \infty$ . A surface mode is described by a special solution of the form

$$A_n = \xi^n, \quad B_n = \frac{1}{2} \frac{1 + \xi}{\Delta + H - E} \xi^n, \quad (3.15)$$

supplemented by the requirement  $|\xi| < 1$  which guarantees that the state decay exponentially away from the boundary. Equations (3.14) reduce to

$$\begin{aligned} (\Delta/2 - H - E)(\Delta + H - E) &= \frac{1}{4}(1 + \xi), \\ (\Delta - E)^2 - H^2 &= \frac{1}{4}(2 + \xi + 1/\xi), \end{aligned} \quad (3.16)$$

and should be viewed as a system of two algebraic equations for the unknowns  $\xi$  and  $E$ . Detailed examination of the roots that satisfy the condition  $|\xi| < 1$  yields two distinct surface modes which we discuss in turn.

The most interesting surface mode is given by the root  $\xi = \xi_1$  and  $E = E_1$  with

$$\xi_1 = \frac{1}{2\Delta^2} \left[ \sqrt{(\Delta^2 + 4\Delta H - 1)^2 + 4\Delta^2} - (\Delta^2 + 4\Delta H - 1) \right],$$

$$E_1 = \Delta - \sqrt{H^2 + \frac{1}{4}(2 + \xi_1 + 1/\xi_1)}, \quad (3.17)$$

and its energy labeled as curve 1 in figure 2.14 lies below the one-magnon continuum. This curve emanates from the continuum at the characteristic field  $-H_0$  with

$$H_0 = \frac{\Delta^2 - 1}{2\Delta}, \quad (3.18)$$

and persists in the field region  $H > -H_0$ . The parameter  $\xi_1$  is equal to unity at  $-H_0$  but lies in the interval  $0 < \xi_1 < 1$  for  $H > -H_0$ . The surface state exists as a distinct gap mode below the continuum even at vanishing field ( $H = 0$ ) where  $\xi_1 = 1/\Delta^2$  and  $E_1 = (\Delta^2 - 1)/2\Delta$ . This special limit coincides with a result obtained by Johnson and Bonner [49] in their study of the ferromagnetic XXZ chain.

A second root satisfying the condition  $|\xi| < 1$  is given by  $\xi = \xi_2$  and  $E = E_2$  with

$$\xi_2 = -\frac{1}{2\Delta^2} \left[ \sqrt{(\Delta^2 + 4\Delta H - 1)^2 + 4\Delta^2} + (\Delta^2 + 4\Delta H - 1) \right], \quad (3.19)$$

$$E_2 = \begin{cases} \Delta - \sqrt{H^2 + \frac{1}{4}(2 + \xi_2 + 1/\xi_2)} & -H_0 < H < 0, \\ \Delta + \sqrt{H^2 + \frac{1}{4}(2 + \xi_2 + 1/\xi_2)} & H < -H_0. \end{cases}$$

The two branches in  $E_2$  join smoothly at  $-H_0$  and their union is labeled as curve 2 in figure 2.14. Therefore the second root describes a surface mode with energy in the middle gap of the magnon continuum. The parameter  $\xi_2$  lies in the interval  $-1 < \xi_2 < 0$  and thus the middle-gap mode decays away from the boundary in an oscillatory manner.

To complete the description of figure 2.14 we must now reconcile the preceding analytical results on a semi-infinite chain with those obtained by numerical diagonalization of the linear system (3.8) or (3.10) on a finite open chain. For any given  $\Lambda = 2N$  the majority of eigenvalues fall within the shaded regions of figure 2.14, but a finite number of eigenvalues occur outside the continuum for each field  $H$ . Also note that a duplication of gap modes should be expected on an open chain because surface states can now be formed near either one of the two free ends. Indeed, in addition to

confirming the gap modes 1 and 2 predicted on a semi-infinite chain, the numerical diagonalization also yields the two mirror modes 1' and 2' shown in figure 2.14.

The energies of the gap modes calculated analytically on a semi-infinite chain with  $\Delta = 1.5$  agree with the numerical results to several significant figures for  $\Lambda \sim 10$ , while the agreement improves rapidly with increasing  $\Lambda$  or  $\Delta$ . Hence the numerical simulations described in sections 3.3 and 3.4 for chains of modest size are expected to provide a reliable picture for most values of  $\Delta$  of practical interest.

The most important conclusion derived from the one-magnon calculation becomes apparent by simple inspection of figure 2.14. The surface modes in the lower gap are degenerate with the Néel states at the critical fields  $\pm H_s$ . The field  $H_s$  is computed from the condition  $E_1 = 0$  where  $E_1$  is given by equation (3.17). A straightforward calculation shows that

$$H_s = \frac{1}{4\Delta} \left[ \sqrt{(\Delta^2 - 1)(9\Delta^2 - 1)} - (\Delta^2 - 1) \right]. \quad (3.20)$$

Outside the interval  $[-H_s, H_s]$  the Néel states cease to be the lowest-energy states. Therefore the BSF transition anticipated to occur at the critical field  $H_b$  of equation (3.13) is preceded on an open chain by a SSF transition at  $H_s < H_b$ . The critical fields  $H_s$  and  $H_b$  coincide with those found in the classical calculation of chapter 2.

### 3.3 Bulk spin-flop transition

In this section we focus on a cyclic chain with an even number of sites and examine in greater detail the BSF transition at the critical field  $H_b$  of equation (3.13) suggested by the one-magnon calculation. In a curious turn of events, the recent work of Alcaraz et al [36] on an open spin chain in the presence of suitable boundary fields proved to be very instructive for the current work on a cyclic chain in a bulk bias field  $H$ .

We may also invoke the cluster argument of Bader and Schilling [39] on a cyclic chain noting that the Hamiltonian may then be written as a sum of cell Hamiltonians, namely

$$W = \sum_{n=1}^{\Lambda} W_n,$$

$$\begin{aligned}
 W_n = & - \left[ T_n^x T_{n+1}^x + T_n^y T_{n+1}^y + \Delta \left( T_n^z T_{n+1}^z - \frac{1}{4} \right) \right] \\
 & - \frac{1}{2} H (-1)^n (T_n^z - T_{n+1}^z),
 \end{aligned} \tag{3.21}$$

and thus the ground-state energy  $E_0$  satisfies the inequality

$$\frac{1}{2} \Lambda (E_+ + E_-) \leq E_0, \tag{3.22}$$

where  $E_{\pm}$  are the ground-state energies of the two-spin Hamiltonians

$$W_{\pm} = - \left[ T_1^x T_2^x + T_1^y T_2^y + \Delta \left( T_1^z T_2^z - \frac{1}{4} \right) \right] \pm \frac{1}{2} H (T_1^z - T_2^z). \tag{3.23}$$

The eigenvalues of both  $W_+$  and  $W_-$  are given by

$$\frac{1}{2} \left( \Delta + \sqrt{H^2 + 1} \right), \quad 0, \quad 0, \quad \frac{1}{2} \left( \Delta - \sqrt{H^2 + 1} \right), \tag{3.24}$$

where the first eigenvalue is always positive and the fourth one may be positive or negative depending on the field strength  $H$ . Therefore inequality (3.22) is written as

$$\Lambda \min \left[ 0, \frac{1}{2} \left( \Delta - \sqrt{H^2 + 1} \right) \right] \leq E_0 \leq 0, \tag{3.25}$$

and has been supplemented by  $E_0 \leq 0$  which follows from the fact that the polarized states are eigenstates of the complete Hamiltonian with vanishing energy for any value of the applied field. An immediate consequence of (3.25) is that the true ground-state energy vanishes when  $-H_b \leq H \leq H_b$ , where  $H_b$  is precisely the critical field (3.13), and thus coincides with the energy of the polarized states.

The preceding result strengthens the conclusion that the BSF transition occurs at the critical field  $H_b$  but a more detailed argument is required to determine the precise nature of the transition. The work of section 3.2 already established that the lowest-energy state in the one-magnon sector becomes degenerate with the polarized states at  $H_b$ . We shall further show that the lowest-energy states of all multimagnon sectors become degenerate at the same critical field, in analogy with a similar result in the model of reference 36. When  $H = H_b$  it is convenient to introduce the parameterization

$$\Delta = \frac{1}{2} \left( q + \frac{1}{q} \right), \quad H = \frac{1}{2} \left( q - \frac{1}{q} \right), \tag{3.26}$$

### 3.3. Bulk spin-flop transition

---

where  $\Delta > 1$  and  $q = \Delta + \sqrt{\Delta^2 - 1} > 1$ .

To motivate the demonstration we return to the one-magnon calculation and specifically consider the lowest-energy state at  $H_b$  obtained by setting  $k = 0$  and  $E = 0$  in equations (3.11) and (3.12) to yield  $A_n = 1$  and  $B_n = 1/q$  for all  $n = 1, 2, \dots, N$ . In the notation of equation (3.7) this special one-magnon state reads

$$C_n = q^{-\frac{1}{2}(-1)^n}, \quad (3.27)$$

where we have also included an overall normalization factor  $\sqrt{q}$ .

We next consider the two-magnon eigenvalue problem

$$W|\psi\rangle = E|\psi\rangle, \quad |\psi\rangle = \sum_{n_1 < n_2} C(n_1, n_2)|n_1, n_2\rangle, \quad (3.28)$$

where  $|n_1, n_2\rangle$  is a state with  $\tau_{n_1} = -1/2 = \tau_{n_2}$  and all other  $\tau$ 's equal to  $1/2$ . On a cyclic chain the generic eigenvalue equation is

$$\begin{aligned} & \{2\Delta + [(-1)^{n_1} + (-1)^{n_2}]H - E\} C(n_1, n_2) \\ &= \frac{1}{2} [C(n_1 + 1, n_2) + C(n_1 - 1, n_2) + C(n_1, n_2 + 1) \\ &+ C(n_1, n_2 - 1)], \end{aligned} \quad (3.29)$$

and should be completed with the meeting condition [12, 14]

$$\Delta C(n, n + 1) = \frac{1}{2} [C(n, n) + C(n + 1, n + 1)], \quad (3.30)$$

where one formally extends the definition of  $C(n_1, n_2)$  to coinciding arguments ( $n_1 = n_2$ ) which are absent in equation (3.28). When  $\Delta$  and  $H$  are given by equation(3.26) the wavefunction

$$C(n_1, n_2) = q^{-\frac{1}{2}[(-1)^{n_1} + (-1)^{n_2}]}, \quad (3.31)$$

satisfies equation (3.28), with  $E = 0$ , as well as the meeting condition (3.30). We have thus obtained a special two-magnon eigenstate which is degenerate with both the one-magnon state (3.27) and the completely polarized states at the critical field  $H_b$ .

These elementary results possess a simple generalization to an arbitrary sector. A set of exact eigenstates with vanishing energy is given by

$$|\psi_\tau\rangle = \sum_{\{\tau\}} q^{\frac{1}{2}\sum_{n=1}^{\Lambda} (-1)^n \tau_n} |\tau_1, \tau_2, \dots, \tau_\Lambda\rangle, \quad (3.32)$$

where the sum extends over all configurations  $\{\tau\} = (\tau_1, \tau_2, \dots, \tau_\Lambda)$  which are consistent with a definite azimuthal pseudospin

$$\tau = \sum_{n=1}^{\Lambda} \tau_n = N, N-1, \dots, -N, \quad (3.33)$$

where  $\Lambda = 2N$ . As a check of consistency one may apply equation (3.32) for  $\tau = N-1$  and  $N-2$  to recover the one- and two-magnon wavefunctions (3.27) and (3.31). For other values of  $\tau$  our basic result (3.32) can be established by a straightforward generalization of the two-magnon calculation given above.

A numerical calculation of all eigenstates and eigenvalues, for various  $\Lambda \leq 14$ , confirms that the ground states of all sectors become degenerate at the critical field. Excited states also exhibit some ‘accidental’ degeneracy that cannot be accounted for by the  $U(1)$  symmetry. One is thus tempted to conclude that the model acquires a larger symmetry at the critical point, perhaps analogous to the quantum-group  $U_q[SU(2)]$  symmetry of the model with boundary fields studied in Refs. 36, 50. We shall not pause to examine the possibility of a hidden symmetry in the present model because the explicit result (3.32) proves to be sufficient to illuminate the nature of the BSF transition.

The special form of the eigenvectors (3.32) at  $H = H_b$  allow us to calculate the magnetization  $M_\tau$  on an even cyclic chain of any size for each sector  $\tau$ . Specifically one can easily check that the magnetization can be written as

$$M_\tau = \sum_{n=1}^{\Lambda} (-1)^n \frac{\langle \psi_\tau | T_n^z | \psi_\tau \rangle}{\langle \psi_\tau | \psi_\tau \rangle} = q \frac{\partial}{\partial q} \ln \langle \psi_\tau | \psi_\tau \rangle, \quad (3.34)$$

and the problem reduces to the calculation of the norm  $\langle \psi_\tau | \psi_\tau \rangle$ . A reasonable amount of combinatorics leads to

$$\langle \psi_\tau | \psi_\tau \rangle = \sum_{\nu=0}^{N-\tau} \left[ \frac{N!}{(N-\nu)!\nu!} \right] \left[ \frac{N!}{(N-\tau-\nu)!(\tau+\nu)!} \right] q^{N-\tau-2\nu} \quad (3.35)$$

that can be written in the integral representation

$$\langle \psi_\tau | \psi_\tau \rangle = \frac{2^N}{\pi} \int_0^\pi \cos(\theta\tau) (\Delta + \cos\theta)^N d\theta \equiv I_N^\tau. \quad (3.36)$$

Combining equations (3.34), (3.36) we obtain

$$M_\tau = \sqrt{\Delta^2 - 1} \frac{I_{N-1}^\tau}{I_N^\tau}. \quad (3.37)$$

A simple application of the Laplace method [51] yields the asymptotic expansion

$$M_\tau = \left(N + \frac{1}{2}\right) \sqrt{\frac{\Delta - 1}{\Delta + 1}} + \frac{1 - 4\tau^2}{8N} \sqrt{\Delta^2 - 1} + O(1/N^2), \quad (3.38)$$

from which we can derive the magnetization of any sector  $\tau$  in the thermodynamic limit.

The emerging qualitative picture of the BSF transition is substantiated with an explicit calculation of the ground-state expectation value of the total magnetization  $M$  which vanishes in the region  $H < H_b$  but acquires finite values for  $H \geq H_b$ . Specifically, for  $H = H_b$  the magnetization can be calculated from

$$\mu_b = \lim_{N \rightarrow \infty} \frac{1}{(2N)^2} \sum_{\tau=-N}^N M_\tau. \quad (3.39)$$

The asymptotic expansion (3.38) cannot be employed here because equation (3.39) contains terms with values of  $\tau$  that are comparable to  $N$  and  $\mu_b$  can only be numerically calculated from equation (3.37). Yet, the actual sudden jump that occurs at the critical field can be calculated analytically from equation (3.37) by noting that the  $\tau = 0$  sector prevails above  $H_b$ , in the sense that it contains the unique absolute ground state for  $H > H_b$ . The last statement is corroborated by numerical diagonalization on short chains of varying size. Therefore the magnetization jump at the critical field is given by

$$\mu_0 = \frac{M_0}{2N} = \frac{1}{2} \sqrt{\Delta^2 - 1} \frac{I_{N-1}^0}{I_N^0} \quad (3.40)$$

where  $\mu_0$  is the average magnetization per site, and its thermodynamic limit  $\lim_{N \rightarrow \infty} \mu_0$  can be found from (3.38) to be

$$\mu_0 = \frac{1}{2} \sqrt{\frac{\Delta - 1}{\Delta + 1}}. \quad (3.41)$$

Analytical calculation of the magnetization for  $H > H_b$  is impossible at present because the  $\tau = 0$  ground state becomes increasingly complex away from the critical point. We have thus resorted to numerical diagonalization on short chains. Memory requirements restrict us to the range  $\Lambda \leq 14$  if we wish to compute all eigenstates. However we have been able to extend the

range to  $\Lambda \leq 24$  for the calculation of the ground-state energy via a Lanczos<sup>1</sup> algorithm [53, 54]. In all cases we provide explicit estimates of finite-size effects which suggest that the derived overall picture is indeed reliable.

For instance, the average magnetization per site  $\mu = M/\Lambda$  calculated on a cyclic chain with  $\Delta = 1.5$  and  $\Lambda = 10$  is depicted by a dashed line in figure 3.1 and exhibits a sudden jump at the critical field  $H_b = 1.11803399$  given by equation (3.13). The size of the jump was found equal to  $\mu = 0.24973268$ , also in perfect agreement with the analytical result (3.40) applied for  $\Delta = 1.5$  and  $N = \Lambda/2 = 5$ . Away from the critical point the magnetization increases smoothly to achieve the saturated ferromagnetic value  $\mu = 1/2$  in the limit  $H \rightarrow \infty$ .

Although  $H_b$  is independent of chain size, the magnetization does depend on  $\Lambda = 2N$  for  $H \geq H_b$ . A good estimate of its size dependence is obtained by taking advantage of the analytical result (3.41). Applied for  $\Delta = 1.5$  the above expression leads to  $\mu = 0.22360680$  which is overestimated by the value at  $\Lambda = 10$  quoted earlier by about 12%. More generally, the magnetization at the critical field computed on chains with  $\Lambda \sim 10$  does not differ from its  $\Lambda \rightarrow \infty$  limit by more than 13%, for all  $\Delta > 1$ , and the agreement improves at large  $\Delta$ . In chapter 5 we extrapolate the results from the Lanczos algorithm to the thermodynamic limit and we compare them with those obtained by other methods that are more appropriate for the study of the infinite system.

### 3.4 Surface spin-flop transition

The numerical calculation described in section 3.3 was subsequently repeated on an open chain with the same size  $\Lambda = 10$ , and the result is depicted by a solid line in figure 3.1. The magnetization is now seen to exhibit a sudden jump at a new critical field  $H_s = 0.60922570$  which is in excellent agreement with equation (3.20) applied for  $\Delta = 1.5$ . This result is consistent with the theoretical development of section 3.2 which predicts that the one-magnon surface mode becomes the ground state beyond  $H_s$ . One may then use the analytical results obtained on a semi-infinite chain to actually predict the magnetization, at least for some nontrivial field region above  $H_s$ .

---

<sup>1</sup>A source code for the Lanczos method can be downloaded freely from the Internet [52]

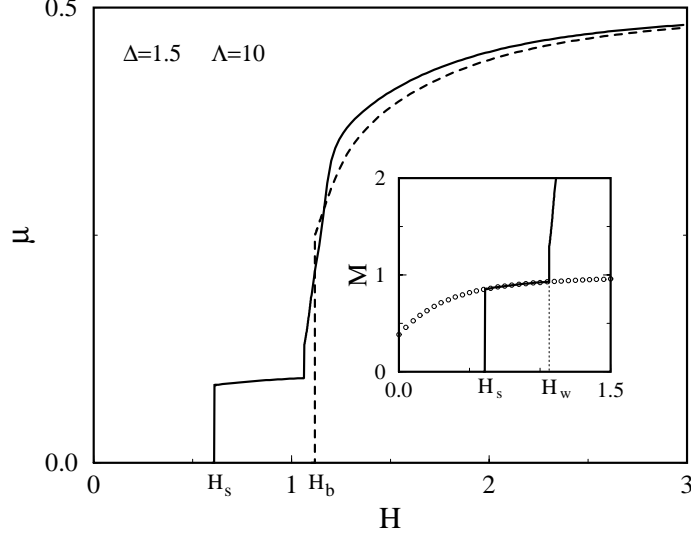


**Figure 3.1:** Field dependence of the average magnetization per site  $\mu = M/\Lambda$  in the ground state of a chain with  $\Delta = 1.5$  and  $\Lambda = 10$ . The dashed line corresponds to a cyclic chain and the solid line to an open chain with the same number of sites. The inset focuses on the first step of the main figure and compares the total magnetization  $M$  to the analytical prediction (3.45) depicted by open circles.

The ground-state total magnetization again vanishes for  $H < H_s$  but is equal to

$$M = \sum_{n=1}^{\Lambda} M_n, \quad M_n = (-1)^n \frac{\langle \psi_1 | T_n^z | \psi_1 \rangle}{\langle \psi_1 | \psi_1 \rangle}, \quad (3.42)$$

for  $H > H_s$  where  $|\psi_1\rangle$  is now the state of the surface mode in the lower gap of figure 2.14. Therefore the norm of this state is given by

$$\langle \psi_1 | \psi_1 \rangle = \sum_{n=1}^{\infty} (|A_n|^2 + |B_n|^2) = [1 + (\Delta - 2H - 2E_1)^2] \frac{\xi_1^2}{1 - \xi_1^2}, \quad (3.43)$$

where  $A_n$  and  $B_n$  are taken from equation (3.15) applied for  $\xi = \xi_1$  and  $E = E_1$  given by equation (3.17). Accordingly the local magnetization  $M_n$  is given by

$$M_{2n-1} = \frac{|A_n|^2}{\langle \psi_1 | \psi_1 \rangle} - \frac{1}{2}, \quad M_{2n} = \frac{1}{2} - \frac{|B_n|^2}{\langle \psi_1 | \psi_1 \rangle}, \quad (3.44)$$

for odd and even sites, respectively, and the total magnetization by

$$M = \frac{1 - (\Delta - 2H - 2E_1)^2}{1 + (\Delta - 2H - 2E_1)^2}. \quad (3.45)$$

It should be clear that the preceding results are valid also for  $H < H_s$  where the surface mode is not the ground state. In particular,

$$M(H = 0) = \frac{\Delta^2 - 1}{\Delta^2 + 1}, \quad (3.46)$$

is the total magnetization of the one-magnon surface state at vanishing field. At the critical field  $H_s$ , where  $E_1 = 0$ , equation (3.45) yields

$$M(H = H_s) = \frac{1 - (\Delta - 2H_s)^2}{1 + (\Delta - 2H_s)^2}, \quad (3.47)$$

which agrees with the jump observed at  $H_s$  in figure 3.1 to eight significant figures; as expected on the basis of our discussion of the size dependence of the surface modes in section 3.2.

Such an excellent agreement of the analytical prediction (3.45) with the finite-size results of figure 3.1 persists over a nontrivial field region  $H_s < H < H_w$ , as demonstrated in the inset which focuses on the first step of the main figure. Clearly a new transition takes place at  $H_w$  and the one-magnon surface mode ceases to be the ground state for  $H > H_w$ . One would think that the SSF transition proceeds beyond  $H_s$  by a cascade of level crossings induced by multimagnon surface modes. But the results of figure 3.1 clearly indicate that there exists only one additional crossing at the critical field  $H_w \approx 1.06 < H_b$  for  $\Delta = 1.5$ .

In order to appreciate the precise nature of the transition at  $H_w$  we have examined the evolution of the *local* magnetization  $M_n$  with increasing bias field. Results for  $\Delta = 1.5$  and  $\Lambda = 10$  are shown in figure 3.2 for a selected set of field values, using a more or less obvious notation. For definiteness we begin with the first Néel state  $|N_A\rangle$  of equation (3.2) whose local magnetization is depicted in the  $H = 0$  entry of figure 3.2. The Néel state persists as the absolute ground state until the field crosses the critical value  $H_s = 0.609$  of equation (3.20). Just above  $H_s$  a surface magnon is realized in the ground state, as shown in the  $H = 0.61$  entry which may be reproduced to great precision using the analytical prediction (3.44) obtained on a semi-infinite chain. With further increase of the applied field the surface magnon slowly approaches a boundary Ising domain wall of the type *uududu* . . . However a sudden change occurs at the critical field  $H_w \approx 1.06$ , as demonstrated in the  $H = 1.07$  entry where a bulk domain wall appears at the center of the

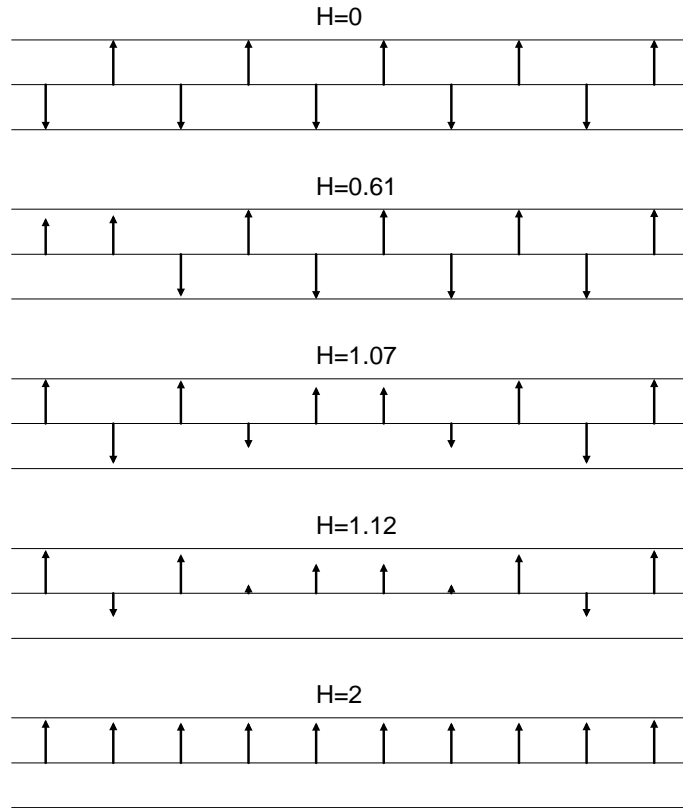


**Figure 3.2:** Snapshots of the local magnetization  $M_n$  on a chain with  $\Delta = 1.5$  and  $\Lambda = 10$ , for a characteristic set of field values described in the text.

chain. This state is a slightly depleted version of an ideal Ising domain wall of the type  $\dots uduudu \dots$ , thanks in part to the finite value of  $\Delta$  and to the applied field. The tendency for inflation of the domain wall with increasing field becomes apparent in the  $H = 1.12$  entry, where the field was chosen to be slightly greater than the bulk critical value  $H_b = 1.118$  of equation (3.13). It should be noted here that the anticipated BSF transition is replaced on an open chain by a rapid but rounded crossover which becomes increasingly sharp with increasing chain size. The inflation of the domain wall is more rampant at higher field values and the local magnetization approaches a nearly uniform ferromagnetic configuration within the bulk, with some nonuniformity persisting near the edges of the open chain; as is completely apparent in the last,  $H = 2$ , entry of figure 3.2. However complete ferromagnetic order is achieved only when  $H \rightarrow \infty$ .

The picture was completed with a detailed examination of the pertinent level crossings. Thus we calculated the ground-state energies of all sectors ( $\tau = N, N - 1, \dots, -N$ ) as functions of the applied field  $H$  at the given anisotropy  $\Delta = 1.5$ . The first transition occurs at the critical field  $H_s$  where the Néel state  $|N_A\rangle$ , with  $\tau = N$ , is crossed by the one-magnon surface mode, with  $\tau = N - 1$ . For higher fields, multiple level crossings take place among the lowest-energy states of the multimagnon sectors  $\tau = N - 2, N - 3, \dots$ , and are likely to play an important role in the low-temperature dynamics. But most of these crossings are irrelevant for the determination of the absolute ground state because the one-magnon surface mode is eventually overtaken only by the ground state of the  $\tau = 0$  sector which is an antiferromagnetic domain wall located at the center of the open chain.

The last remark prompted us to examine the local magnetization in the lowest-energy states of all sectors, even though most of these states do not become the absolute ground state for any field value. The result for  $\Lambda = 2N = 10$  is presented in table 3.1 using a symbolic notation that is strictly appropriate only in the extreme Ising limit  $\Delta \rightarrow \infty$ . But the essence of the derived picture at finite  $\Delta$  and  $0 < H \lesssim H_b$  is well represented in table 3.1. Thus the ground state in each sector ranges between the two pure Néel states of equation (3.2) which correspond to the two extreme values of the azimuthal pseudospin  $\tau = \pm N$ . For intermediate values of  $\tau = N - \lambda$ , with  $\lambda = 1, 2, \dots, 2N - 1$ , a domain wall is formed at a distance equal to  $\lambda$  lattice

### 3.4. Surface spin-flop transition

$\tau$	Pseudospin	Spin	$M$
5	<i>uuuuuuuuuu</i>	<i>dududududu</i>	0
4	<i>duuuuuuuuu</i>	<i>ududududu</i>	1
3	<i>dduuuuuuuu</i>	<i>uddudududu</i>	0
2	<i>ddd uuuuuuuu</i>	<i>ud u u d u d u d u</i>	1
1	<i>dddduuuuuu</i>	<i>ud u d d u d u d u</i>	0
0	<i>ddddduuuuu</i>	<i>u d u d u d u d u</i>	1
-1	<i>dddddduuuu</i>	<i>u d u d u d d u d u</i>	0
-2	<i>ddddddd uuu</i>	<i>u d u d u d u d u</i>	1
-3	<i>ddddddd duu</i>	<i>u d u d u d u d d u</i>	0
-4	<i>ddddddd du</i>	<i>u d u d u d u d u u</i>	1
-5	<i>ddddddd d</i>	<i>u d u d u d u d u d</i>	0

**Table 3.1:** Symbolic illustration of the ground state in each sector on an open chain with  $\Lambda = 10$ .

units from the left boundary of the chain. Therefore the good quantum number  $\tau$  provides a rigorous definition of the relative location of a domain wall on an open chain, even at finite  $\Delta$  where the wall expands and thus departs from its ideal Ising shape. Domain walls with opposite pseudospin  $\pm\tau$  are displayed symmetrically about the center and carry the same energy. The least-energy state for  $H > H_w$  is a  $\tau = 0$  domain wall located at the center of the chain.

To rule out the possibility of an accident that might have occurred for the specific size  $\Lambda = 10$  used so far, we repeated the calculation for  $\Lambda = 12$  and the results for the total magnetization are shown in figure 3.3. Surprisingly, two instead of one additional level crossings may now be discerned; the first at  $H_w \approx 1.06$ , which is virtually identical to the value obtained earlier for  $\Lambda = 10$ , and the second at  $H'_w \approx 1.09$  which indicates the existence of yet another critical field. This interesting twist in the general picture is clarified by the results of the local magnetization  $M_n$  given in figure 3.4, in conjunction with an obvious extension of table 3.1 to  $\Lambda = 12$ . At this point it is useful to address the last column of table 3.1 which quotes the possible values of the total magnetization of domain walls in the extreme Ising limit;  $M = 0$  or 1. One may say that the two values correspond to domain walls of *dd*

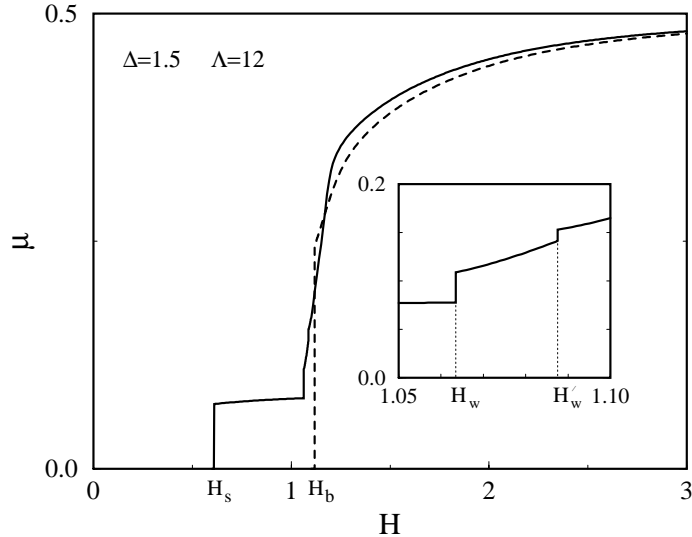


**Figure 3.3:** Same as figure 3.1 for a chain with  $\Lambda = 12$ . The inset now focuses on a narrow region near the critical field  $H_w$  to reveal the existence of a secondary critical field  $H'_w$ .

or  $uu$  type, respectively. Although these values are significantly modified at finite  $\Delta$ , they nevertheless suggest that a level crossing is more likely to be induced by a  $uu$  state whose (negative) Zeeman energy in a (positive) field  $H$  is greater in absolute value, similarly to the case of the classical system discussed in chapter 2. The  $\tau = 0$  domain wall at the center of the  $\Lambda = 10$  chain is indeed a  $uu$  state. However, when table 3.1 is extended to  $\Lambda = 2N = 12$ , where  $N = 6$  is even, the  $\tau = 0$  domain wall becomes a  $dd$  state, whereas  $uu$  domain walls that are closest to the center are those with  $\tau = \pm 1$  and are likely to be energetically favorable.

Simple comparison of the  $H = 1.07$  entries in figures 3.2 and 3.4 reveals that the same domain wall of the  $uu$  type appears in both cases, but the wall in the second case is displaced by one lattice unit from the center of the chain. Since a bulk domain wall is rather narrow for the specific anisotropy  $\Delta = 1.5$  used so far, its energy is relatively insensitive to the precise location about the center even for short chains. This explains why the transition observed for  $\Lambda = 12$  occurs at virtually the same critical field  $H_w \approx 1.06$  found earlier for  $\Lambda = 10$ , even though it now corresponds to a level crossing of the one-magnon mode by the ground state of the  $\tau = 1$  sector. However the  $\tau = 0$  ground state, which originates in a  $dd$  domain wall at lower fields,

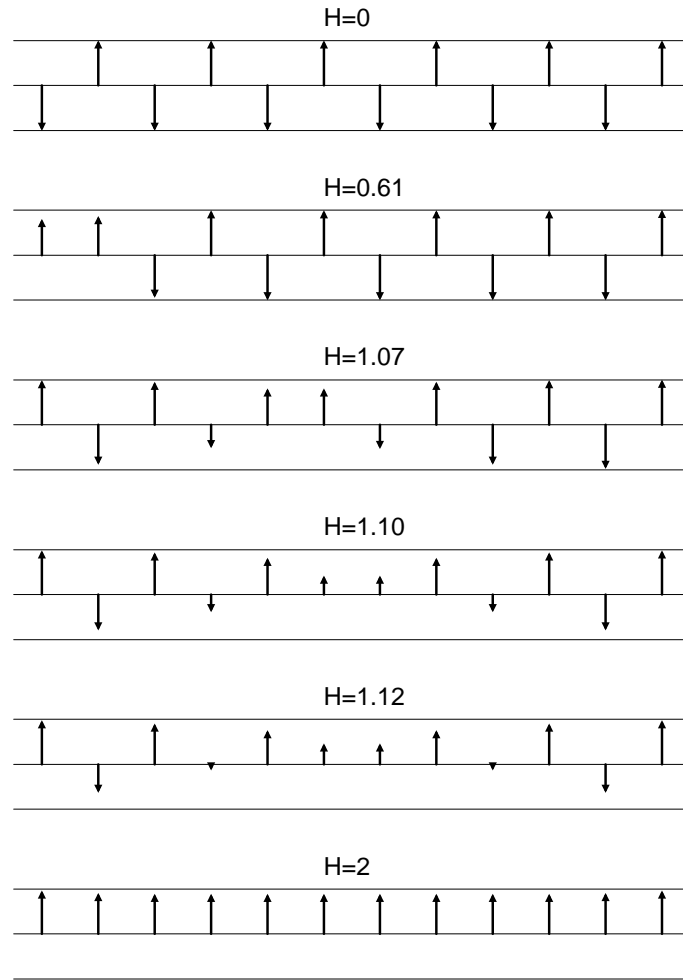


**Figure 3.4:** Snapshots of the local magnetization  $M_n$  on a chain with  $\Delta = 1.5$  and  $\Lambda = 12$ , for a characteristic set of field values described in the text.

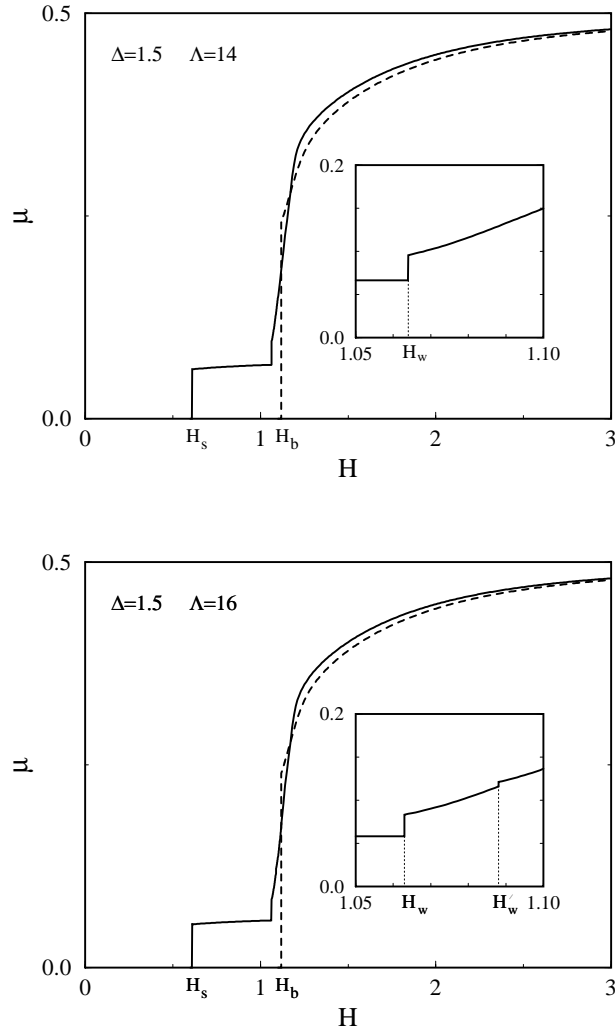


**Figure 3.5:** The results of figures 3.1, 3.3 now iterated on longer chains with  $\Lambda = 14$  and  $16$  to establish the alternating pattern described in the text.

ultimately becomes sufficiently frustrated to overtake the  $\tau = 1$  sector at a new critical field  $H'_w \approx 1.09$ ; as demonstrated by the  $H = 1.10$  entry of figure 3.4. The absolute ground state remains in the  $\tau = 0$  sector for  $H > H'_w$  and is again rendered increasingly ferromagnetic in the limit  $H \rightarrow \infty$ .

The foregoing analysis suggests that a transition into a domain-wall state is always present on an open chain at a critical field  $H_w$ , and is merely decorated by a secondary transition at a slightly higher field  $H'_w$  when  $N$  in  $\Lambda = 2N$  is even. This alternating pattern is confirmed by the calculated total moment for  $\Lambda = 14$  and  $16$  shown in figure 3.5, and by further analysis

of level crossings using the Lanczos algorithm on chains with  $\Lambda \leq 22$ . The main new critical field  $H_w$  quickly stabilizes to the size-independent value  $H_w = 1.0625$ , for  $\Delta = 1.5$ , which is distinct from the bulk critical field  $H_b = 1.118$  and thus clearly suggests the appearance of a definite domain-wall phase in  $H_w < H < H_b$ .

The picture just derived for the specific anisotropy  $\Delta = 1.5$  is more or less sustained for a wide range of anisotropies in the region  $\Delta \gtrsim 1.25$ . However this simple picture becomes more involved as the anisotropy approaches the isotropic limit  $\Delta \rightarrow 1^+$ . Already at  $\Delta = 1.125$  a cascade of level crossings are induced by the least-energy states of the sectors  $\tau = N-1, N-3, N-5, \dots$  at a sequence of critical fields  $H_s, H_w, H'_w, \dots$  which stabilize to size-independent values. The main SSF transition is still given by the crossing of the  $\tau = N$  Néel state by the  $\tau = N-1$  surface magnon or boundary domain wall at the critical field  $H_s$  of equation (3.20). However the next transition at  $H_w$  now corresponds to a crossing of the  $\tau = N-1$  surface magnon by the  $\tau = N-3$  ground state which is a  $uu$ -type domain wall located three lattice units away from the left end of the chain. Subsequent transitions at a sequence of critical fields  $H'_w, H''_w, \dots$  correspond to a sequence of hoppings of the domain wall in steps of two lattice units until it arrives at the center of the chain. Once the domain wall reaches the center, its future evolution is similar to the one described earlier for  $\Delta = 1.5$ .

So far we have described the SSF transition through a series of level crossings from the  $\tau = N$  to the  $\tau = 0$  sector. We could equivalently start from the second of the polarized Néel states (3.2), with  $\tau = -N$ , which would give its place to the  $-N+1$  surface state at  $H = H_s$  and finally lead to the  $\tau = 0$  sector through a  $\tau \rightarrow -\tau$  symmetrical series of crossings. An inspection of table 3.1 shows that this procedure corresponds to a surface transition at the other end of the chain and in fact both mechanisms of the SSF transition take place simultaneously in our numerical simulations.

A completely satisfactory description of the SSF transition is not possible on the short chains used in our numerical calculations, because the size of the relevant domain walls increases to lattice dimensions in the limit  $\Delta \rightarrow 1^+$ . However the observed pattern is sufficiently clear to provide unambiguous numerical evidence for the new critical field  $H = H_w(\Delta)$ .

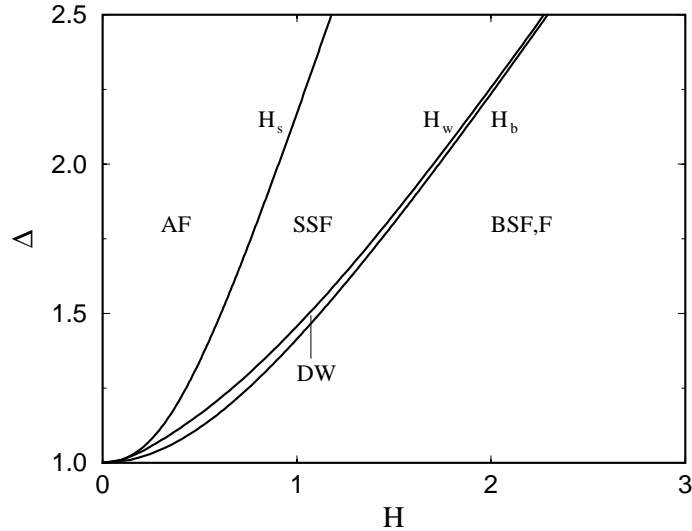


**Figure 3.6:** The  $T = 0$  phase diagram for the quantum model (3.1). The bulk and surface critical boundaries  $H_b$  and  $H_s$  are given analytically by equations (3.13) and (3.20), and the domain-wall boundary  $H_w$  was obtained numerically as described in section 3.2.

### 3.5 The phase diagram

In figure 3.6 we show the  $T = 0$  phase diagram of the quantum system. For  $H < H_s$  the ground state is purely Néel and the corresponding phase is labeled as antiferromagnetic (AF). The region  $H_s < H < H_w$  is characterized by a ground state which is a surface mode and is thus called a surface spin-flop (SSF) phase. The domain-wall (DW) phase extends in the region  $H_w < H < H_b$  where a bulk domain wall is realized in the ground state. Finally the region  $H > H_b$  corresponds to the bulk spin-flop (BSF) phase, studied in section 3.3, which becomes increasingly ferromagnetic (F) although no transition to the pure F state occurs at any finite field  $H$ . This explains the composite designation (BSF,F) in figure 3.6. Although this basic phase diagram does not reflect the fine structure in  $H_w < H < H_b$  alluded to in section 3.4 it certainly contains all those elements that are likely to be important in practical applications. One should add that the phase diagram for this quantum spin- $\frac{1}{2}$  chain is simpler than the classical phase diagram of figure 2.15.

We conclude with a comment on the thermodynamic limit. Bulk quantities such as the average magnetization per site  $\mu = M/\Lambda$  become relatively

insignificant in the limit  $\Lambda \rightarrow \infty$  within the SSF and BSF phases. For example, for  $H_s \leq H \leq H_w$ , the total magnetization  $M$  is given analytically by equation (3.45) and is of order unity. Therefore the average moment  $\mu$  in the SSF phase decreases linearly with  $1/\Lambda$ , a fact that is progressively apparent in figures 3.1, 3.3 and 3.5, and in the thermodynamic limit the union of the AF, SSF and DW phases becomes an extended AF phase. Nevertheless surface effects are always present on open even chains of any size and could be observed in a magnetic material that is sufficiently doped to produce a statistically significant number of such chains.

### 3.6 The odd chain

Similarly to the classical system of chapter 2 the odd system differs from the even one without introducing anything fundamentally new. The two Néel states

$$\begin{aligned} |N_A\rangle &= |d, u, d, u, \dots, d, u, d\rangle, \\ |N_B\rangle &= |u, d, u, d, \dots, u, d, u\rangle, \end{aligned} \tag{3.48}$$

are again mapped by equation (3.3) to two completely polarized ‘ferromagnetic’ states which are exact eigenstates of the Hamiltonian (3.4) for any value of the applied field. However degeneracy is now lifted by the bias field because the states (3.48) carry nonvanishing total magnetization  $M = \mp 1/2$  and the corresponding energy eigenvalues are given by  $\pm H/2$ . Therefore, when  $H$  is taken to be positive,  $|N_B\rangle$  is the unique ground state with  $M = 1/2$ . Similarly, when  $H$  is negative, the unique ground state is  $|N_A\rangle$  with  $M = -1/2$ . For definiteness, we assume that the bias field is positive, the case of  $H$  being completely analogous.

Our task is then to determine the critical field above which a spin-flop transition may take place. Examination of the one-magnon spectrum around the state  $|N_B\rangle$  leads to a picture that is fairly similar to that of figure 2.14, with the following notable difference. The gap mode 1 is now missing from the spectrum, while mode 1' is duplicated. As a result there will be no SSF transition at the critical field  $H_s$ . Instead an odd open chain will proceed directly to a BSF transition which occurs by a cascade of successive level crossings in the vicinity of the critical field  $H_b$ . This picture is similar but not

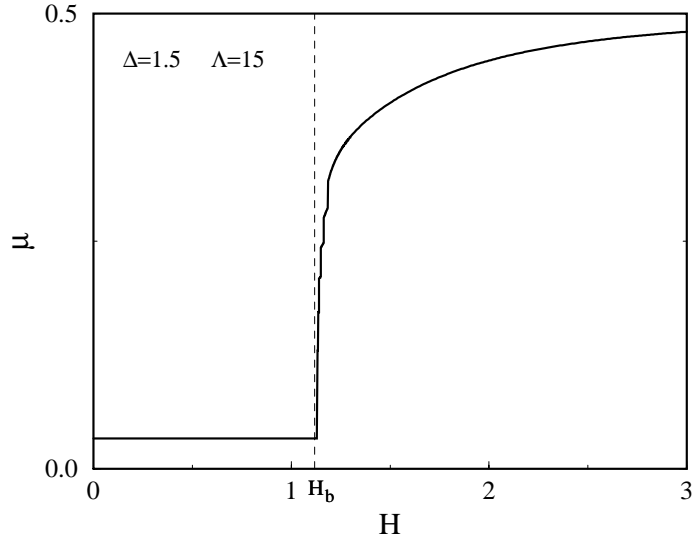


**Figure 3.7:** Field dependence of the average magnetization per site  $\mu = M/\Lambda$  in the ground state with  $\Delta = 1.5$  on an open chain with an odd number of sites  $\Lambda = 15$ .

identical to the BSF transition on an even cyclic chain, studied in section 3.3, where all crossings take place at precisely the same critical field  $H_b$ . Putting it differently, if a hidden symmetry were indeed present on an even cyclic chain at the critical point, it would be broken on an open chain.

The lack of a SSF transition on an odd chain becomes apparent with an explicit calculation of the total magnetization for  $\Delta = 1.5$  and  $\Lambda = 15$  shown in figure 3.7. At low field values the total magnetization is given by  $M = 1/2$ , or  $\mu = 1/2\Lambda$ , and coincides with that of the pure Néel state  $|N_B\rangle$ . The BSF transition near the critical field  $H_b$  is also apparent in figure 3.7, whereas the chain is set on a more or less smooth course toward ferromagnetic order for  $H > H_b$ .

### 3.7 The general XYZ model

There have been known [55] spin- $\frac{1}{2}$  antiferromagnets throughout a wide range of parameters satisfying inequalities (2.1). While a direct approach to all these models has not yet been possible, we present some preliminary results for some interesting limiting cases of the general XYZ model.

For example, an interesting special case is the anisotropic XY model ( $J_1 =$

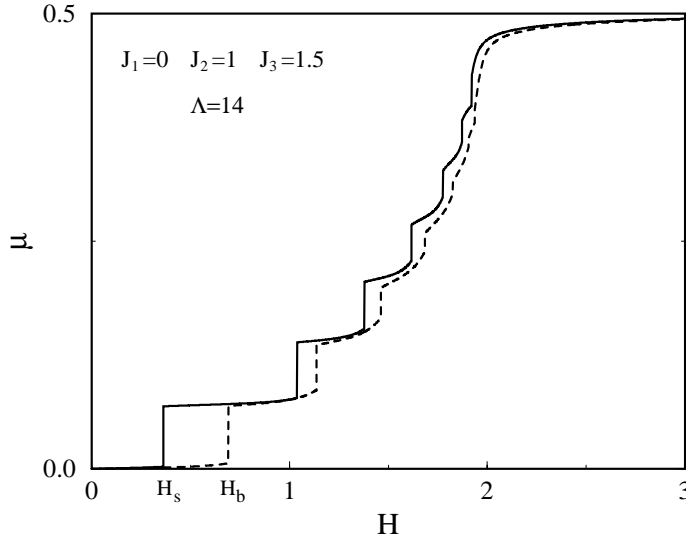


**Figure 3.8:** Field dependence of the average magnetization per site  $\mu = M/\Lambda$  in the ground state of a model with  $J_1 = 0$ ,  $J_2 = 1$ ,  $J_3 = 1.5$ , and  $\Lambda = 14$ . The dashed line corresponds to a cyclic chain and the solid line to an open chain with the same number of sites.

0,  $J_2 = 1$ ,  $J_3 = \Delta > 1$ ), or YZ model in current notation, in the presence of an in-plane field applied along the easy axis. Analytical solution of this model does not seem possible at nonvanishing field, and theoretical analysis is further complicated by the lack of a  $U(1)$  symmetry. A numerical calculation of the ground-state total magnetization on a chain with  $\Lambda = 14$  is shown in figure 3.8. While a trace of both a surface ( $H_s$ ) and a bulk ( $H_b$ ) critical field is again present, the spin-flop transition obviously proceeds by multiple level crossings which are difficult to study in detail by numerical simulations on short chains. A notable feature of figure 3.8 is that ferromagnetic order at high fields is now more robust.

The picture could again simplify in the XXZ model ( $J_1 = 1 = J_2$ ,  $J_3 = \Delta > 1$ ) where a  $U(1)$  symmetry is restored. The effect of a uniform field pointing along the symmetry axis is simply a linear Zeeman shift of the zero-field energy eigenvalues. The latter may, in principle, be obtained by the Bethe Ansatz [12] known to apply to both a cyclic and an open chain, [40] and the problem of spin-flop transitions amounts to studying the density of level crossings induced by the linear Zeeman shift. In fact, the  $T = 0$  phase diagram on an infinite chain was studied by Johnson and McCoy [56] and consists of an AF phase for  $H < H_b$ , a BSF phase for  $H_b < H < H_f$ , and a

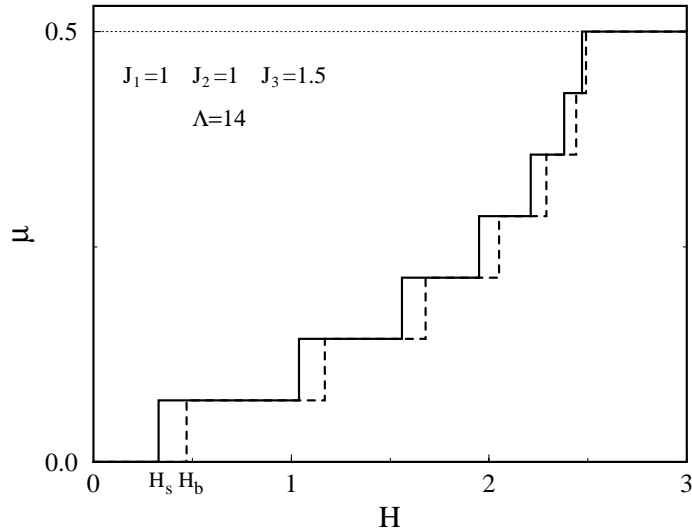


**Figure 3.9:** Field dependence of the average magnetization per site  $\mu = M/\Lambda$  in the ground state of the XXZ model  $J_1 = 1$ ,  $J_2 = 1$ ,  $J_3 = 1.5$  with  $\Lambda = 14$ . The dashed line corresponds to a cyclic chain and the solid line to an open chain with the same number of sites. Note the transition to a pure F phase above the critical field  $H_f = 2.5$ .

pure F phase for  $H > H_f$ . If we set  $\Delta \equiv \cosh \Phi$  the critical field  $H_b$  is given by [49]

$$H_b = \sinh \Phi \sum_{n=-\infty}^{\infty} \frac{(-1)^n}{\cosh n\Phi} = \sinh \Phi \frac{\pi}{\Phi} \sum_{n=-\infty}^{\infty} \frac{1}{\cosh \left[ \frac{(2n+1)\pi^2}{2\Phi} \right]}, \quad (3.49)$$

which differs significantly from equation (3.13) especially at weak anisotropies ( $\Delta \rightarrow 1^+$  or  $\Phi \rightarrow 0$ ) where the field (3.49) vanishes exponentially. Furthermore a transition to a pure F state now takes place above the critical field

$$H_f = \Delta + 1. \quad (3.50)$$

Comparison of the results for the total magnetization computed numerically on an open and a cyclic chain with  $\Lambda = 14$ , shown in figure 3.9, again suggests a SSF transition at a new critical field  $H_s < H_b$ . However both  $H_b$  and  $H_s$  are now size-dependent and hence the results of figure 3.9 are not sufficient to establish the existence of a SSF transition. Extrapolation of the relevant magnon gaps calculated on chains with  $\Lambda \leq 22$  indicates a ratio  $H_b/H_s$  that remains remarkably close to its Ising value 2 for a wide range of strong anisotropies in the region  $\Delta > 2$ . Nevertheless extrapolation

becomes problematic at weak anisotropies and thus a definite prediction near the isotropic limit is difficult to obtain numerically. It should be mentioned that a considerable amount of work has been devoted to the study of the XXZ model in the presence of boundary fields, [37, 38] but the more direct questions raised here in the presence of a uniform bulk field do not seem to have been addressed.

### 3.8 Conclusion

The main advantage of the bulk and surface spin-flop transitions studied in this chapter is that they are induced by a *uniform* bias field which can be easily applied and tuned to any desired value. This situation should be contrasted with the case of *boundary* fields [36] that are generally difficult to implement, especially in doped materials where open magnetic chains are produced within the crystal in a random manner.

Suppose that a quasi-one-dimensional magnetic material is found [55] with exchange constants that are approximately given by equation (3.1) after suitable normalization. Doping such a material with nonmagnetic ions [57] would produce open magnetic chains of varying size. However, since the critical boundaries of figure 3.6 are practically independent of chain size, it would be possible to tune the applied field to the various regions of the phase diagram and thus probe the predicted magnetic phases. Electron-spin resonance at low temperature seems to be an appropriate experimental tool, and is theoretically discussed in chapter 4.

We conclude with a comment on the classical limit of our model. The analytical result (3.41) coincides with the magnetization obtained within the classical calculation of chapter 2 at the onset of the BSF phase which is described by a canted spin configuration. This curious fact could be investigated further by generalizing the special states (3.32) to arbitrary spin  $s$ , also in analogy with a similar calculation in the model of reference 36. One should then be able to explicitly study the classical (large- $s$ ) limit on any finite chain and eventually explain its coincidence with the quantum prediction (3.41) in the thermodynamic limit. As we have seen in chapter 2 the classical ground state is independent of  $J_1$  and thus combines features of the entire class of quantum models in the range  $|J_1| \leq J_2 < J_3$ .



## CHAPTER 4

# MAGNETIC RESONANCE

### 4.1 Introduction

In this chapter we present a theoretical study of electron-spin resonance (ESR) in a system described by the Hamiltonian (3.1). In a typical ESR experiment a homogeneous microwave field of frequency  $\omega$  is applied to the magnetic system and its absorption spectrum is measured in order to probe the susceptibility and elementary excitations.

When an AC magnetic field of the form

$$\mathbf{h} = h_0 \cos \omega t \mathbf{e} \quad (4.1)$$

is applied to a magnetic system, in addition to the bias field  $\mathbf{H}$ , it induces transitions between its eigenstates. The resulting average power absorption is equal to [58]

$$\bar{P}(\omega) = \hbar\omega \sum_{E_a > E_b} D_{ab} [p(E_a) - p(E_b)] \quad (4.2)$$

where  $D_{ab}$  is the quantum-mechanical probability that a transition takes place between an initial state  $|a\rangle$  and a final state  $|b\rangle$ , and  $p(E)$  is the Boltzmann probability that a state of energy  $E$  is occupied given by

$$p(E) = \frac{e^{-E/kT}}{\sum_{E'} e^{-E'/kT}}. \quad (4.3)$$

Sufficiently weak fields  $\mathbf{h}$  can be considered to be a perturbation to the Hamiltonian (3.4) of the form

$$W_{pert} = -M^e h_0 \cos \omega t \quad (4.4)$$

where  $M^e = \mathbf{M} \cdot \mathbf{e}$  is the projection of the magnetization  $\mathbf{M}$  along the direction of the AC field. Then, time dependent perturbation theory predicts

$$D_{ab} = \frac{2\pi h_0^2}{\hbar} |\langle a|M^e|b\rangle|^2 \delta(E_a - E_b - \hbar\omega), \quad (4.5)$$

where  $|\langle a|M^e|b\rangle|^2$  will be referred to as the transition amplitude. The average power absorption then reads

$$\bar{P} = \frac{h_0^2}{2} \pi\omega \sum_{E_a > E_b} [p(E_a) - p(E_b)] |\langle a|M^e|b\rangle|^2 \delta(E_a - E_b - \hbar\omega). \quad (4.6)$$

From equation (4.6) it is possible to derive the imaginary part of the susceptibility which is related to  $\bar{P}$  by

$$\bar{P} = \frac{\omega}{2} \chi'' h_0^2 \quad (4.7)$$

while the real part of the susceptibility can be found from the Kramers-Kronig equations.

In the case of our model (3.1) operators  $M^x$  and  $M^y$  can be rewritten with respect to the pseudospin variables (3.3) as

$$\begin{aligned} M^x &= \sum_{n=1}^{\Lambda} T_n^x = \sum_{n=1}^{\Lambda} \frac{T_n^+ + T_n^-}{2}, \\ M^y &= \sum_{n=1}^{\Lambda} (-1)^n T_n^y = \sum_{n=1}^{\Lambda} (-1)^n \frac{T_n^+ - T_n^-}{2i}. \end{aligned} \quad (4.8)$$

Therefore, if the field  $\mathbf{h}$  is applied in either the  $x$  or  $y$  direction a transition between states  $|a\rangle$  and  $|b\rangle$  is only possible if

$$\tau_a = \tau_b \pm 1 \quad (4.9)$$

where  $\tau_a$  and  $\tau_b$  are the eigenvalues of  $T^z$  corresponding to the  $|a\rangle$  and  $|b\rangle$  states respectively.

Our task in this chapter will be to calculate the low-temperature absorption intensity along the  $x$  and the  $y$  direction defined as

$$I^{x,y}(\omega_{ab}) = \omega_{ab} \sum_{E_a > E_b} [p(E_a) - p(E_b)] |\langle a|M^{x,y}|b\rangle|^2 \quad (4.10)$$

where  $\omega_{ab} = E_a - E_b$ . For the calculation of the eigenstates and the relevant matrix elements we use analytical results of chapter 3 or numerical diagonalization on sort chains. The intensity spectrum of the closed chain is studied in section 4.2 in order to probe the BSF transition while in section 4.3 we present the corresponding calculation on an open chain. Finally, our main conclusions are summarized in section 4.4.

## 4.2 Bulk spin-flop transition

In order to calculate the absorption intensity spectrum  $I(\omega)$  of the bulk system we consider a closed chain with  $\Lambda = 2N$  sites. As we have seen in chapter 3 for fields in the region of  $0 \leq H < H_b$  the energy spectrum presents non vanishing energy gap. For sufficiently low temperatures  $T$  only the two fully polarized ground states  $|F_A\rangle$ ,  $|F_B\rangle$  with  $\tau = N$  and  $\tau = -N$  and vanishing energy are occupied with

$$p(0) \simeq 1/2. \quad (4.11)$$

Then from equations (4.9) and (4.11) we can see that non zero contributions to the intensity spectrum will be due to transitions from  $|F_A\rangle$  to the one-magnon sector with  $\tau = N - 1$  and from  $|F_B\rangle$  to the sector with  $\tau = -N + 1$ .

Because of the  $\tau \leftrightarrow -\tau$  symmetry the contribution of these two sets of transitions will be equal therefore it is sufficient to study only the former. In the rest of this chapter we use this symmetry argument to restrict to transitions between the sectors with  $\tau = 0, 1, \dots, N$ . We then scale the resulting absorption intensity by two in order to account for transitions to negative  $\tau$ . States of negative  $\tau$  are only considered for the proper calculation of  $p(E)$ .

We now use the analytical results of section 3.2 for the  $\tau = N - 1$  eigenstates  $|\psi\rangle$  to calculate the relevant matrix elements  $\langle F_A | M^{x,y} | \psi \rangle$ . One can easily check that for  $0 \leq H < H_b$  all the matrix elements are equal to zero except for those involving one-magnon states  $|A\rangle$  and  $|B\rangle$  characterized by the quantum numbers  $\tau = N - 1$ ,  $\mathbf{k} = 0$ , and corresponding energies  $E_{A,B} = \Delta \mp \sqrt{H^2 + 1}$ . Therefore at low temperatures the only possible transitions are between  $|F_A\rangle$  and the states  $|A\rangle$  and  $|B\rangle$  contributing to the absorption intensity  $I^{x,y}(\omega)$  at frequencies

$$\omega_A = \Delta - \sqrt{H^2 + 1}, \quad \omega_B = \Delta + \sqrt{H^2 + 1}. \quad (4.12)$$

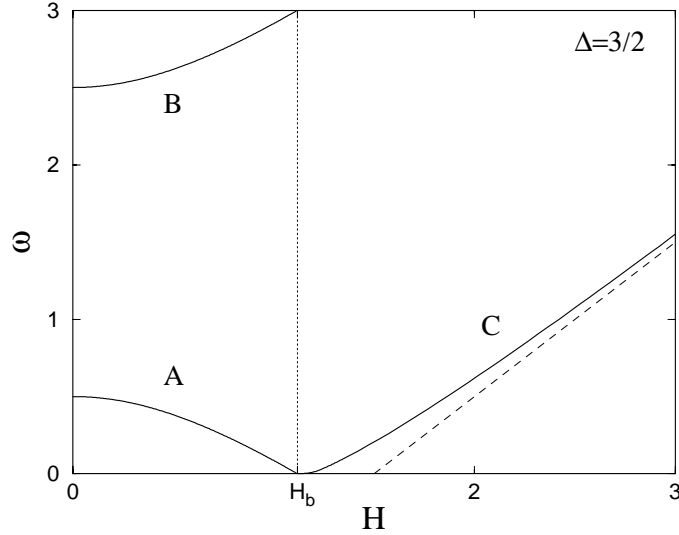


**Figure 4.1:** Field dependence of the resonance lines of the bulk system for  $\Delta = 3/2$ . The A and C lines actually designate the energy gap of the closed chain in the thermodynamic limit while the skew dashed line represents the Ising asymptote  $H - \Delta$ .

For the special case of  $\Delta = 3/2$   $\omega_A$  and  $\omega_B$  are displayed in figure 4.1 by lines A and B respectively.

The resulting transition amplitudes are found to be

$$\frac{|\langle F_A | M^x | A \rangle|^2}{\langle F_A | A \rangle} = \frac{|\langle F_A | M^y | B \rangle|^2}{\langle F_A | B \rangle} = \frac{\Lambda (1 + Y)^2}{8 (1 + Y^2)} \quad (4.13)$$

$$\frac{|\langle F_A | M^y | A \rangle|^2}{\langle F_A | A \rangle} = \frac{|\langle F_A | M^x | B \rangle|^2}{\langle F_A | B \rangle} = \frac{\Lambda (1 - Y)^2}{8 (1 + Y^2)}$$

where  $Y = 1/(H + \sqrt{H^2 + 1})$ . Combining equations (4.10), (4.11) and (4.13) we find the absorption intensities per site  $I_A^{x,y} = I^{x,y}(\omega_A)/\Lambda$  and  $I_B^{x,y} = I^{x,y}(\omega_B)/\Lambda$  to be

$$I_A^x = \frac{\omega_A (1 + Y)^2}{8 (1 + Y^2)}, \quad I_A^y = \frac{\omega_A (1 - Y)^2}{8 (1 + Y^2)} \quad (4.14)$$

$$I_B^x = \frac{\omega_B (1 - Y)^2}{8 (1 + Y^2)}, \quad I_B^y = \frac{\omega_B (1 + Y)^2}{8 (1 + Y^2)}$$

where we have included a factor of two due to the negative  $\tau$  transitions as discussed above. The calculated intensities per site for anisotropy  $\Delta = 3/2$  are shown in figure 4.2.

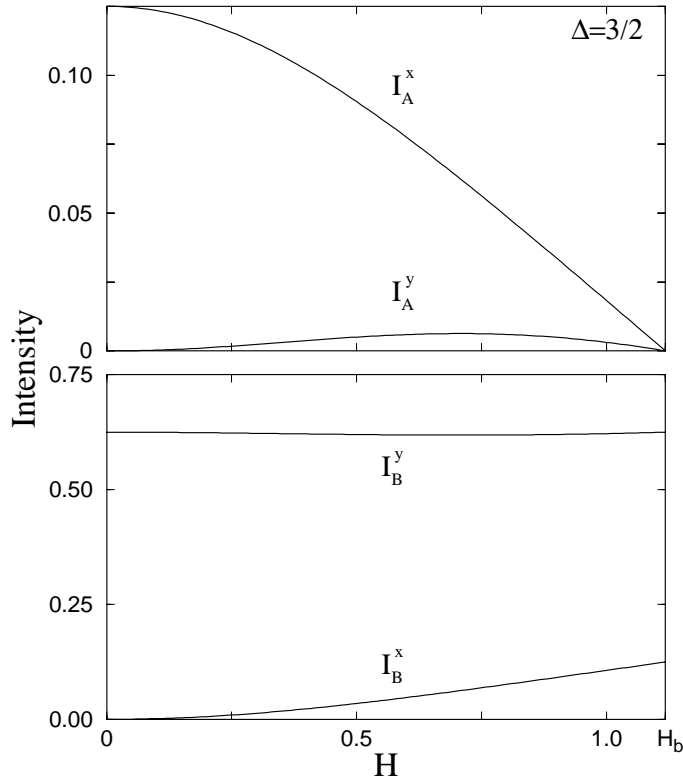


**Figure 4.2:** The absorption intensities per site  $I_A$  and  $I_B$  of the bulk resonance lines A and B for  $H < H_b$ .

For  $H > H_b$  the ground state is the lowest energy state of the  $\tau = 0$  sector  $|\psi_0\rangle$ . Direct numerical diagonalization on short chains ( $\Lambda \leq 14$ ) shows that the first excited states of the system are the lowest lying states of the  $\tau = \pm 1$  sectors  $|\psi_{\pm 1}\rangle$  which is verified by Lanczos diagonalization on chains up to  $\Lambda = 24$  sites. At low temperatures only the ground state is occupied with  $p(E) \simeq 1$  and the absorption intensity spectrum is due to transitions from  $|\psi_0\rangle$  to states of the  $\tau = \pm 1$  sectors. Here again we study transitions to the  $\tau = 1$  sector only.

The numerical calculation of the relevant matrix elements of both  $M^x$  and  $M^y$  shows that the only significant contribution to the absorption intensity is caused by transitions from the  $|\psi_0\rangle$  to the  $|\psi_1\rangle$  states, resulting in a unique resonance line in the spectrum of the absorption intensity at frequency

$$\omega_C = E_{\psi_1} - E_{\psi_0}, \quad (4.15)$$

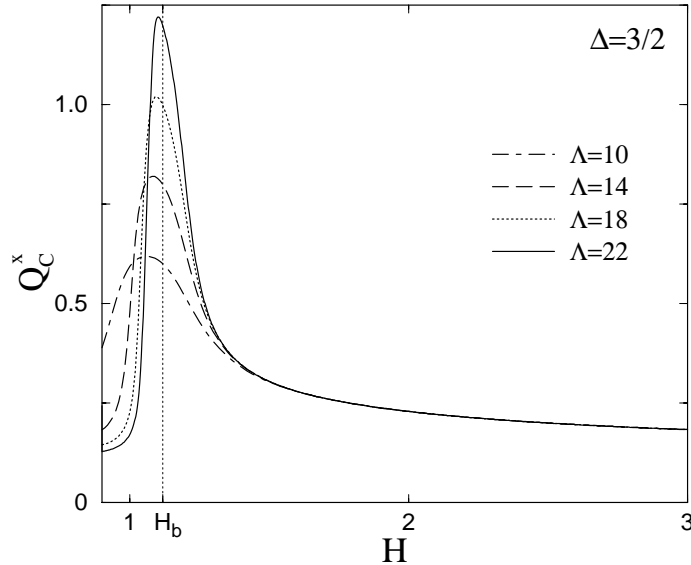


**Figure 4.3:** The transition amplitude per site  $Q_C^x$  corresponding to the  $C$  resonance line for field applied along the  $x$  axis.

where  $E_{\psi_0}$  and  $E_{\psi_1}$  are the energies of the  $|\psi_0\rangle$  and  $|\psi_1\rangle$  states respectively. In fact in region  $H > H_b$   $\omega_C$  is equal to the energy gap and can accurately be determined by extrapolation of our Lanczos results. For the special case of  $\Delta = 3/2$  the results are depicted in figure 4.1 by line C.

The transition amplitudes per site

$$Q_C^x = \frac{|\langle \psi_0 | M^x | \psi_1 \rangle|^2}{\Lambda \langle \psi_0 | \psi_0 \rangle \langle \psi_1 | \psi_1 \rangle}, \quad Q_C^y = \frac{|\langle \psi_0 | M^y | \psi_1 \rangle|^2}{\Lambda \langle \psi_0 | \psi_0 \rangle \langle \psi_1 | \psi_1 \rangle}, \quad (4.16)$$

are then numerically calculated and extrapolated for the determination of the corresponding absorption intensities per site  $I_C^{x,y} = I^{x,y}(\omega_C)/\Lambda$ . We find that  $Q_C^x$  diverges with  $\Lambda$  for fields close to  $H_b$  while converging behavior is restored for fields in the region  $H \gtrsim \Delta$  as it is shown in figure 4.3. Yet, the corresponding intensity  $I_C^x$  scales smoothly with  $\Lambda$  suggesting that the scaling behavior of  $Q_C^x$  might be connected to that of  $\omega_C$ . For the case of the  $y$  direction we find that both  $Q_C^y$  and  $I_C^y$  converge rapidly with increasing  $\Lambda$ . The extrapolated intensities per site for the case of  $\Delta = 3/2$  are shown in figure 4.4.

In order to understand the diverging behavior of  $Q_C^x$  in the region of  $H_b$  we use our analytical result (3.32) for its explicit calculation. A reasonable

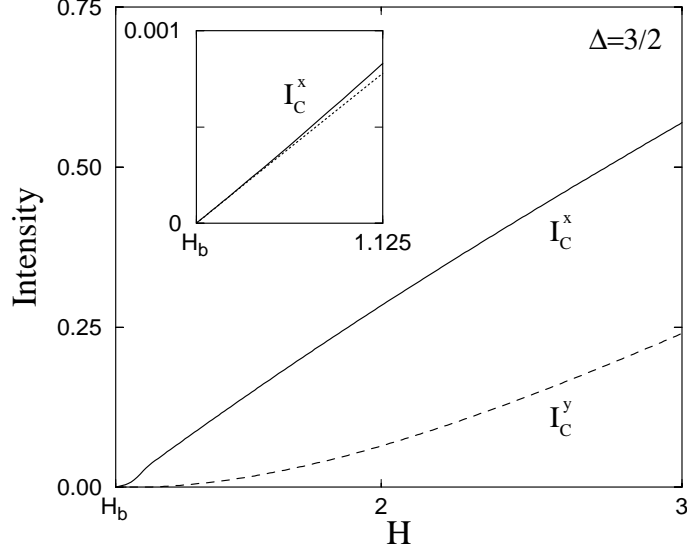


**Figure 4.4:** The numerically calculated absorption intensities per site occurring at frequency  $\omega_C$  for field applied in either the  $x$  and  $y$  direction and  $\Delta = 3/2$ . The inset compares with the analytic approximation for  $H \simeq H_b^+$  described in the text.

amount of combinatorics leads to

$$\langle \psi_0 | M^x | \psi_1 \rangle = \frac{1}{2} \sum_{\nu=0}^N \left( \frac{N-\nu}{\sqrt{q}} + \nu\sqrt{q} \right) \left[ \frac{N!}{(N-\nu)!\nu!} \right]^2 q^{N-2\nu}. \quad (4.17)$$

Its asymptotic behavior can then be found by expressing our result with respect to  $\langle \psi_0 | \psi_0 \rangle$  and  $I_N$  of equations (3.35) and (3.36) respectively to produce

$$Q_C^x = \frac{\Lambda^2}{8(\Delta+1)}. \quad (4.18)$$

For  $H \rightarrow H_b^+$  a straightforward application of the Feynman-Helman theorem yields

$$\omega_C \simeq (M_1 - M_0)(H - H_b) \quad (4.19)$$

while for large  $\Lambda$  from equation (3.38) we obtain

$$M_1 - M_0 = \frac{1}{\Lambda} \sqrt{\Delta^2 - 1}. \quad (4.20)$$

Using equations (4.18) (4.20) in (4.10) we obtain the absorption intensity per site for fields slightly above  $H_b$

$$I_C^x \simeq \frac{1}{4} \sqrt{\frac{\Delta-1}{\Delta+1}} (H - H_b) \quad (4.21)$$

where we have again scaled the result by two in order to account for the  $|\psi_0\rangle \rightarrow |\psi_{-1}\rangle$  transitions. The intensity calculated from (4.21) is depicted in the inset of figure 4.4 by the dashed line and we can see that it is in very good agreement with the corresponding extrapolated results for fields  $H \rightarrow H_b^+$ .

The  $\Delta$  dependence of the absorption spectrum for  $H > H_b$  can be found by numerical calculation on short chains. The general qualitative picture for the frequency  $\omega_C$  can be derived by noting that the C line for large fields coincides with its Ising asymptote depicted by the dashed line of figure 4.1.

### 4.3 Surface spin-flop transition

We now consider an open chain with  $\Lambda = 2N$  in order to investigate the absorption intensity spectrum that might be due to the existence of open boundaries.

Similarly to the case of the closed chain for  $H < H_s$  the ground states of the system are the two fully polarized states with  $\tau = N$  and  $\tau = -N$  thus low temperature contributions to the absorption intensity will be due to transitions from states  $|F_A\rangle, |F_B\rangle$  to one magnon states. Again we only study transitions from  $|F_A\rangle$  to states with  $\tau = N - 1$ .

Numerical calculations of the relevant matrix elements on finite chains show that the dominant contributions to the absorption intensity spectrum are found in the close vicinity of frequencies  $\omega_A$  and  $\omega_B$  and are now caused by the sets of states that lie in the lower and upper limit of the one magnon continuum respectively. As the size of the system increases the resulting frequencies and intensities converge rapidly to those of equations (4.12), (4.14) as expected.

Our results show that there is also significant contribution from transitions to the surface modes  $|1\rangle, |1'\rangle$ . Specifically, the  $|F_A\rangle \rightarrow |1\rangle$  transition causes a distinct resonance line throughout the  $H < H_s$  region at frequency equal to

$$\omega_1 = E_1(H), \quad (4.22)$$

where  $E_1(H)$  is the energy of the surface mode  $|1\rangle$  for bias field  $H$  given by equation (3.17). On the other hand the  $|F_A\rangle \rightarrow |1'\rangle$  transition causes a line at frequency  $\omega_{1'} = E_1(-H)$  for  $H < H_0$  while above  $H_0$  the  $|1'\rangle$  state enters

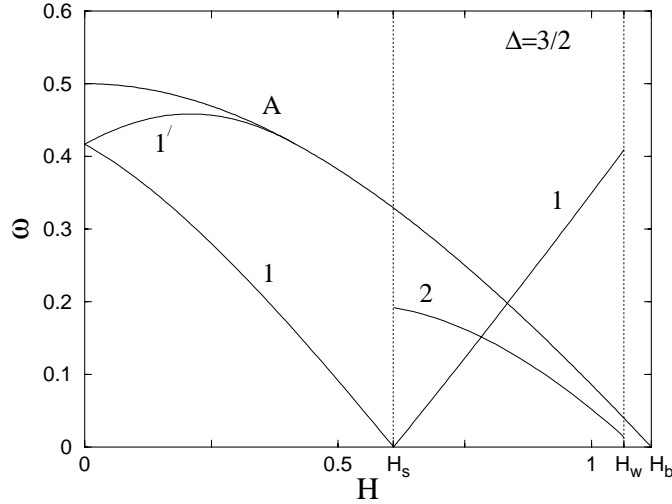


**Figure 4.5:** The resonance lines corresponding to surface transitions. The  $A$  line corresponds to the bulk transition described in section 4.2.

the continuum contributing to the intensity of the  $A$  resonance line. The frequencies  $\omega_1$ ,  $\omega_{1'}$  for the case of  $\Delta = 3/2$  are displayed in figure 4.5.

The transition amplitudes for the  $|F_A\rangle \rightarrow |1\rangle$  transition can be calculated from our analytical result (3.17) and are found to be rather insensitive to chain size. For large  $\Lambda$  we find

$$\frac{|\langle F_A | M^x | 1 \rangle|^2}{\langle F_A | F_A \rangle \langle 1 | 1 \rangle} = \frac{\Xi}{4} \frac{(1+r)^2}{1+r^2}, \quad \frac{|\langle F_A | M^y | 1 \rangle|^2}{\langle F_A | F_A \rangle \langle 1 | 1 \rangle} = \frac{\Xi}{4} \frac{(1-r)^2}{1+r^2}, \quad (4.23)$$

where

$$r = \frac{1}{2} \frac{1 + \xi_1}{\Delta + H - E}, \quad \Xi = \frac{1 + \xi_1}{1 - \xi_1} \quad (4.24)$$

and  $\xi_1$  is given by equation (3.17). The corresponding intensities are

$$I_1^x = \frac{\omega_1}{4} \frac{\Xi (1+r)^2}{1+r^2}, \quad I_1^y = \frac{\omega_1}{4} \frac{\Xi (1-r)^2}{1+r^2}, \quad (4.25)$$

and for the case of  $\Delta = 3/2$  they are displayed in figure 4.6.

For fields in the region  $H_s < H < H_w$  the surface state  $|1\rangle$  becomes the ground state of the system. From (4.9) we see that the possible transitions will now be from  $|1\rangle$  to the  $|F_A\rangle$  state as well as to states of the two-magnon sector with  $\tau = N - 2$ .

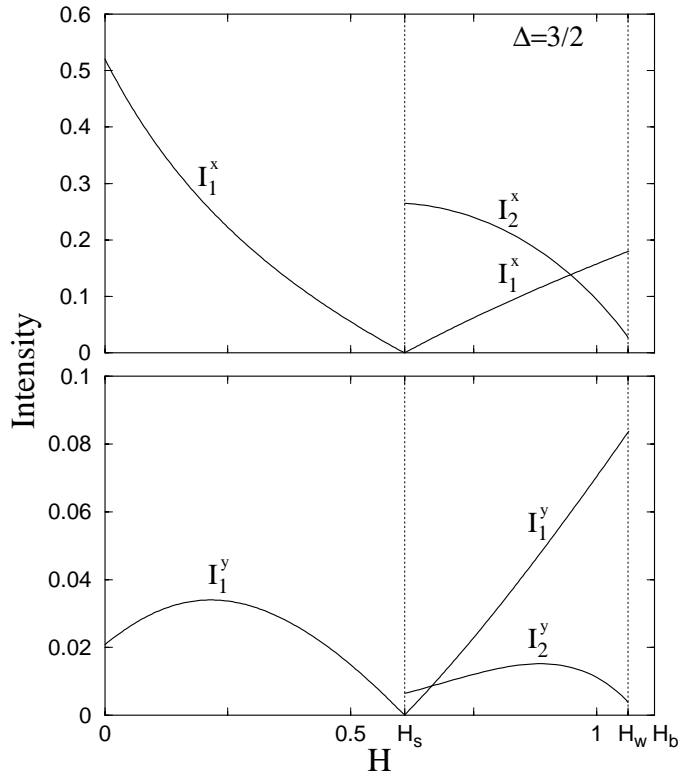


**Figure 4.6:** The absorption intensities of the main surface transitions.

The first possibility  $|1\rangle \rightarrow |F_A\rangle$  involves the transition amplitudes of equation (4.23) and will cause a resonance line at frequency

$$\omega_1 = E_{F_A} - E_1 = |E_1|. \quad (4.26)$$

The corresponding absorption intensity is found from equations (4.25) where  $\omega_1$  is now given by equation (4.26). The results for the special case of  $\Delta = 3/2$  are shown in figure 4.6.

The numerical calculation of the matrix elements involving two-magnon states shows that the A and B resonance lines are now caused by transitions from the state  $|1\rangle$  to bound states of the  $\tau = N - 2$  sector. For large  $\Lambda$  their frequency and intensity rapidly converge to the values calculated from equations (4.12), (4.14).

Additional to bulk transitions we find that there is also contribution caused by a transition to the lowest lying state of the two-magnon sector  $|2\rangle$ . This is actually a surface state and we find the frequency and matrix

elements of the  $|1\rangle \rightarrow |2\rangle$  transition to be rather insensitive to chain size. Our results for  $\omega_2$  and the corresponding intensity  $I_2^{x,y}$  on short chains have stabilized to several significant figures and for  $\Delta = 3/2$  they are shown in figure 4.6.

In the region  $H_w < H < H_b$  the ground state strongly depends on the specific value of  $\Delta$  and it is difficult to provide a complete picture of the occurring transitions. Yet, the A and B resonance lines of the closed chain are still present and for large  $\Lambda$  they are found by equations (4.12) (4.14).

Finally, for  $H > H_b$  there are no new transitions of physical importance that are induced by the boundaries and the resulting spectrum of the open chain practically coincide with that of the closed chain.

## 4.4 Conclusion

We have provided an analysis of the ESR spectrum of both surface and bulk spin flop transitions. We have seen that the resulting spectrum probes the energy excitation gap for all values of the bias field. Surface transitions give significant contribution that occur at frequencies which are distinct from those corresponding to bulk modes. Furthermore, the resulting absorption spectrum of either bulk or surface transitions is relatively insensitive to the size of the chain making the identification of the different resonance lines possible.

If a magnetic system described by our model (3.1) is doped with non-magnetic ions so that a statistically significant number of open boundaries is created, transitions to surface modes can cause experimentally measurable absorption intensity. The different phases of the system can then be probed by the emerging spectrum whereas the SSF and BSF phase transitions are identified by the closing of the corresponding excitation gap.

To summarize ESR spectroscopy proves to be very efficient for the study and of the bulk and the surface spin-flop phase transitions of magnetic materials that are in the region of parameters of our model (3.1).



# CHAPTER 5

## THERMODYNAMICS

### 5.1 Introduction

In this chapter we study [44] thermodynamic properties of our model (3.4) like the specific heat and the magnetization as functions of the applied magnetic field and the temperature. The most straightforward method for the calculation of thermodynamic properties is by evaluating the partition function from the complete set of energy eigenvalues. This demands a complete numerical diagonalization of the Hamiltonian which is possible only for small chains ( $\Lambda \simeq 14$ ) while a reliable extrapolation to larger values of  $\Lambda$  is difficult.

The most powerful method for studying thermodynamic properties of quasi one-dimensional quantum lattice models with short range interactions is the transfer matrix renormalization group (TMRG) method [59–61]. This method addresses directly the thermodynamic limit while it is possible to reach very low temperatures of the order of  $T = 0.01J$ . TMRG is based on a Trotter-Suzuki [62, 63] decomposition of the partition function leading to the construction of the quantum transfer matrix (QTM). In the thermodynamic limit the calculation of thermodynamic quantities reduces to the determination of the maximum eigenvalue and the corresponding eigenvector of the QTM. The dimension of the quantum transfer matrix becomes very large for low temperature calculations and requires the use of a density matrix renormalization group (DMRG) method.

The DMRG method [59, 60, 64, 65] is a numerical technique for finding accurate approximations to the ground state and the low-lying excited states of large strongly interacting quantum lattice systems. The numerical renormalization group (RG) treatment was used for the first time by Wilson [66] for the solution of the Kondo problem. It is actually a variational diagonalization scheme that truncates the relevant Hilbert space. In the DMRG method the density matrix [59, 67] is used in the calculation for the selection of the optimal base of the truncated space.

In section 5.2 we present a TMRG calculation for the magnetization at finite temperature while the zero temperature limit is consistent with results obtained by extrapolation of our Lanczos results of chapter 3. Specific heat calculations are presented in section 5.3 with a detailed analysis of low temperature behavior in respect to anomalous scaling. A discussion on the origin of the anomalous scaling phenomena and the validity of the dilute magnon approximation is given in section 5.4. Our main conclusions are summarized in section 5.5.

## 5.2 Magnetization

Our analytical results of chapter 3 (eqs. (3.40), (3.41)) allow us to check that the  $T = 0$  magnetization converges rapidly with increasing  $\Lambda$  for  $H = H_b$ . For example the magnetization jump at the critical field calculated by our Lanczos method for  $\Lambda = 22$  differs from the analytical prediction (3.41) by about 5%, a difference that is rectified by Richardson extrapolation to an accuracy about one part in a thousand. Hence we have applied the same extrapolation to our Lanczos results for  $H > H_b$  and the result is depicted by the solid line in figure 5.1. Extrapolation becomes unnecessary for  $H \gtrsim \Delta$  leading us to believe that we have calculated the magnetization of the thermodynamic limit with an accuracy better than 0.1% for all  $H \geq H_b$ .

We now apply our TMRG algorithm to calculate the temperature dependence of the magnetization which is shown in figure 5.2 for a number of field values. The magnetization vanishes for all temperatures at vanishing field. For finite fields in the subcritical region,  $H < H_b$ , the magnetization again vanishes at  $T = 0$ , as expected, but develops a maximum at some finite temperature. Right at the critical field,  $H = H_b$ , the  $T = 0$  limit of the

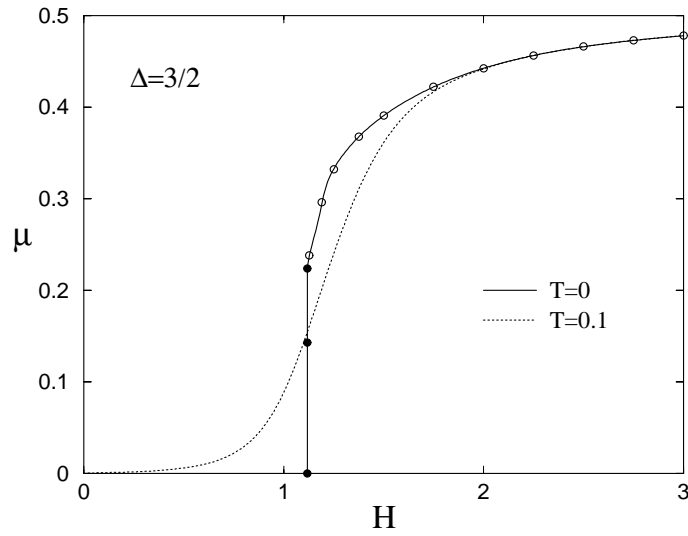


**Figure 5.1:** Field dependence of the average magnetization per site  $\mu = M/\Lambda$  for  $T = 0$  (solid line) and  $T = 0.1$  (dotted line). The solid circles represent the values of the  $T = 0$  magnetization just below  $H_b$  ( $\mu = 0$ ), right at  $H_b$  ( $\mu_b = 0.143$ ), and just above  $H_b$  ( $\mu_0 = 0.224$ ). The meaning of the open circles is discussed in the text.

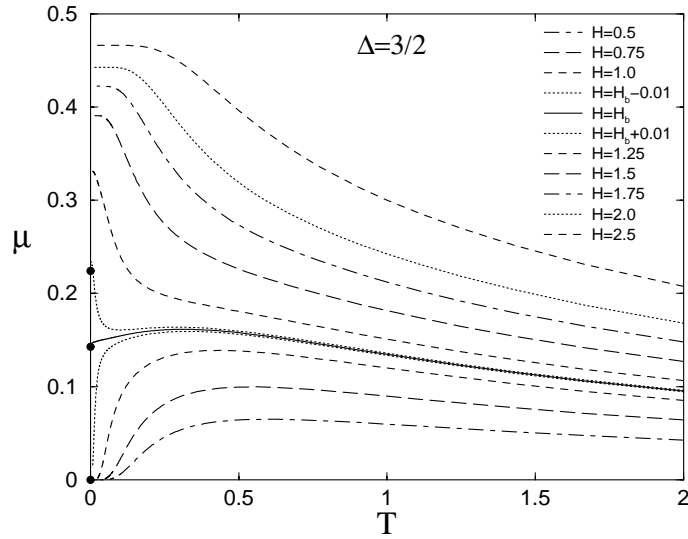


**Figure 5.2:** Temperature dependence of the magnetization for various field values throughout the BSF transition. The solid circles on the  $\mu$  axis correspond to the same values as those of figure 5.1.

calculated curve is consistent with the value  $\mu_b = 0.143$  of equation (3.39), applied for  $\Delta = 3/2$ , whereas just above  $H_b$  the  $T = 0$  limit is consistent with the value  $\mu_0 = 0.224$  of equation (3.40). For supercritical fields,  $H > H_b$ , the low-temperature limiting values of  $\mu$  extracted from figure 5.2 are depicted by open circles in figure 5.1 and are thus seen to be in excellent agreement with our independent Lanczos calculation of the magnetization at  $T = 0$ . Similarly the results extracted from figure 5.2 at the specific temperature  $T = 0.1$  were used to calculate the field dependence of the magnetization at this temperature, a result that is shown by a dotted line in figure 5.1 and illustrates the manner in which the  $T = 0$  magnetization jump at the critical point is smoothed out at finite temperature.

### 5.3 Specific heat

We thus arrive at the main point of this chapter, namely the calculation of the specific heat via a TMRG algorithm [60, 68]. In figure 5.3 we compare the TMRG result at vanishing field with a finite-size calculation for chains with  $\Lambda = 10, 12$ , and 14 for which a complete numerical diagonalization of the Hamiltonian is possible. This comparison is surprising in that the trend of the finite-size results does not seem to be consistent with the calculated thermodynamic limit. We have thus naturally questioned the validity of our TMRG calculation. However this special case was also considered in figure 4(b) of a paper by Klümper [69] whose numerical method is again based on a transfer matrix but relies heavily on the complete integrability of model (3.4) at vanishing staggered field. Direct correspondence with the above author established that our result agrees with his throughout the temperature range considered.

The “anomalous scaling” observed in figure 5.3 for  $H = 0$  persists for nonvanishing fields throughout the BSF transition but gradually disappears in the “no-scaling region”  $H \gtrsim \Delta$  where the correct thermodynamic limit is practically reached by very short chains, as short as  $\Lambda = 4$ . In any case, the TMRG calculation of the temperature dependence of the specific heat is illustrated in figure 5.4 for various field values. The main feature of this figure is that the specific heat develops a double peak for fields in the vicinity of the critical point  $H_b$ . Furthermore the low-temperature behavior appears to

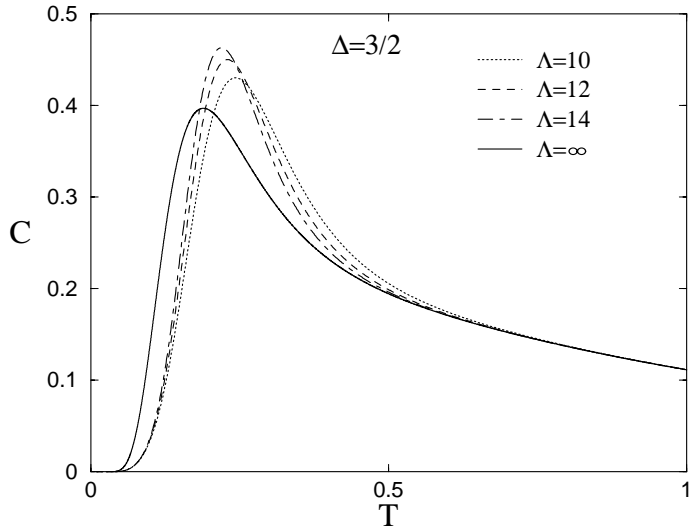


**Figure 5.3:** Temperature dependence of the specific heat per site  $C$  at vanishing field ( $H = 0$ ).

be generally consistent with the field dependence of the magnon gaps shown in figure 4.1.

One would expect that the low-temperature specific heat is correctly predicted by a dilute-magnon or spinwave approximation, a long cherished assumption in condensed matter physics. To check this assumption we first consider the case of vanishing field for which our model is formally identical to the ferromagnetic XXZ chain extensively studied through the Bethe Ansatz [49, 69]. At sufficiently low temperature the spinwave approximation of the specific heat should read

$$C \approx \frac{G_-^2 \exp(-G_-/T)}{(2\pi T^3)^{1/2}}, \quad G_- = \Delta - 1, \quad (5.1)$$

where  $G_-$  is the lowest magnon gap at vanishing field. Equation (5.1) suggests considering the quantity  $-T \ln(T^{3/2}C)$  which should interpolate linearly to the magnon gap  $G_-$  at  $T = 0$ . Yet a comparison of the spinwave prediction (5.1) with the TMRG calculation shown in the  $\Delta = 3/2$  entry of figure 5.5 reveals a sharp disagreement even at the lowest temperature accessible by our method. On the other hand, one can show that the spinwave approximation agrees well with the finite-size results for  $\Lambda = 10, 12, 14$  given in figure 5.3 restricted to the temperature range of figure 5.5. Clearly then the

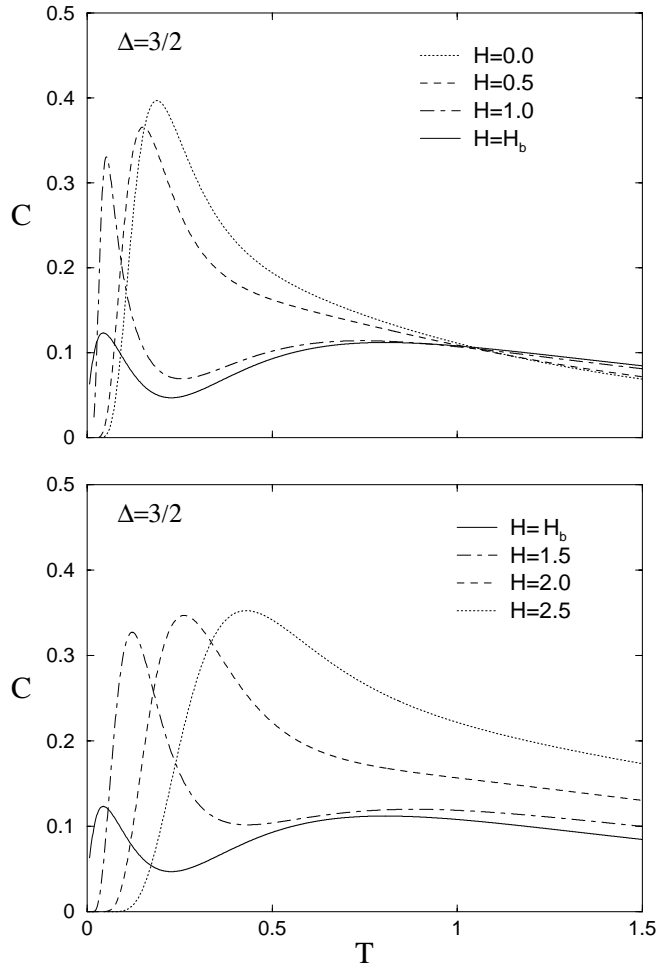


**Figure 5.4:** Specific heat for various field values throughout the BSF transition.

anomalous scaling noted earlier is intimately related to the apparent failure of the dilute-magnon approximation.

In order to understand this situation we now invoke an asymptotic result obtained for the ferromagnetic XXZ chain by Johnson and Bonner [49] who predict that the low-temperature specific heat is more appropriately described by

$$C \approx \frac{G_-^2 \exp(-G_-/T)}{(2\pi T^3)^{1/2}} + \frac{G_1^2 \exp(-G_1/T)}{T^2}, \quad (5.2)$$

$$G_1 = \frac{1}{2} \sqrt{\Delta^2 - 1},$$

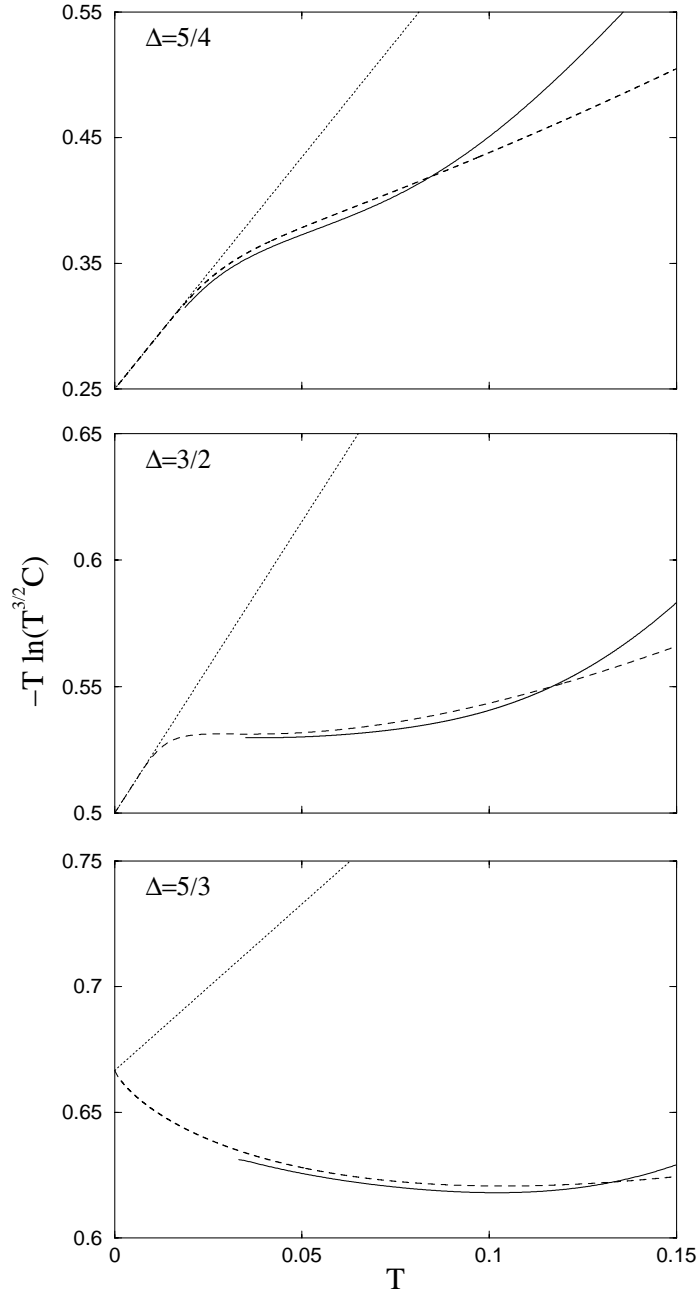


**Figure 5.5:** Comparison of the calculated specific heat (solid line) at vanishing field ( $H = 0$ ) with the spinwave approximation (5.1) (dotted line) and the Johnson-Bonner prediction (5.2) (dashed line).

where a new gap  $G_1$  is potentially important. The two gaps  $G_-$  and  $G_1$  become equal at the critical anisotropy  $\Delta = 5/3$  and are ordered as  $G_- < G_1$  or  $G_- > G_1$  for  $\Delta < 5/3$  or  $\Delta > 5/3$ .

Therefore, when  $1 < \Delta < 5/3$ , the magnon contribution in equation (5.2) dominates for sufficiently low temperature, practically in the region  $T \ll G_1 - G_- \equiv \delta$ . For  $\Delta = 3/2$  one finds that  $\delta = 0.06$  and hence the region  $T \ll \delta$  is difficult to approach by the inherently finite-temperature TMRG algorithm. This explains the apparent failure of spinwave theory demonstrated in the  $\Delta = 3/2$  entry of figure 5.5. However, when both terms of Equation (5.2) are included, the agreement with our TMRG result is obviously very good. The picture becomes more transparent in the  $\Delta = 5/4$  entry of figure 5.5 where the differential gap  $\delta = 0.125$  is greater and thus the region  $T \ll \delta$  becomes accessible to TMRG, albeit somewhat marginally. Also interesting is the result for the critical anisotropy  $\Delta = 5/3$  shown in figure 5.5, where the failure of spinwave theory becomes complete, whereas our result continues to agree with the Johnson-Bonner prediction (5.2). Finally we have examined the case of a supercritical anisotropy,  $\Delta = 2$ , with a similar conclusion.

At finite (staggered) field our model is not equivalent to the ferromagnetic XXZ chain and thus the finite-field results of reference 49 are no longer applicable. We do not know at this point how to generalize equation (5.2) to account for a staggered field, especially because complete integrability seems to be lost. Numerical investigation of this issue suggests that spinwave anomalies persist in the subcritical region  $H < H_b$  while normal spinwave behavior is restored for  $H > H_b$ . In the latter region the quantity  $-T \ln(T^{3/2}C)$  interpolates linearly to the magnon gap  $G$  shown in figure 4.1.

## 5.4 Johnson-Bonner anomalies

In order to understand the origin of the new gap  $G_1$  we examine the Ising model which presents similar low temperature anomalous scaling behavior.

The energy levels of a cyclic ferromagnetic Ising chain (ring) appear at  $E = 0, 2|J|, 4|J|, \dots$ , where  $J$  is the exchange parameter, therefore one would expect the low temperature behavior of the specific heat to be governed by an energy gap of  $2|J|$ . The exact partition function for an Ising ring can

be found to be [14]

$$Z_\Lambda = 2^\Lambda [\cosh^\Lambda(J/T) + \sinh^\Lambda(J/T)]. \quad (5.3)$$

We may see from a series expansion of equation (5.3) that there is an “accidental” canceling of the odd powers of  $e^{J/T}$  for any finite  $\Lambda$  thus causing an effective gap of  $2|J|$  which is equal to the lowest excitation energy of the Ising ring. The canceling is due to the effect of the  $\sinh^\Lambda(J/T)$  term which is completely negligible in the thermodynamic limit  $\Lambda \rightarrow \infty$  resulting in an effective gap of  $J$ . This means that in the thermodynamic limit the low temperature behavior is not determined just by the low-lying states but may be governed by all the energy levels.

Using the Ising model as their starting point Johnson and Bonner [49] proposed that in the thermodynamic limit of the zero field XXZ model the effective gap depends on both the energies and the degeneracy of the lowest lying excitations. Specifically, they suggested that an energy level  $E$  with multiplicity of the order  $O(N^r)$  produce an effective gap of  $E/r$ ; e.g. the degeneracy of the  $2|J|$  energy state of the Ising ring is of order  $O(N^2)$  and should induce an effective gap  $|J|$  which is consistent with the exact result. In this interpretation the effective gap  $G_1$  of our model is found to originate from bound multimagnon or domain wall states predicted by the Bethe Ansatz solution to rise at energy  $\sqrt{\Delta^2 - 1}$  [49, 56], including the notorious factor  $1/2$  due to their multiplicity.

The most important conclusion of this analysis is that the dilute magnon approximation can sometimes fail to predict the correct low temperature behavior of quantum spin systems. Furthermore, as we can see in figures 5.4, its validity can be restricted to very low temperatures which may be difficult to reach either experimentally or by numerical calculations. In every case the dilute magnon predictions should be corroborated by more accurate calculations.

## 5.5 Conclusion

We have presented a reasonably complete theoretical description of the thermodynamics of the spin-flop transition for Hamiltonian (3.4). The calculated specific heat exhibits a double peak at the critical field  $H_b$  which might

be related to the special character of the BSF transition while anomalous scaling phenomena are present throughout a wide range of parameters. Our explicit results would be directly relevant for the analysis of actual experiments, provided that a quasi-one-dimensional magnetic system is found that is described by our model Hamiltonian at least approximately [55]. On the other hand we have checked that the TMRG algorithm provides exceptional accuracy even under stringent conditions while it can be trivially adjusted to handle a general class of spin systems without relying on integrability.

## CHAPTER 6

# SPIN-1 PLANAR FERROMAGNET $\text{CsNiF}_3$

### 6.1 Introduction

In this chapter [45] we apply the DMRG and TMRG methods, described in chapter 5, to study the magnetic compound  $\text{CsNiF}_3$ .  $\text{CsNiF}_3$  has been the subject of a number of experimental investigations which suggest that it undergoes three-dimensional (3D) ordering at very low temperatures,  $T < T_N = 2.7$  K, but exhibits essentially one-dimensional (1D) behavior for  $T > T_N$ . It is believed that an appropriate 1D model is described by the spin  $s = 1$  Hamiltonian

$$W = \sum_n [-J\mathbf{S}_n \cdot \mathbf{S}_{n+1} + A(S_n^z)^2 - g\mu_B\mathbf{H} \cdot \mathbf{S}_n], \quad (6.1)$$

which contains a ferromagnetic ( $J > 0$ ) isotropic exchange interaction and an easy-plane ( $A > 0$ ) single-ion anisotropy, in addition to the usual Zeeman term produced by an applied field  $\mathbf{H}$ .

The derivation of accurate theoretical predictions based on Hamiltonian (6.1) turned out to be more difficult than anticipated thanks to the strong quantum fluctuations that occur in this quasi-1D system. In particular, the leading-order magnon dispersion derived within the usual  $1/s$  expansion is too crude an approximation for  $s = 1$ . As a result, inelastic neutron scattering experiments were analyzed [70] mostly on the basis of an alternative dispersion derived by Lindgard and Kowalska [71] using a self-consistent approach that is designed to properly account for single-ion anisotropy. Sim-

ilarly, a large body of experimental data became available for thermodynamic quantities such as magnetization, susceptibility, and specific heat, but a corresponding theoretical calculation proceeded slowly. To the best of our knowledge, the most accurate calculation of thermodynamics was provided by Delica et al [72] based on a quantum transfer matrix, while comparable success was claimed more recently by Cuccoli et al [73] through a sophisticated semiclassical approach. The above two papers also contain an extensive list of references to earlier work.

It is our aim in this chapter to derive theoretical predictions that are accurate to within line thickness and thus provide a safe basis for the discussion of various issues that have been raised during the long history of this subject.

In section 6.2, experimental data on the magnon dispersion are analyzed in terms of an unconventional  $1/n$  expansion [74] which is shown to contain the Lindgard-Kowalska dispersion as a special case. The accuracy of the leading  $1/n$  approximation is confirmed by an independent calculation of the field dependence of the magnon gap using a DMRG method [64, 65], while a discussion of anharmonic corrections within the conventional  $1/s$  expansion is also included for comparison. Thermodynamic quantities are calculated in section 6.3 by a powerful TMRG algorithm [59–61]. We are thus in a position to appreciate the relative accuracy of earlier calculations, analyze all available data and anticipate results of possible future experiments, as well as challenge popular interpretations in terms of sine-Gordon solitons. A brief summary of the main conclusions is given in section 6.4.

## 6.2 The magnon dispersion

The standard spinwave theory is a method for calculating quantum corrections around the classical minimum of Hamiltonian (6.1) by a systematic  $1/s$  expansion. The  $1/n$  expansion developed in reference 74 is of a similar nature, except that the corresponding “classical” minimum is a variational Hartree-like ground state that is more sensitive to the nature of single-ion anisotropy and thus provides a more sensible starting point. Hence one obtains an accurate magnon dispersion even if the  $1/n$  series is restricted to the harmonic approximation.

For a field applied in a direction perpendicular to the  $c$ -axis, e.g.,  $\mathbf{H} =$

$(H, 0, 0)$ , the magnon energy at crystal momentum  $q$  is given by

$$\omega_q = 2J \left\{ (1 + \varepsilon) \left( \frac{\alpha}{4\varepsilon} - \cos q \right) \left[ \frac{\alpha}{4\varepsilon} (1 + \varepsilon) - (1 - \varepsilon) \cos q \right] \right\}^{1/2} \quad (6.2)$$

Here and in the rest of this chapter we employ rationalized parameters for anisotropy and field,

$$\alpha = A/J, \quad h = g_{\perp} \mu_B H/J, \quad (6.3)$$

while energy and temperature may be measured in units of the exchange constant  $J$ . The notation employed for the gyromagnetic ratio  $g_{\perp}$  implies that the corresponding ratio  $g_{\parallel}$  for a field parallel to the  $c$ -axis may be different. Finally, the dimensionless parameter  $\varepsilon$  in equation (6.2) is determined in terms of  $\alpha$  and  $h$  by the algebraic equation

$$\varepsilon = \frac{\alpha(1 - \varepsilon^2)^{1/2}}{2h + 4(1 - \varepsilon^2)^{1/2}}. \quad (6.4)$$

One should add that derivation of systematic  $1/n$  corrections to the harmonic approximation (6.2) is possible [74] but unnecessary in the parameter range of current interest:  $\alpha, h < 0.5$ .

At zero field, the root of equation (6.4) is  $\varepsilon = \alpha/4$  which is inserted in equation (6.2) to provide a completely explicit expression for the magnon dispersion. For nonzero field, equation (6.4) may be solved by simple iteration starting with  $\varepsilon = 0$ . In fact, the result of a single iteration,

$$\varepsilon \simeq \frac{\alpha}{2h + 4}, \quad (6.5)$$

is practically indistinguishable from the exact root of equation (6.4) for parameters such that  $\alpha, h < 0.5$ . The last remark becomes especially important if one notes that the dispersion obtained by inserting the approximate root (6.5) in equation (6.2) is precisely the magnon dispersion derived earlier by Lindgard and Kowalska [71], applied for  $s = 1$ , which was in turn employed for the analysis of experimental data from inelastic neutron scattering [70].

The latter analysis provided what is often referred to as the standard set of parameters for  $\text{CsNiF}_3$ :

$$J = 23.6 \text{ K}, \quad A = 9 \text{ K}, \quad g_{\perp} = 2.4. \quad (6.6)$$

The corresponding theoretical predictions of the magnon dispersion (6.2) are compared to experimental data [70] in the upper panel of figure 6.1. The agreement is obviously very good for field  $H = 41$  kG, while a slight but systematic deviation is observed for  $H = 0$ . This conclusion is somewhat surprising in view of the claim in reference 70 that nearly perfect agreement is obtained for both field values, even though the Lindgard-Kowalska dispersion employed in the above reference is practically identical to equation (6.2) for the set of parameters (6.6). The systematic nature of this discrepancy makes it unlikely that the data communicated to us by Steiner [75] differs from the data actually used in the analysis of reference 70. A more likely explanation is that the Lindgard-Kowalska dispersion was further approximated by the authors of reference 70, as is evident in the expression for the magnon gap given in their equation (5).

Although the observed discrepancy appears to be minor, it nonetheless leads to a substantial redefinition of parameters. Thus we have redetermined the exchange constant  $J$  and anisotropy  $A$  by a least-square fit of the zero-field data to dispersion (6.2), while the gyromagnetic ratio was subsequently obtained by a one-parameter least-square fit of the  $H = 41$  kG data. The resulting new set of parameters

$$J = 23.6 \text{ K}, \quad A = 11 \text{ K}, \quad g_{\perp} = 2.18 \quad (6.7)$$

restores agreement with experiment for both field values, as is shown in the lower panel of figure 6.1. A notable feature of equations (6.6) and (6.7) is that the exchange constant has remained unchanged. Indeed, throughout our analysis, we found no evidence for departure of the exchange constant from the value  $J = 23.6$  K which will thus be adopted in the following without further questioning.

In contrast, the observed significant fluctuations in the anisotropy constant  $A$  and gyromagnetic ratio  $g_{\perp}$  simply reflect the fact that the magnon dispersion is not especially sensitive to those parameters. Therefore, their values given in either equation (6.6) or (6.7) cannot be considered as established without further corroboration. Now, the reduced value of the gyromagnetic ratio given in equation (6.7) is consistent with  $g_{\perp} = 2.1 \pm 0.05$  obtained independently by measuring the saturation magnetization at strong fields [72] and is also supported by the analysis of the zero-field susceptibility in section

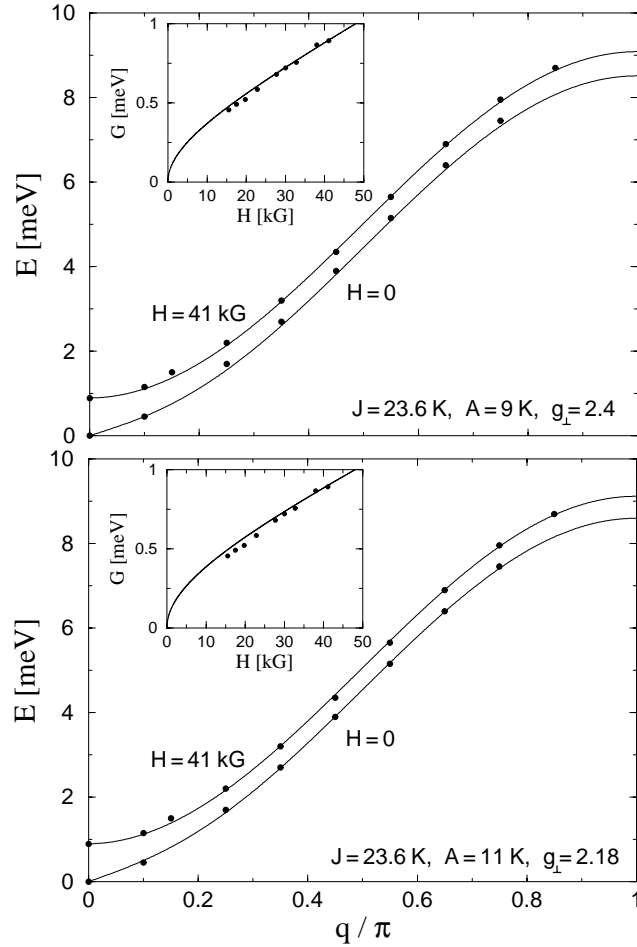


**Figure 6.1:** The magnon energy  $E = \omega_q$  as a function of crystal momentum  $q$  calculated from equation (6.2) for two values of the applied field,  $H = 0$  and  $H = 41$  kG, and two different sets of parameters. The insets illustrate the corresponding field dependence of the  $q = 0$  magnon gap  $G$  calculated from equation (6.8). Solid circles represent experimental data from reference 70 taken at  $T = 4.2$  K.

6.3. But a proper choice of the anisotropy constant  $A$  will be a matter of debate throughout this chapter. In this respect, one should keep in mind that the neutron data displayed in figure 6.1 were taken at helium temperature,  $T = 4.2$  K, which is relatively high but not too distant from the 3D-ordering transition temperature  $T_N = 2.7$  K. Hence, finite-temperature effects as well as deviations from ideal 1D behavior may already be present.

An important special case of the magnon dispersion (6.2) is the zero-momentum gap  $G = \omega_{q=0}$ , or

$$G = \left\{ g_{\perp} \mu_B H \left[ g_{\perp} \mu_B H + A \left( \frac{1 + \varepsilon}{1 - \varepsilon} \right)^{1/2} \right] \right\}^{1/2}, \quad (6.8)$$

where we have made use of the algebraic equation (6.3) to simplify the expression [74]. A comparison of the predictions of equation (6.8) with the measured field dependence of the magnon gap [71, 75] is shown in the insets of figure 6.1 for both sets of parameters. Although the overall agreement is reasonable, systematic deviations are present at relatively low field values in both cases. An attempt to redetermine the parameters by a least-square fit of the  $q = 0$  data to equation (6.8) yields values for  $A$  and  $g_{\perp}$  that would significantly compromise the agreement obtained at nonzero crystal momentum  $q$ .

Implicit in the preceding discussion is the presumption that the magnon dispersion (6.2) and its special case (6.8) are sufficiently accurate and there is no need to proceed with the calculation of anharmonic  $1/n$  corrections. We now test this assumption by a completely independent calculation of the field dependence of the magnon gap based on a DMRG algorithm [64, 65]. An early effort [76] to apply a renormalization-group technique was restricted to short chains (16 sites) and thus provided reasonable but not especially accurate estimates of the magnon gap. The DMRG algorithm allowed us to calculate the gap on long chains up to 400 sites. We have also tested the stability of our results through Shanks or Richardson extrapolation [51] and believe to have calculated the gap to an accuracy greater than the three figures actually displayed in the third column of Table 6.1.

It is then important that the corresponding results obtained through equation (6.8), listed in the second column of Table 6.1, are in agreement with the DMRG calculation. Since the relative accuracy is expected to fur-

$h$	Magnon gap $G$		
	$1/n$	DMRG	$1/s$
0.000	0.000	0.000	0.000
0.025	0.105	0.106	0.109
0.050	0.152	0.155	0.160
0.075	0.192	0.195	0.201
0.100	0.227	0.230	0.238
0.150	0.290	0.295	0.304
0.200	0.350	0.354	0.365
0.250	0.406	0.411	0.422
0.300	0.461	0.466	0.478
0.400	0.568	0.573	0.586
0.500	0.673	0.677	0.691

**Table 6.1:** Magnon gap in units of  $J$ , for a typical anisotropy  $\alpha = A/J = 0.38$ , and a field  $h = g_{\perp}\mu_B H/J$  applied in a direction perpendicular to the  $c$ -axis.

ther improve at nonzero crystal momentum  $q$ , one must conclude that the magnon dispersion (6.2) is sufficiently accurate for all practical purposes. Therefore, any disagreement between theory and experiment should be attributed to other reasons. In particular, one should note in Table 6.1 that the  $1/n$  results slightly underestimate the DMRG data and hence the latter cannot be used to eliminate the remaining small disagreement with the experimental data shown in the insets of figure 6.1.

Next we comment on the relative validity of the standard semiclassical theory based on a  $1/s$  expansion. The corresponding harmonic approximation of the magnon dispersion is clearly inaccurate, as is apparent in the estimate of anisotropy  $A = 4.5$  K encountered in the early literature [77]. However, the semiclassical prediction can be significantly improved by including the first (anharmonic)  $1/s$  correction. At zero field, a completely analytical calculation is possible and may be found in reference 78. For nonzero field, the anharmonic correction is expressed in terms of complicated integrals that cannot be computed analytically. Therefore, for simplicity, the main point is made here by considering only the  $q = 0$  magnon gap which

can be written as

$$\begin{aligned}
 G &= G_0 [1 + \delta/s + O(1/s^2)], \\
 G_0 &= sJ [h(h + 2\alpha)]^{1/2}, \quad \delta = \frac{\alpha}{h + 2\alpha} \left( \frac{1}{2} - I \right), \\
 I &= \frac{1}{\pi} \int_0^\pi dq \frac{1 - \cos q + h/2 + \alpha/4}{[(1 - \cos q + h/2)(1 - \cos q + h/2 + \alpha)]^{1/2}},
 \end{aligned} \tag{6.9}$$

where the rationalized field is now defined as  $h = g_\perp \mu_B H / sJ$  which differs from the definition given in equation (6.3) by a factor that becomes unimportant for  $s = 1$ .  $G_0$  is the (harmonic) classical approximation and  $\delta$  provides the first anharmonic correction which amounts to about 15 ~ 20% of the total answer. Numerical values for the gap calculated from equation (6.9), applied for  $s = 1$ , are listed in the fourth column of Table 6.1. These values overestimate the DMRG data by a wider margin than the *harmonic*  $1/n$  approximation underestimates the same data. Therefore, we again conclude that the magnon dispersion (6.2) and the magnon gap (6.8) provide the most accurate description.

Finally, we mention that an  $1/n$  expansion is also possible in the case of a field parallel to the  $c$ -axis, along the lines outlined in the Appendix of reference 74. Such a possibility will not be pursued further here, except for a minor application in section 6.3.2, mainly because we do not know of an experimental measurement of the magnon dispersion for this field orientation.

### 6.3 Thermodynamics

Since the calculation of the partition function through a complete diagonalization of the Hamiltonian is only possible on very short chains ( $\Lambda \simeq 7$ ) more powerful numerical methods proceed with the construction of a quantum transfer matrix (QTM) obtained by an  $M$ -step Trotter decomposition. An explicit calculation was initially performed via Quantum Monte Carlo sampling [79] and was also limited to short chains ( $\Lambda = 16$ ) and a relatively small number of Trotter steps ( $M = 12$ ). This procedure led to reasonable results for the magnetization and susceptibility, but the calculation of the specific heat was plagued by large statistical errors.

A more systematic QTM calculation was later accomplished [72] on long

chains ( $\Lambda \sim 150$ ) by limiting the number of Trotter steps ( $M \leq 6$ ) which allows an accurate diagonalization of the matrices involved in the Trotter decomposition. At first sight, a small  $M$  limits the calculation to high temperatures. However, Delica et al [72] extrapolate their results for  $M = 4, 5$  and 6 to higher values of  $M$  and thus obtain thermodynamic quantities that are expected to be accurate to within a few percent in the temperature region  $T > 0.16J \simeq 4$  K. This restriction is not crucial for application to  $\text{CsNiF}_3$  in view of the 3D-ordering transition below  $T_N = 2.7$  K which limits the validity of the 1D model anyway.

Our TMRG calculation [59–61] concentrates on the largest eigenvalue of the QTM and thus addresses directly the infinite-chain limit. The number of Trotter steps may be chosen to be as large as  $M \sim 160$  which leads to numerical results with an accuracy better than line thickness, down to temperature as low as  $T = 0.02J \simeq 0.5$  K which is one order of magnitude lower than the lowest temperature reached in earlier calculations. We find that the results of Delica et al [72] are reliable, within the anticipated limits of accuracy, whereas the more recent elaborate semiclassical calculation of Cuccoli et al [73] is not very accurate over the temperature region of current interest.

### 6.3.1 Field perpendicular to $c$

We begin with the discussion of the temperature dependence of the zero-field transverse susceptibility  $\chi_\perp$  measured sometime ago by Dupas and Renard [80]. The TMRG result for the standard set of parameters (6.6) is depicted by a dashed line in figure 6.2 and is seen to systematically deviate from the experimental data. The agreement with experiment for this set of parameters claimed by Cuccoli et al [73] is due to inaccuracies in their calculation, a point that will be made more explicit in our subsequent discussion of the specific heat.

Now, the transverse susceptibility  $\chi_\perp$  is found to be largely insensitive to the specific strength of anisotropy, as demonstrated in the inset of figure 6.2. On the other hand,  $\chi_\perp$  depends quadratically on the gyromagnetic ratio  $g_\perp$  and is thus very sensitive to its specific value. It is then important that a reasonable agreement with the data is achieved for the same value  $g_\perp = 2.18$

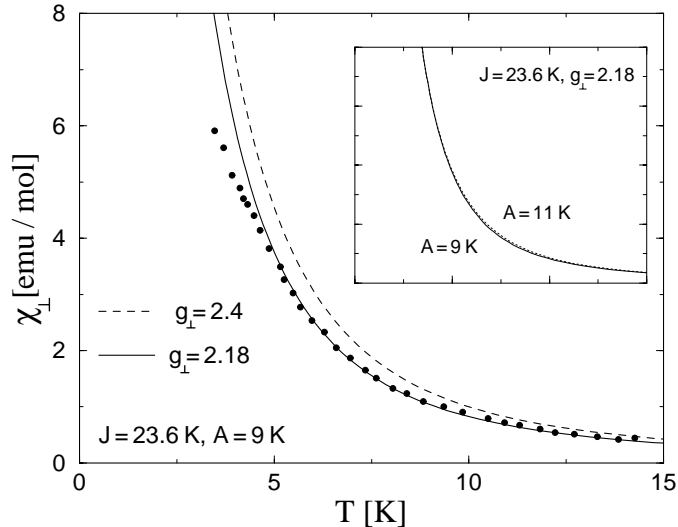


**Figure 6.2:** Comparison of TMRG predictions for the temperature dependence of the zero-field transverse susceptibility  $\chi_{\perp}$  with experimental data from reference 80 (solid circles). The dashed line corresponds to the standard set of parameters of equation (6.6) and the solid line to a lower value of the gyromagnetic ratio ( $g_{\perp} = 2.18$ ). The inset illustrates the calculated susceptibility for two values of anisotropy,  $A = 9$  K (solid line) and  $A = 11$  K (dotted line), which lead to virtually identical results.

obtained by our spinwave analysis of section 6.2, as shown by the solid line in the main frame of figure 6.2. The remaining systematic departure from the data observed for  $T \lesssim 5$  K could be due to a gradual onset of 3D ordering at low temperatures.

The above choice of the gyromagnetic ratio is further challenged by comparing, in figure 6.3, the TMRG prediction for the field dependence of the magnetization with experimental data taken at selected temperatures [72]. The specific value of  $A$  chosen in figure 6.3 is not important because the transverse magnetization is also not particularly sensitive to the strength of anisotropy. But the relatively low value  $g_{\perp} = 2.18$  was again important to improve agreement with the data. Yet a significant disagreement between theory and experiment is apparent in figure 6.3, even at relatively high temperatures. The lower value  $g_{\perp} = 2.1$  employed in reference 72 reduces but does not eliminate the discrepancy. An attempt to remedy this situation by incorporating a phenomenological interchain interaction leads to a deterioration of the corresponding theoretical prediction for the zero-field transverse

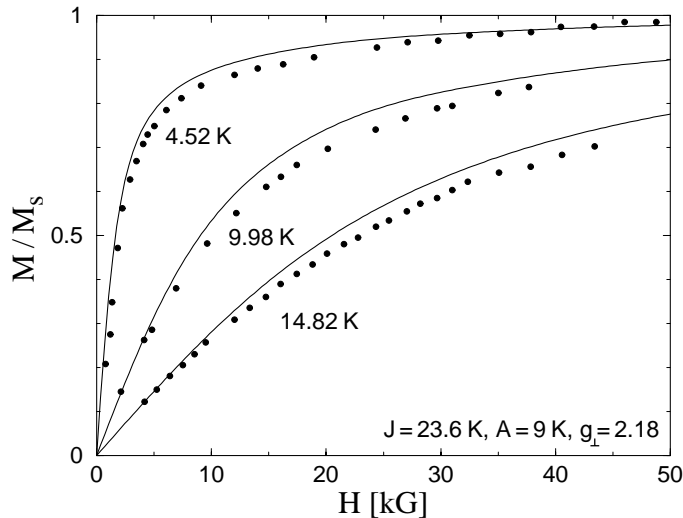


**Figure 6.3:** Comparison of TMRG predictions for the field dependence of the magnetization  $M$  at selected temperatures with experimental data from reference 72 (solid circles).  $M_s$  is the saturation magnetization, and the specific choice of parameters is discussed in the text.

susceptibility [72].

We next discuss the specific heat  $C = C(T, H)$  which was measured experimentally by Ramirez and Wolf [81]. In fact, most of the attention was concentrated on the *excess* specific heat

$$\Delta C = C(T, H) - C(T, 0) \quad (6.10)$$

viewed as a function of field  $H$  at some specified temperature  $T$ . An elementary argument based on the dilute-magnon approximation suggests that  $\Delta C$  is negative and decreases with increasing field, because the magnon dispersion discussed in section 6.2 increases monotonically with  $H$  for all values of the crystal momentum  $q$ . Nevertheless, the experiment revealed that  $\Delta C$  rises to a positive maximum at some field  $H_{max} \sim T^2$  before it begins to decrease and eventually reach negative values for stronger fields. A possible explanation of this unexpected behavior could be that the dilute-magnon approximation breaks down in the actual temperature range of the experiment, or “nonlinear modes” are activated in addition to magnons. Whence the beginning of a long debate concerning the possible relevance of sine-Gordon kinks, at least in some approximate sense [72, 73].

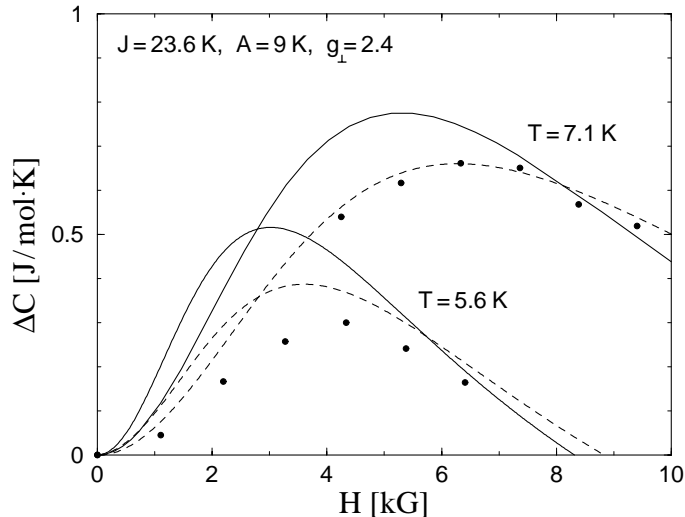


**Figure 6.4:** Comparison of TMRG predictions for the excess specific heat (solid lines) with experimental data from reference 81 (solid circles) for two typical values of temperature. The dashed lines depict the corresponding theoretical results of reference 73 for the same set of parameters given by equation (6.6).

One of the advantages of an accurate numerical algorithm such as TMRG is that potential nonlinear effects are automatically taken into account. Our results for the excess specific heat calculated for the standard choice of parameters given in equation (6.6) are depicted in figure 6.4 for two characteristic values of temperature actually employed in the experiment [81]. In spite of the overall qualitative agreement, significant quantitative differences are apparent in figure 6.4 for both values of the temperature. We were thus surprised to note that the theoretical results of Cuccoli et al [73, 82] for the same set of parameters, depicted by dashed lines in figure 6.4, are in agreement with the data for the specific temperature  $T = 7.1$  K. On the other hand, our results agree with those given by Delica et al [72] for the same set of parameters, except for some minor (a few percent) differences anticipated by the introductory remarks of this section. As mentioned already, a similar criticism applies to the calculation of the transverse susceptibility by Cuccoli et al [73]. We must thus conclude that the semiclassical nature of their method does not allow a completely accurate calculation in this temperature range and the claimed agreement with experiment is fortuitous.

It is now interesting to examine whether or not the alternative set of

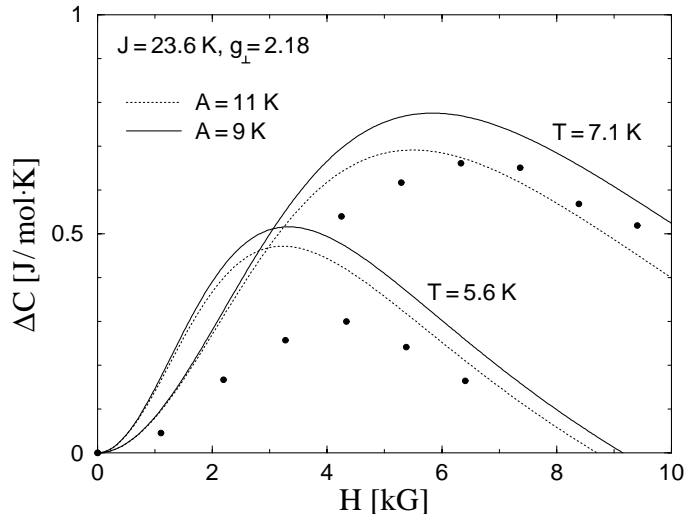


**Figure 6.5:** Comparison of TMRG predictions for the excess specific heat, for two different sets of parameters, with experimental data from reference 81 (solid circles).

parameters given in equation (6.7) may be used to eliminate the observed differences. In fact, our results quoted in figure 6.5, together with those given in figure 4 of reference 72 for yet another set of parameters, suggest that an accurate fit of the data is not possible for any reasonable choice of parameters.

Nevertheless, the main qualitative features of the experimental data are reproduced by the theoretical calculation. Therefore, it is important to examine further within the 1D model the mechanism by which the simple spinwave argument given earlier in the text is reconciled with a positive excess specific heat. In the remainder of this subsection we find it convenient to work exclusively with the rationalized parameters  $\alpha$  and  $h$  of equation (6.3) whereas the temperature  $\tau = T/J$  is measured in units of the exchange constant  $J$ . The corresponding absolute specific heat per lattice site is denoted by  $c = c(\tau, h)$  and the excess specific heat by  $\delta c = c(\tau, h) - c(\tau, 0)$ .

We first consider the quantity

$$-\tau \ln(\tau^{3/2}c) = G + G_1\tau + G_2\tau^2 + \dots, \quad (6.11)$$

where the expansion in the right-hand side presumes that the low-temperature thermodynamics is dominated by magnons with a  $q = 0$  energy gap equal

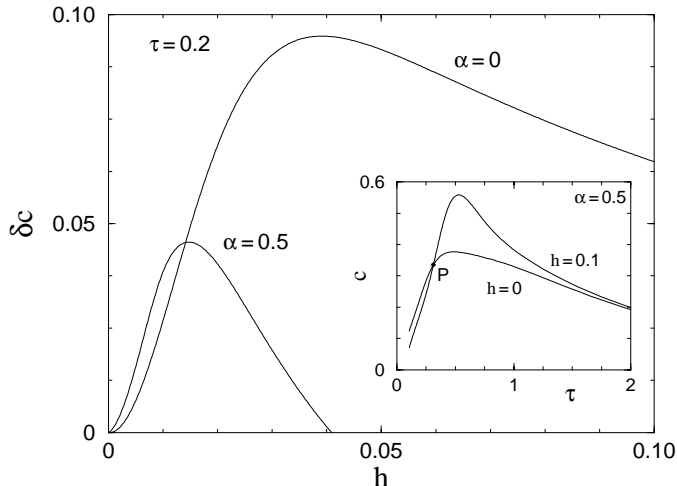


**Figure 6.6:** TMRG calculation of the excess specific heat  $\delta c$  for a typical anisotropy ( $\alpha = 0.5$ ) and for the isotropic spin-1 ferromagnetic chain ( $\alpha = 0$ ). The inset depicts the temperature dependence of the absolute specific heat  $c$  for two field values,  $h = 0$  and  $0.1$ , and anisotropy  $\alpha = 0.5$ . All quantities shown in this figure are expressed in rationalized units.

to  $G$ . A detailed TMRG calculation of the left-hand side of equation (6.11) for low temperatures down to  $\tau = 0.02$  reveals a behavior that is indeed consistent with the right-hand side of the same equation. Putting it in more practical terms, an extrapolation to  $\tau = 0$  using a second-degree polynomial to fit the low-temperature numerical data yields estimates of the magnon gap  $G$  which are in agreement with the direct DMRG calculation given in Table 6.1. A curious fact is that the present calculation gives values for the gap that are even closer to the  $1/n$  results of Table 6.1, but this may be an artifact of the specific second-order interpolation scheme.

The implied normal spinwave behavior of this easy-plane ferromagnetic chain should be contrasted with the low-temperature anomalies discovered by Johnson and Bonner [49] in an easy-axis ferromagnetic chain and recently confirmed by a TMRG calculation [44]. The absence of such anomalies in the present model reinforces the need for explaining the excess specific heat in simple terms.

The inset of figure 6.6 illustrates the calculated temperature dependence of the specific heat  $c$  for a typical anisotropy  $\alpha = 0.5$  and two field values;  $h = 0$  and  $0.1$ . It is clear that a nonzero field causes a depression of the

specific heat at low temperatures thanks to the opening of a finite magnon gap. This is the expected normal spinwave behavior, as predicted by the usual dilute-magnon approximation. What is not accounted for by dilute magnons is the crossing of the  $h = 0$  and  $h = 0.1$  curves at a point  $P$  that corresponds to a specific temperature  $\tau$  which depends on  $h$ . In particular,  $P$  is located near the origin for small  $h$  and moves outward with increasing  $h$ . This crossing is precisely the origin of the positive excess specific heat at low  $h$ , as demonstrated again by the  $\alpha = 0.5$  solid curve in the main frame of figure 6.6 for the specific temperature  $\tau = \tau_0 = 0.2$ .

Indeed, for any fixed  $\tau_0$ , the crossing point  $P$  occurs at some  $\tau < \tau_0$  for sufficiently weak fields, and thus leads to positive  $\delta c$  at  $\tau = \tau_0$ . With increasing field the point  $P$  moves to the right and the corresponding temperature  $\tau$  eventually overtakes  $\tau_0$ , thus leading to negative  $\delta c$  at  $\tau = \tau_0$  for sufficiently strong fields. The described picture is valid for any choice of  $\tau_0$ , and is confirmed by all of our numerical experiments. Therefore, the explanation of a positive  $\delta c$  at low fields is equivalent to ascertaining the robust enhancement of the absolute specific heat  $c$  with increasing field, inspite of its initial depression by the field dependent magnon gap.

At this point one could invoke the popular sine-Gordon approximation to argue that the crossing mechanism described in the preceding paragraph is due to the activation of kinks or other nonlinear modes in addition to magnons. We think that such an interpretation is dubious simply because the same mechanism occurs also in the *isotropic* Heisenberg chain, as illustrated by the  $\alpha = 0$  line in figure 6.6. In fact, the effect is strongly pronounced in the isotropic limit, even though a sine-Gordon approximation is clearly out of question.

Therefore, we return to the described crossing mechanism and attempt to explain it by more elementary means [83]. The absolute specific heat satisfies the obvious identity

$$\int_0^\infty d\tau c(\tau, h) = u(\infty, h) - u(0, h), \quad (6.12)$$

where  $u(\tau, h)$  is the internal energy at temperature  $\tau$  and field  $h$ . A corresponding identity for the excess specific heat is obtained by applying equation

(6.12) twice:

$$\int_0^\infty d\tau \delta c(\tau, h) = [u(\infty, h) - u(\infty, 0)] + [u(0, 0) - u(0, h)]. \quad (6.13)$$

A significant simplification occurs in the limit of an isotropic ferromagnetic chain for which the field dependence of the energy levels is simply a linear Zeeman shift  $mh$ , with  $m = 0, \pm 1, \pm 2, \dots$ . Therefore the field dependence averages out of the infinite-temperature internal energy  $u(\infty, h)$ , which is the sum of all energy levels, and  $u(\infty, h) - u(\infty, 0) = 0$ . If we further recall that  $e(h) = u(0, h)$  is the ground-state energy at field  $h$ , we obtain the elementary sum rule

$$\int_0^\infty d\tau \delta c(\tau, h) = e(0) - e(h) = h, \quad (6.14)$$

where we have also invoked the known energy of the fully polarized ferromagnetic ground state.

The obvious consequence of equation (6.14) is that positive values of  $\delta c$  are the rule rather than the exception. In particular, the initial depression of the specific heat ( $\delta c < 0$ ) at low temperatures, due to the opening of a magnon gap at finite field, is overwhelmed by positive values of  $\delta c$  attained at higher temperatures also thanks to the applied field. This explains the gross features of the crossing mechanism described earlier in the text and concludes our discussion of the excess specific heat.

### 6.3.2 Field parallel to $c$

The case of a field parallel to the  $c$ -axis is equally interesting but the corresponding experimental work has not been as extensive. We begin with the discussion of the temperature dependence of the zero-field longitudinal susceptibility. A notable feature of  $\chi_{\parallel}(T)$  is that it must approach a finite value in the limit  $T \rightarrow 0$ . A simple estimate of this value is obtained by a straightforward classical argument. In the presence of a field  $\mathbf{H} = (0, 0, H)$  the classical ground state is such that all spins form an angle  $\theta$  with the  $c$ -axis calculated from  $\cos \theta = g_{\parallel} \mu_B H / 2A$ . Therefore, the  $T = 0$  magnetization is given by  $M = \Lambda g_{\parallel} \mu_B \cos \theta$  and the susceptibility by

$$\chi_{\parallel}^{cl}(T = 0) = \frac{1}{2A} (\Lambda g_{\parallel}^2 \mu_B^2), \quad (6.15)$$

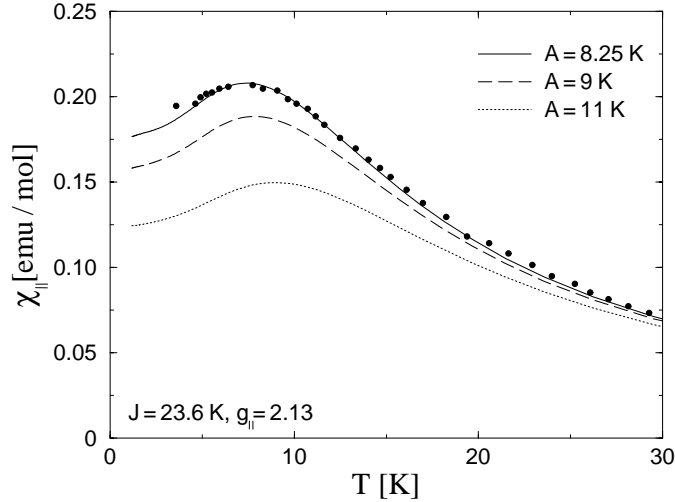


**Figure 6.7:** Comparison of TMRG predictions for the temperature dependence of the zero-field longitudinal susceptibility  $\chi_{||}$  with experimental data from reference 80 (solid circles).

where  $\Lambda$  is the total number of magnetic sites and  $g_{||}$  is the gyromagnetic ratio for a field applied along the  $c$ -axis.

Of course, numerical estimates based on the above classical result are not expected to be accurate, for reasons similar to those explained in section 6.2. However, a more accurate prediction may again be obtained through the  $1/n$  expansion. To leading order, the  $T = 0$  magnetization is calculated as the expected value of the azimuthal spin in the Hartree variational ground state given in the Appendix of reference 74. Restricting that calculation to weak fields one may extract the  $T = 0$  longitudinal susceptibility

$$\chi_{||}^{1/n}(T = 0) = \frac{1}{A} \left(1 - \frac{A}{4J}\right) (\Lambda g_{||}^2 \mu_B^2). \quad (6.16)$$

The main difference from equation (6.15) is an overall factor of 2, which is essentially the same factor that caused the low estimate  $A = 4.5$  K in the early literature [77], in addition to some mild dependence on the exchange constant. In any case, the main conclusion is that  $\chi_{||}$  is more sensitive to the value of the anisotropy constant  $A$  than to the exchange constant  $J$ , a situation that is reverse to the one encountered in section 6.3.1.

Therefore, the longitudinal susceptibility is an ideal physical quantity to yield a sensible estimate of the anisotropy constant  $A$ , provided that an

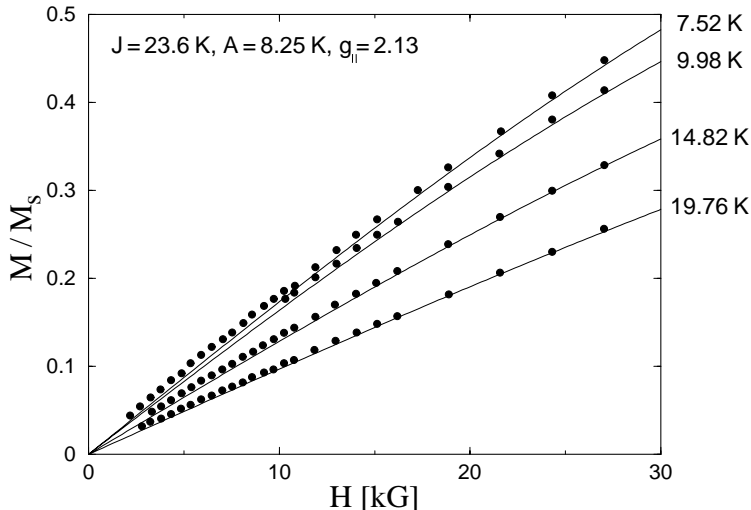


**Figure 6.8:** Comparison of TMRG predictions for the field dependence of the magnetization  $M$  at selected temperatures with experimental data from reference 72 (solid circles). The field is applied along the  $c$ -axis and  $M_s$  is the saturation magnetization.

accurate value for  $g_{\parallel}$  is also available. The latter is fixed here by appealing to a theoretical estimate [80] of the difference  $g_{\perp} - g_{\parallel} \simeq 5 \times 10^{-2}$  which leads to  $g_{\parallel} = 2.13$  if we adopt our earlier value for the transverse gyromagnetic ratio  $g_{\perp} = 2.18$ . The corresponding TMRG calculation of  $\chi_{\parallel}(T)$  is illustrated in figure 6.7 for various reasonable choices of  $A$ . The experimental data [80] are well reproduced for the set of parameters

$$J = 23.6 \text{ K}, \quad A = 8.25 \text{ K}, \quad g_{\parallel} = 2.13, \quad (6.17)$$

which is closer to the set employed by Delica et al [72]. In addition, the field dependence of the magnetization measured at selected temperatures [72] agrees with our TMRG calculation without further fit of parameters, as demonstrated in figure 6.8.

Incidentally, for this choice the classical result (6.15) yields 0.10 emu/mol and the leading  $1/n$  approximation (6.16) gives 0.19 emu/mol. These values should be compared with  $\chi_{\parallel}(T = 0) \simeq 0.175$  emu/mol extracted by a visual extrapolation of the solid curve in figure 6.7 to  $T = 0$ . Including the  $1/n$  correction produced by zero-point fluctuations in equation (6.16) will bring its prediction to the same level of accuracy with the magnon gap discussed in Table 6.1.

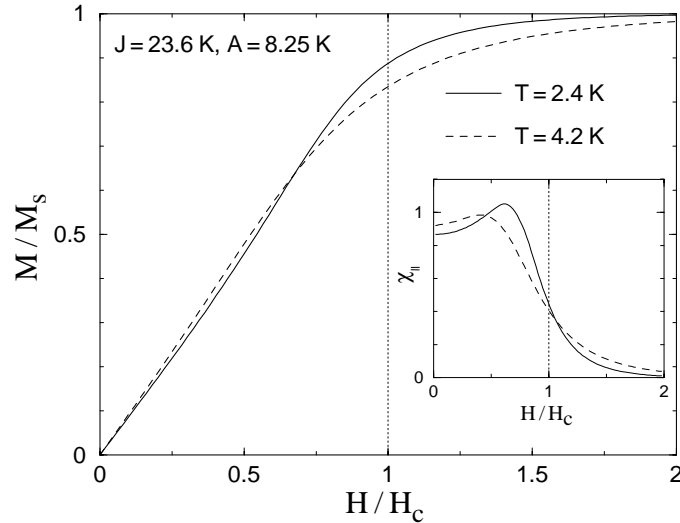


**Figure 6.9:** TMRG calculation of the field dependence of the magnetization  $M$  for a wide field range and two typical values of temperature. The inset displays the corresponding results for the field dependence of the susceptibility. The field is applied along the  $c$ -axis and the critical field  $H_c$  is estimated to be 58 kG for  $g_{\parallel} = 2.13$ .

It is now interesting to take this calculation into the region of strong fields where the ground state becomes completely ordered along the  $c$ -axis. Such a ferromagnetic state is actually an exact eigenstate of the Hamiltonian for any strength of the field  $H$ . But the corresponding magnon gap

$$G = g_{\parallel}\mu_B H - A \quad (6.18)$$

is positive only for  $H > H_c$  where

$$H_c = A/g_{\parallel}\mu_B \quad (6.19)$$

is the critical field beyond which the fully ordered state is the absolute ground state. The gap vanishes for all  $H < H_c$  because the corresponding magnon is a Goldstone mode associated with the axial symmetry for this field orientation.

For the set of parameters (6.17) one finds that  $H_c = 58$  kG, in reasonable agreement with the value 62.5 kG estimated from an experiment of A. Miedan which is quoted in reference 80 but is apparently unpublished. According to the description of Dupas and Renard, [80] Miedan measured the field

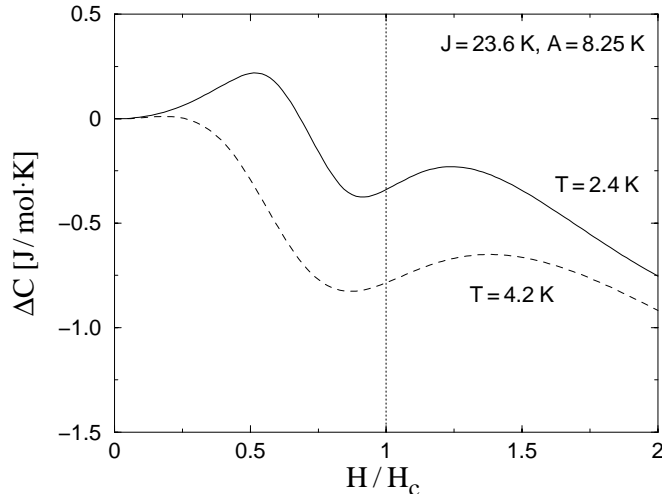


**Figure 6.10:** TMRG calculation of the excess specific heat for a wide field range and two typical values of temperature. The field is applied along the  $c$ -axis and the critical field  $H_c$  is estimated to be 58 kG for  $g_{\parallel} = 2.13$ .

dependence of the magnetization at  $T = 4.2$  K and extracted  $H_c$  from the observed bending of the  $M(H)$  curve. Although we do not know the details of this experiment, we have calculated the  $M(H)$  curve at  $T = 4.2$  K for a wide field range and the result is depicted by a dashed line in figure 6.9. Interestingly, the bending of the  $M(H)$  curve is not predicted to be especially sharp at this temperature, as is apparent in the corresponding susceptibility displayed also by a dashed line in the inset of figure 6.9. In other words, if the location of the maximum of the susceptibility were taken as an estimate of the critical field  $H_c$ , the latter would have been severely underestimated. The situation improves slowly at lower temperatures, as indicated by the solid lines in figure 6.9 which correspond to  $T = 2.4$  K; i.e., to a temperature that is already below the 3D-transition temperature  $T_N = 2.7$  K.

It is clear that we cannot go farther with our theoretical arguments without explicit knowledge of detailed experimental data on  $M(H)$  in this field region. We thus conclude the discussion of magnetization with a comment concerning an apparent contradiction between the results of figure 6.9 and those given earlier in figure 6.8 for lower field strengths. Indeed, figure 6.8 suggests that the magnetization  $M(H)$  for any given field  $H$  decreases with increasing temperature, as expected, while figure 6.9 indicates that a rela-

tive crossing occurs between any two  $M(H)$  curves. The resolution of this apparent paradox lies in the fact that the values of temperature employed in figure 6.8 are all greater than the temperature  $T \simeq 7.5$  K, at which the maximum of the zero-field susceptibility of figure 6.7 occurs, while those of figure 6.9 are smaller.

Finally, we discuss the specific heat in a field parallel to the  $c$ -axis. It appears that no measurements have been made for this field orientation but could prove to be feasible in the future [84]. Our TMRG calculation of the excess specific heat is illustrated in figure 6.10 for the two values of temperature employed in our preceding discussion of the magnetization. The characteristic double peak near the critical field  $H_c$  was anticipated by earlier work [83] based on a classical transfer matrix calculation, on the known exact solution for a spin- $\frac{1}{2}$  XY chain, as well as on an accurate numerical solution for a spin- $\frac{1}{2}$  XXZ chain based on the Bethe Ansatz. The calculated double peak is also a clear departure from the corresponding prediction of the dilute-magnon approximation [83] and could eventually be observed in CsNiF<sub>3</sub>. An unfortunate feature of figure 6.10 is that a strongly pronounced double peak is predicted to occur in the low-temperature region where the 1D model is no longer applicable.

## 6.4 Conclusion

We have presented a more or less complete calculation of the dynamics and the thermodynamics associated with the spin-1 Hamiltonian (6.1). The  $T = 0$  dynamics is efficiently described by an  $1/n$  expansion whose full potential has not yet been explored. For example, an accurate calculation of the magnon dispersion for a field parallel to the  $c$ -axis is also possible but has not been carried out mainly because there seems to have been no experimental effort in that direction.

On the other hand, the thermodynamics is calculated by a powerful TMRG method which has opened the way to obtain accurate theoretical predictions for a wide class of quantum magnetic chains. Suffice it to say that our present algorithm may be trivially adjusted to handle spin-1 Haldane-gap antiferromagnets [85] in the presence of anisotropy and external fields. Even in the case of completely integrable spin- $\frac{1}{2}$  chains, for which the Bethe

Ansatz applies, the calculation of the thermodynamics is far from trivial [69]. Nevertheless, TMRG can be applied in a straightforward manner irrespective of complete integrability [44].

The extent to which the 1D Hamiltonian (6.1) may describe the magnetic properties of CsNiF<sub>3</sub> has been debated on several occasions. Our calculations confirm the general conclusion that the 1D model accounts for the main features of all available experimental data. But it is also clear that departures from ideal model behavior are present, especially at low temperatures approaching the 3D-ordering transition temperature  $T_N = 2.7$  K.

## CHAPTER 7

# CONCLUSION

In this work we have presented a complete analysis of bulk and surface spin-flop transitions induced by a uniform magnetic field in special cases of the general XYZ model of equation (1.1). The classical analysis of chapter 2 shows that surface effects are easier to comprehend in our model than in the case of the single-ion model and is therefore helpful for a better understanding of the surface transition in magnetic multilayers [22–35]. But, the main reason for performing the classical study was to provide a guide for the quantum mechanical model of chapters 3 to 5.

To the best of our knowledge the SSF transition presented in chapter 3 is the first example of a surface transition induced in a quantum spin- $\frac{1}{2}$  model by a uniform magnetic field. For the specific choice of parameters (3.1) the surface transition of the quantum chain is present for all values of anisotropy, sharing several common features with that of the classical system. In fact, our results suggest that the occurrence of a similar transition is a generic characteristic of the larger family of XYZ models defined by inequalities (2.1).

If a magnetic material is found to be described by our model (3.1) this work can be a guide for its experimental study. The calculation of thermodynamic properties and ESR spectrum can then be used for the determination of the values of parameters used in our model. Doping such a material with nonmagnetic ions [57] would produce open magnetic chains of varying size. The surface spin-flop transition can then be probed through low temperature

ESR spectroscopy as described in the text.

Recently there has been increased research interest for boundary induced phenomena arising in doped spin-1 Haldane-gap materials [86–88] whose origin has not yet been understood. Furthermore, one-dimensional spin- $\frac{1}{2}$  materials have recently attracted attention especially with respect to ultrafast non-linear optical properties [89–91] that could lead to all-optical switches applicable in high speed network systems. The Bethe Ansatz does not apply for the majority of these models. Therefore alternative more versatile methods are needed for the study of surface as well as bulk properties, as explained in the main body of this thesis.

For example, the recently developed DMRG and TMRG methods presented in chapter 5 have proved to be extremely efficient for the study of thermodynamic properties and, corroborated with direct diagonalization, can provide a complete analysis of quantum spin systems. Both methods are independent of complete integrability and are easily generalized to a wide range of quantum chains. The power of these methods was demonstrated in chapter 6 where we used DMRG and TMRG for a thorough analysis of experimental results on the spin-1 planar ferromagnet  $\text{CsNiF}_3$ .

# APPENDIX A

## DETAILED DESCRIPTION OF THE SSF PHASE

The SSF phase is easier to understand in the strong anisotropy limit where the created formations remain compact or even locked for most of the  $(H_s, H_b)$  region. On the other hand close to the isotropic limit the surface state is wider and evolves continuously to a DW through a non trivial mechanism.

Numerical investigation for small anisotropies shows that there is a correspondence between the spin configuration of a surface state and that of a DW. For example in figure A.1 we show the surface state of a system with 22 sites compared to a selected part of a bulk DW, for the same parameters  $\Delta$  and  $H$ , and we see that they coincide. One can therefore conclude that the evolution of the surface state with the field within the SSF phase is described by a DW moving from infinite distance away from the surface of the system under  $H_s$  to infinite distance within the system above  $H_w$ . We should mention here that the impressive agreement shown above in figure A.1 was achieved by a careful choice of fields  $H$  so that the position of the DW with respect to the finite lattice will allow it to be of the “up” type.

One can use this idea to extract more information about the SSF phase near the isotropic limit where the continuous approximation of equation (2.17) is valid. We consider a chain of  $\Lambda = 200$  spins and anisotropy  $\Delta = 1.005$  and we create a state with a DW located at site  $x$  by setting the spins in a configuration given by the analytical solution (2.17). Specifi-

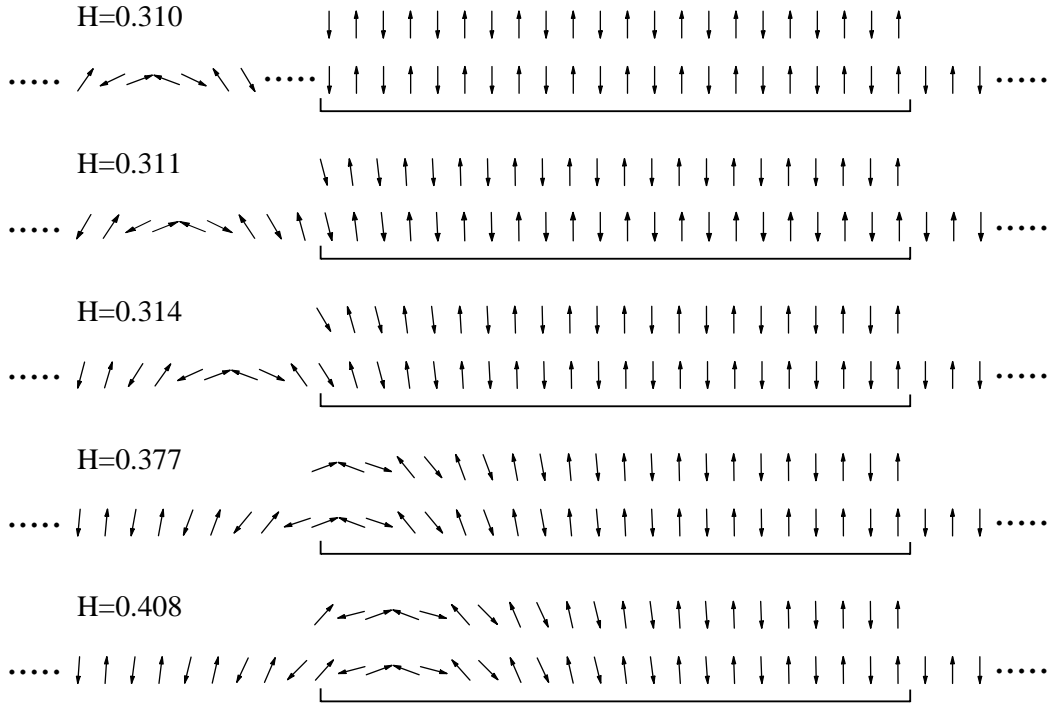


**Figure A.1** : Spin configuration of a chain of  $\Lambda = 22$ ,  $\Delta = 1.125$ , in comparison with the spin configuration of a DW in the bulk for a choice of bias fields  $H$ . We see that the surface state coincides with the underlined part of the DW. For this set of parameters it is  $H_s = 0.310$ ,  $H_w = 0.428$ .

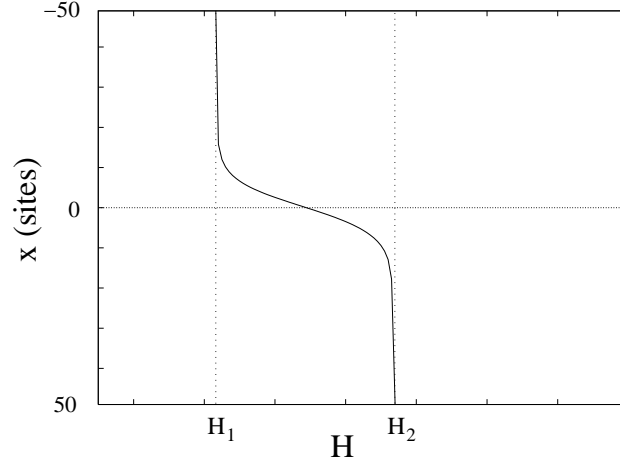


**Figure A.2** : The energy minimizing position of a DW with respect to the surface as a function of the magnetic field. We can see that in the SSF phase the DW relaxes at finite distance from the surface. Negative values correspond to positions out of the chain.

cally, we set the reference system for the  $x$ -axis at site 1 to get

$$\begin{aligned} S_{2\alpha-1} &= \frac{m(y_\alpha) + n(y_\alpha)}{2}, \\ S_{2\alpha} &= \frac{m(y_\alpha) - n(y_\alpha)}{2}, \end{aligned} \quad (\text{A.1})$$

$$y_\alpha = \sqrt{2\delta(1-h^2)}[(\alpha-1) - x], \quad \alpha = 1, 2, \dots, \Lambda/2$$

where  $m(y)$  and  $n(y)$  are given by equation (2.17). We then minimize the energy of the chain with respect to the position  $x$  for fields in the region  $(H_s, H_b)$ . In figure A.2 we display the energy minimizing position of the wall as a function of the applied magnetic field. We see that the wall migrates from  $x = -\infty$  (at infinite distance from our system) below  $H_s$  to  $x = +\infty$  (in our case the center of the chain for  $x = 50$ ) above  $H_w$ .

The results found by the procedure described above are in very good agreement with those obtained by applying our relaxation algorithm for the same parameters  $\Delta$  and  $H$ . This is demonstrated in figure A.3 where we display the third component of the magnetization produced by the two different methods. The disagreement for big values of  $H$  is due to the failure of the continuous approximation close to  $H_b$ .

From the analysis above we can conclude that for every field value in the region  $(H_s, H_w)$  there is a site in the DW, at finite distance from its center,

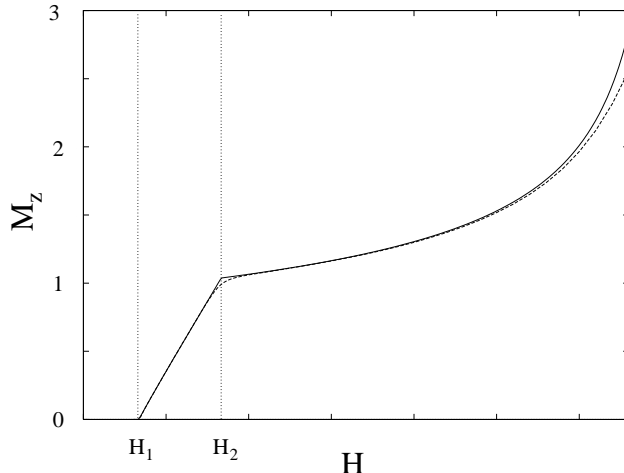


**Figure A.3** : The  $z$ -axis magnetization of a system obtained through our relaxation algorithm (dashed line) and the continuous model (solid line).

that hardly interacts with one of its neighbors. For example in figure A.1 the last underlined spin of the DW on the left remains in the same position no matter if the spin on its left is there or not<sup>1</sup>.

The time evolution of a spin in the chain is governed by the Landau-Lifshitz equations

$$\frac{\partial \mathbf{S}_i}{\partial t} = \mathbf{S}_i \times \mathbf{F}_i \quad (\text{A.2})$$

where  $\mathbf{F}_i = -\partial W / \partial S_i$ . If for a given field  $H$  in  $(H_s, H_w)$  it is the  $i$ th spin that does not interact with its previous neighbor  $\mathbf{S}_{i-1}$  then it will be

$$\mathbf{S}_i \times \mathbf{F}_i^{(i-1)} = 0 \quad (\text{A.3})$$

where  $\mathbf{F}_i^{(i-1)}$  is the part of  $\mathbf{F}_i$  due to the previous spin  $\mathbf{S}_{i-1}$ . Equation (A.3) is actually the condition that two neighboring spins have to satisfy so that there can be a surface state identical to the part of the DW at the right of site  $i$  and can be rewritten as

$$\Delta \frac{S_i^y}{S_i^z} = \frac{S_{i-1}^y}{S_{i-1}^z}. \quad (\text{A.4})$$

One can substitute the solution of the continuous (2.17) into (A.4) to get analytical formulas for the critical fields for  $H_s$  and  $H_w$ . Although we shall

<sup>1</sup>Actually there are two such sites symmetric around the center of the wall.

---

not provide these result here they coincide with those of (3.20) and (2.57) in the limit of small anisotropies.

Condition (A.3) is satisfied because of the exchange nature of the anisotropy and thus can not be applied in the single ion model describing magnetic superlattices. This is the reason that a smooth transition from the Néel state to the DW state does not take place in the single ion model causing a more involved picture of the SSF transition.



# Bibliography

- [1] E. Ising, Z. Physik **31**, 253 (1925).
- [2] *Crystal statistics. I. A two-dimensional model with an order-disorder transition*, L. Onsager, Phys. Rev. **65**, 117 (1944).
- [3] W. Heisenberg, Z. Physik **49**, 619 (1928).
- [4] F. Bloch, Z. Physik. **61**, 206 (1930).
- [5] *Two soluble models of an antiferromagnetic chain*, E. H. Lieb, T. D. Schultz, D. C. Mattis, Ann. Phys. (N.Y.) **16**, 407 (1961).
- [6] *Statistical mechanics of the anisotropic linear Heisenberg model*, S. Katsura, Phys. Rev. **127**, 1508 (1962).
- [7] A. Bethe, Z. Physik. **71**, 205 (1931).
- [8] *One-Dimensional chain of anisotropic spin-spin interactions. I. Proof of Bethe's hypothesis for ground state in a finite system*, C. N. Yang and C. P. Yang, Phys. Rev. **150**, 321 (1966).
- [9] *One-dimensional chain of anisotropic spin-spin interactions. II. Properties of the ground state energy per lattice site for an infinite system*, C. N. Yang and C. P. Yang, Phys. Rev. **150**, 327 (1966).
- [10] *One-Dimensional chain of anisotropic spin-spin interactions. III. Applications*, C. N. Yang and C. P. Yang, Phys. Rev. **151**, 258 (1966).
- [11] *Thermodynamics of the Heisenberg-Ising ring for  $\Delta \geq 1$* , M. Gaudin, Phys. Rev. Lett. **26**, 1301 (1971).
- [12] *La fonction d'onde de Bethe*, M. Gaudin (Masson, Paris, 1983).

- [13] *Thermodynamics of one-dimensional solvable models*, M. Takahashi (Cambridge University Press, Cambridge, United Kingdom, 1999).
- [14] *Exactly solved models in statistical mechanics*, R. J. Baxter (Academic Press, London, 1982).
- [15] *One-dimensional anisotropic Heisenberg chain*, R. J. Baxter, *Annals of Phys.* **70**, 323 (1972).
- [16] *Phase transitions and critical phenomena*, R. J. Baxter (Academic Press, London, 1972).
- [17] *Algebraic analysis of solvable lattice models*, M. Jimbo and T. Miwa (American Mathematical Society, Providence, Rhode Island, 1995).
- [18] *Quantum inverse scattering method*, L. D. Faddeev, *Sov. Sci. Rev. Math. Phys.* **1**, 107 (1981).
- [19] *Surface spin-flop state in a simple antiferromagnet*, D. L. Mills, *Phys. Rev. Lett.* **20**, 18 (1968).
- [20] *Surface effects in the Heisenberg antiferromagnet*, D. L. Mills and W. Saslow, *Phys. Rev.* **171**, 488 (1968).
- [21] *Dynamics of the antiferromagnetic spin-flop transition*, F. Keffer and H. Chow, *Phys. Rev. Lett.* **31**, 1061 (1973).
- [22] *Surface spin-flop transition in Fe/Cr(211) superlattices: Experiment and theory*, R. W. Wang, D. L. Mills, E. E. Fullerton, J. E. Mattson and S. D. Bader, *Phys. Rev. Lett.* **72**, 920 (1994).
- [23] *Magnons in antiferromagnetically coupled superlattices*, R. W. Wang, D. L. Mills, E. E. Fullerton, S. Kumar and M. Grimsditch, *Phys. Rev. B* **53**, 2627 (1996).
- [24] *Low-frequency dynamic response and hysteresis in magnetic superlattices*, S. Rakhmanova, D. L. Mills and E. E. Fullerton, *Phys. Rev. B* **57**, 476 (1998).

- 
- [25] *Magnetic properties of finite antiferromagnetic superlattices: Statics, dynamics, and the surface spin-flop phase*, R. W. Wang and D. L. Mills, Phys. Rev. B **50**, 3931 (1994).
- [26] *Finite-size effects on spin configurations in antiferromagnetically coupled multilayers*, F. C. Nörtemann, R. L. Stamps, A. C. Carrico and R. E. Camley, Phys. Rev. B **46**, 10847 (1992).
- [27] *Microscopic calculation of spin waves in antiferromagnetically coupled multilayers: Nonreciprocity and finite-size effects*, F. C. Nörtemann, R. L. Stamps and R. E. Camley, Phys. Rev. B **47**, 11910 (1993).
- [28] *Dynamic susceptibilities for magnetic layered structures*, R. L. Stamps, R. E. Camley, F. C. Nörtemann and D. R. Tilley, Phys. Rev. B **48**, 15740 (1993).
- [29] *Field and surface effects on the ground state of antiferromagnetic systems*, L. Trallori, P. Politi, A. Rettori, M. G. Pini and J. Villain, Phys. Rev. Lett. **72**, 1925 (1994).
- [30] *Field dependence of the magnetic susceptibility of an Fe/Cr(211) superlattice: effect of discreteness and chaos*, L. Trallori, P. Politi, A. Rettori, M. G. Pini and J. Villain, J. Phys.: Condens. Matter **7**, L451 (1995).
- [31] *Magnetic superlattices, classical spin chains, and the Frenkel-Kontorova model*, L. Trallori, Phys. Rev. B **57**, 5923 (1998).
- [32] *Surface spin-flop phases and bulk discommensurations in antiferromagnets*, C. Micheletti, R. B. Griffiths and J. Yeomans, J. Phys. A **30**, L233 (1997).
- [33] *Surface spin-flop and discommensuration transitions in antiferromagnets*, C. Micheletti, R. B. Griffiths and J. Yeomans, Phys. Rev. B **59**, 6239 (1999).
- [34] *The ferromagnetic moment of an antiferromagnetic domain wall*, N. Papanicolaou, J. Phys.: Condens. Matter **10**, L131 (1998).
- [35] *Low-frequency dynamics in an antiferromagnetic superlattice*, N. Papanicolaou, J. Phys.: Condens. Matter **11**, 59 (1999).

- [36] *Anisotropic ferromagnetic quantum domains*, F. C. Alcaraz, S. R. Salinas and W. F. Wrezninski, Phys. Rev. Lett. **75**, 930 (1995).
- [37] *XXZ chain with a boundary*, M. Jimbo, R. Kedem, T. Kojima, H. Konno and T. Miwa, Nucl. Phys. B **441**, 437 (1995).
- [38] *Surface excitations and surface energy of the antiferromagnetic XXZ chain by the Bethe Ansatz approach*, A. Kapustin and S. Skorik, J. Phys. A **29**, 1629 (1996).
- [39] *Conditions for a ferromagnetic ground state of Heisenberg Hamiltonians*, H. P. Bader and R. Schilling, Phys. Rev. B **19**, 3556 (1979).
- [40] *Surface exponents of the quantum XXZ, Ashkin-Teller and Potts models*, F. C. Alcaraz, M. N. Barber, M. T. Batchelor, R. J. Baxter and G. R. W. Quispel, J. Phys. A **20**, 6397 (1987).
- [41] *Heisenberg XYZ Hamiltonian with integrable impurities*, Zhan-Ning Hu, Phys. Lett. A **250**, 337 (1998).
- [42] *Surface spin-flop transition in a classical XYZ chain*, J. Karadamoglou and N. Papanicolaou, J. Phys. A **32**, 3275 (1999).
- [43] *Bulk and surface spin-flop transitions in an antiferromagnetic XYZ chain*, J. Karadamoglou and N. Papanicolaou, Phys. Rev. B **60**, 9477 (1999).
- [44] *Thermodynamics of the spin-flop transition in a quantum XYZ chain*, X. Wang, X. Zotos, J. Karadamoglou and N. Papanicolaou, Phys. Rev. B **61**, 14303 (2000).
- [45] *Magnon dispersion and thermodynamics in CsNiF<sub>3</sub>*, J. Karadamoglou, N. Papanicolaou, X. Wang, and X. Zotos, to appear in Phys. Rev. B (2001).
- [46] *Antiferromagnetic domain walls*, N. Papanicolaou, Phys. Rev. B **51**, 15062 (1995).
- [47] *Soliton like excitations in a one-dimensional atomic chain with nonlinear deformable substrate potential*, M. Peyrard and M. Remoissenet, Phys. Rev. B **26**, 2886 (1982).

- 
- [48] *Models with competing interactions*, C. Micheletti, Ph.D. thesis, Department of Physics, Theoretical Physics, University of Oxford, 1996.
- [49] *Excitation spectrum and low-temperature thermodynamics of the Ising-Heisenberg linear ferromagnet*, J. D. Johnson and J. C. Bonner, Phys. Rev. B **22**, 251 (1980).
- [50] *Common structures between finite systems and conformal field theories through quantum groups*, V. Pasquier and H. Saleur, Nucl. Phys. B **330**, 523 (1990).
- [51] *Advanced mathematical methods for scientists and engineers*, C. M. Bender and S. A. Orszag (McGraw-Hill, New York, 1978).
- [52] see <http://netlib.uow.edu.au/linalg/lalqmr> for the look ahead Lanczos method.
- [53] *Correlated electrons in high-temperature superconductors*, E. Dagotto, Rev. Mod. Phys. **66**, 763 (1994).
- [54] *Variations on Arnoldi method for computing eigenelements of large unsymmetric matrices*, Y. Saad, Lin. Alg. App. **34**, 269 (1980).
- [55] *Bloch oscillations of magnetic solitons in anisotropic spin-1/2 chains*, J. Kyriakidis and D. Loss, Phys. Rev. B **58**, 5568 (1998).
- [56] *Low-Temperature thermodynamics of the  $|\Delta| \geq 1$  Heisenberg-Ising ring*, J. D. Johnson and B. M. McCoy, Phys. Rev. A **6**, 1613 (1972).
- [57] *Experimental and theoretical studies of finite-size effects in an  $S = 1/2$  antiferromagnetic Heisenberg chain*, H. Asakawa, M. Matsuda, K. Minami, H. Yamazaki and K. Katsumata, Phys. Rev. B **57**, 8285 (1998).
- [58] *Principles of magnetic resonance*, C. P. Slichter (Springer-Verlag, Berlin Heidelberg, New York, 1978).
- [59] *Density - matrix renormalization*, Lecture Notes in Physics, vol. 258, M. Kaulke I. Peschel, X. Wang and K. Hallberg (Springer - Verlag, New York, 1999).

- [60] *Transfer-matrix density-matrix renormalization-group theory for thermodynamics of one-dimensional quantum systems*, X. Wang and T. Xiang, Phys. Rev. B **56**, 5061 (1997).
- [61] *The density matrix renormalization group for a quantum spin chain at non-zero temperature*, R. J. Bursill, T. Xiang and G. A. Gehring, J. Phys.: Condens. Matter **8**, L583 (1996).
- [62] *On the product of semi-groups of operators*, H. F. Trotter, Proc. Am. Math. Soc. **10**, 545 (1959).
- [63] *Generalized Trotter's formula and systematic approximants of exponential operators and inner derivations with applications to many body problems*, M. Suzuki, Commun. Math. Phys. **51**, 183 (1976).
- [64] *Density matrix formulation for quantum renormalization groups*, S. R. White, Phys. Rev. Lett. **69**, 2863 (1992).
- [65] *Density-matrix algorithms for quantum renormalization groups*, S. R. White, Phys. Rev. Lett. **48**, 10345 (1993).
- [66] *The renormalization group: Critical phenomena and the Kondo problem*, K. G. Wilson, Rev. Mod. Phys. **47**, 773 (1975).
- [67] *Statistical mechanics, A set of lectures*, R. P. Feynman (Addison-Wesley Publishing Company, Inc, 1972).
- [68] *Magnetic-field effects on two-leg Heisenberg antiferromagnetic ladders: Thermodynamic properties*, X. Wang and L. Yu, Phys. Rev. Lett. **84**, 5399 (2000).
- [69] *Thermodynamics of the anisotropic spin- $\frac{1}{2}$  Heisenberg chain and related quantum chains*, A. Klümper, Z. Phys. B **91**, 507 (1993).
- [70] *Spin waves in CsNiF<sub>3</sub> with an applied magnetic field*, M. Steiner and J. K. Kjems, J. Phys. C : Solid State Phys. **10**, 2665 (1977).
- [71] *Bose operator expansions of tensor operators in the theory of magnetism. II*, P. A. Lindgard and A. Kowalska, T. Phys. C: Solid State Phys. **9**, 2081 (1976).

- 
- [72] *Static properties of CsNiF<sub>3</sub>: Comparison of numerical results, experimental data, and predictions from soliton-bearing models*, T. Delica, W. J. M. de Jonge, K. Kopinga, H. Leschke and H. J. Mikeska, Phys. Rev. B **44**, 11773 (1991).
- [73] *Quantum thermodynamics of the easy-plane ferromagnetic chain*, A. Cuccoli, V. Tognetti, P. Verrucchi and R. Vaia, Phys. Rev. B **46**, 11601 (1992).
- [74] *Pseudospin approach for planar ferromagnets*, N. Papanicolaou, Nucl. Phys. B **240**, 281 (1984).
- [75] M. Steiner, private communication.
- [76] *Solitons in quantum-spin systems*, J. T. Chui and K. B. Ma, Phys. Rev. B **27**, 4515 (1983).
- [77] *Theoretical and experimental studies on one-dimensional magnetic systems*, M. Steiner, J. Vilain and C. G. Windsor, Adv. Phys. **25**, 87 (1976).
- [78] *Semiclassical and variational approximations for spin-1 magnetic chains*, L. R. Mead and N. Papanicolaou, Phys. Rev. B **26**, 1416 (1982).
- [79] *Quantum Monte Carlo and transfer-matrix calculations for one-dimensional easy-plane ferromagnets*, G. M. Wysin and A. R. Bishop, Phys. Rev. B **34**, 3377 (1986).
- [80] *Low-temperature magnetic properties of the three linear S=1 ferromagnets with an easy plane anisotropy: TMNB, TMNC and CsNiF<sub>3</sub>*, C. Dupas and J. P. Renard, J. Phys. C. : Solid State Phys. **10**, 5057 (1977).
- [81] *Specific heat of CsNiF<sub>3</sub>*, A. P. Ramirez and W. P. Wolf, Phys. Rev. B **32**, 1639 (1985).
- [82] R. Vaia, private communication.
- [83] *The magnetic field dependence of the specific heat in quantum spin chains with axial symmetry*, N. Papanicolaou and P. Spathis, J. Phys. C. : Solid State Phys. **20**, L783 (1987).

- [84] M. Orendac, A. Orendacova and M. W. Meisel, private communication.
- [85] *Calculation of the susceptibility of the  $S = 1$  antiferromagnetic Heisenberg chain with single-ion anisotropy using the transfer matrix renormalization group method*, D. Coombes, T. Xiang and G. A. Gehring, J. Phys.: Condens. Matter **10**, L159 (1998).
- [86] *Evidence of quantum criticality in the doped Haldane system  $Y_2BaNiO_5$* , C. Payen, E. Janod, K. Schoumacker, C. D. Batista, K. Hallberg, and A. A. Aligia, Phys. Rev. B **62**, 2998 (2000).
- [87] *Finite-size spectrum, magnon interactions, and magnetization of  $S = 1$  Heisenberg spin chains*, Jizhong Lou, Shaojin Qin, Tai-Kai Ng, Zhaobin Su, and Ian Affleck, Phys. Rev. B **62**, 3786 (2000).
- [88] *Spin-vacancy-induced long-range order in a new Haldane-gap antiferromagnet*, Y. Uchiyama, Y. Sasago, I. Tsukada, K. Uchinokura, A. Zheludev, T. Hayashi, N. Miura, and P. Böni, Phys. Rev. Lett. **83**, 632 (1999).
- [89] *Magnetic Susceptibility of Ideal Spin 1 /2 Heisenberg Antiferromagnetic Chain Systems,  $Sr_2CuO_3$  and  $SrCuO_2$* , N. Motoyama, H. Eisaki, and S. Uchida, Phys. Rev. Lett. **76**, 3212 (1996).
- [90] *Singularities in Optical Spectra of Quantum Spin Chains*, H. Suzuura, H. Yasuhara, A. Furusaki, N. Nagaosa, and Y. Tokura, Phys. Rev. Lett. **76**, 2579 (1996).
- [91] *Ultrafast optical nonlinearity in the quasi-one-dimensional mott insulator  $Sr_2CuO_3$* , T. Ogasawara, M. Ashida, N. Motoyama, H. Eisaki, S. Uchida, Y. Tokura, H. Ghosh, A. Shukla, S. Mazumdar, and M. Kuwata-Gonokami, Phys. Rev. Lett. **85**, 2204 (2000).